SHAPE COEXISTENCE NEAR THE Z=82 CLOSED SHELL
A STUDY OF THE EXCITED STATES OF ^{187}Au AND ^{187}Pt IN THE β^+ DECAY OF ^{187}Hg AND ^{187}Au.

A THESIS

Presented to

The Faculty of the Division of Graduate Studies

By

Marvin Anton Grimm, Jr.

In Partial Fulfillment

of the Requirements for the Degree

Doctor of Philosophy in the School of Physics

Georgia Institute of Technology

November, 1978

SHAPE COEXISTENCE NEAR THE Z=82 CLOSED SHELL

A STUDY OF THE EXCITED STATES OF ^{187}Au AND ^{187}Pt IN THE β^+ DECAY OF ^{187}Hg AND ^{187}Au.

A THESIS

Presented to

The Faculty of the Division of Graduate Studies

By

Marvin Anton Grimm, Jr.

In Partial Fulfillment

of the Requirements for the Degree

Doctor of Philosophy in the School of Physics

Georgia Institute of Technology

November, 1978

SHAPE COEXISTENCE NEAR THE Z=82 CLOSED SHELL

A STUDY OF THE EXCITED STATES OF ^{187}Au AND ^{187}Pt IN THE β^+ DECAY OF ^{187}Hg AND ^{187}Au.

Approved:

R. W. Fink

R. W. Fink, Chairman

C. H. Braden

F. T. Avignone

Date Approved by Chairman DEC 1 - 1978

I am deeply indebted to a number of people for their help and support in completing this thesis and would like to take this opportunity to thank them for their efforts.

First I would like to thank Dr. J. L. Wood, my senior postdoctoral research advisor, for suggesting the thesis topic and following it through to its completion. His interest, and fruitful discussions with him have been most helpful and are greatly appreciated. It would also like to thank Dr. R. W. Fink for acting as chairman of my thesis committee and reading committee, and Drs. C. H. Braden and F. T. Avignone for serving on both my reading and final examination committees. Their suggestions and corrections of the original manuscript of this thesis are greatly appreciated. I also thank Drs. E. H. Spejewski and R. L. Mlekodaj of UNISOR for serving on my final examination committee and acting as my laboratory supervisors at Oak Ridge National Laboratory.

Dr. H. K. Carter's assistance in setting up the experiments and taking the data and his help in mastering the Tennecomp computers is greatly appreciated. The assistance of Drs. L. L. Riedinger, C. R. Bingham, A. C. Kahler, E. F. Zganjar and A. Visvanathan in setting up the experiments is also gratefully acknowledged.

Financial assistance from the Ga. Tech Physics Department, in the form of a teaching/research assistantship, the Department of Energy, in the form of a research assistantship at Ga. Tech, and Oak Ridge

Associated Universities, through the Laboratory Graduate Participation Program, is greatly appreciated. I also thank Dr. D. A. McClure for encouraging me to apply for the Laboratory Graduate Participation Program.

The ORIC staff has been most hospitable and I would like to thank both the professional and technical staffs for their assistance and availability whenever needed. I also thank Miss Helen Dockery for her aid in using the Nuclear Data Group plotting program at ORNL and Mrs. Martha Dawson for her excellent typing of this manuscript.

Finally, but certainly not least of all, I would like to thank my wife, Arlene, for her patience and support in every way, during the past two years.

TABLE OF CONTENTS

LIST OF TABLES

LIST OF ILLUSTRATIONS

FIGURE PAGE

FIGURE PAGE

SUMMARY

The decays of mass-separated (2.4, 2.2 min) ^{187m,g}Hg and (8.4 min) ^{187}Au have been studied using the University Isotope Separator at Oak Ridge (UNISOR) facility operated on-line to the Oak Ridge Isochronous Cyclotron. Conventional methods of gamma-ray and conversion electron spectroscopy measurements in singles, multiscaling, and coincidence modes were used. Both high- and low-spin states in ^{187}Au are fed in the ($^{+}$,EC) decay of ^{187m,g}Hg isomers. The $h_{11/2}$ $h_{9/2}$, $s_{1/2}$, $d_{3/2}$, and $d_{5/2}$ collective bands, which are systematically observed throughout the odd-mass gold isotopes, are now extended to ^{187}Au. In ^{187}Au, the $h_{9/2}$ bandhead is below the $h_{11/2}$ bandhead, and the transition between the two is found to proceed via a hindered M1 transition due to the change in nuclear shape involved in the transition.

The high-spin, unique parity states in the odd-mass gold nuclei are readily described by a triaxial rotor model, with the ordering of energy levels and electromagnetically transition probabilities quantitatively reproduced. Moreover, it is found that the energy levels of the normal (positive) parity states in ^{187}Au are also qualitatively described by this model. One of the most important results of the present study is the discovery of the coupling of the odd proton in an $h_{9/2}$ particle state to the excited 0^{+} state of the ^{186}Pt core. Transitions with E0 components are found which feed the 9/2- and 13/2- members of the "first" $h_{9/2}$ band, thus defining the 9/2- and 13/2- members of the "second" $h_{9/2}$ band and suggesting a third shape isomer (in addition

to the couplings $h^{-1}_{11/2} \otimes {}^{188}Hg(0^+_1)$ and $h_{9/2} \otimes {}^{188}Pt\ (0^+_1)$ in ^{187}Au. The nature of the 0^+_2 state in ^{186}Pt is not understood at present, but it appears, from the coupling of the $h_{9/2}$ proton particle seen in the present study, that an additional shape degree of freedom is needed to explain this state. Candidates for Nilsson states coupled as holes to the deformed prolate excited 0^+ state in the ^{188}Hg core have also been found. These Nilsson states would suggest a fourth shape isomer in ^{187}Au. The four isomers in ^{187}Au confirmed or suggested by the present study have energies, spin-parity assignments, and halflives of: (1) 121 keV, 9/2-, $T_{1/2}$>50 ns (the transition depopulating this isomeric level is not observed in the coincidence data, i.e., its lifetime is longer than that observable in the timing range of the present study, but it is observed in the singles data); (2) 224 keV, 11/2-, $T_{1/2}$ = 48.0 ± 4.8 ns; (3) 444 keV, 9/2-, halflife not measured; and (4) 620 keV, 11/2- (possibly the 11/2- [505] Nilsson state), halflife not measured.

Only the low-spin states in ^{187}Pt appear to be populated in the beta decay of ^{187}Au. The nature of these low-spin states is not understood at present. The location of the $i_{13/2}$ neutron band relative to the ground state is not known. Low-spin members of this band appear to be populated in the present study since the gamma ray depopulating the $11/2^+$ bandhead is observed. One aspect of the levels of ^{187}Pt not previously reported is a delayed transition of 251 keV energy observed in the present study. Due to poor statistics, however, its lifetime is not measured in the present work. This study will provide a basis for future studies on the levels of ^{187}Pt.

CHAPTER 1

INTRODUCTION

Although much progress has been made in nuclear structure study in the past 30 years, the actual nucleon-nucleon interaction is still not sufficiently understood to account for the variety of phenomena observed in nuclei starting with a microscopic approach. Therefore, approximate nuclear models have been developed to describe nuclear structure. The simple shell model (see, e. g., ref. 1) was the first model to succeed in describing a variety of properties for a broad range of nuclei. Those nuclei far removed from closed shells, however, were found to exhibit collective behavior which led Bohr and Mottelson [2,3] to develop a collective model. Between these two extremes is the transitional region to which the two nuclei of the present study belong. In this region, the nuclei are only weakly deformed and Coriolis effects[4] and asymmetric shapes[5,6] have recently been found to play an important role.

Both vibrational and rotational collective phenomena are observed in nuclei. Thus both rotational and vibrational models have been applied to the transitional nuclei (see, e. g., refs. 4-9). In addition to these approaches, the full collective Hamiltonian of ref. 2 has been numerically solved and applied to the transitional region[10]. Each approach has had limited success, and it appears that only a model which accounts for both vibrations and rotations will successfully describe the

transition region. The rotation-aligned model[4] and the asymmetric rotor model[5,6], however, have been quite successful in their description of transitional nuclei, especially on the high-spin, unique parity levels. The asymmetric rotor model for odd-A nuclei as modified by Meyer ter Vehn[5,6] is the one used as the theoretical basis of the present study due to its simplicity.

Since the validity of any nuclear model depends on its ability to reproduce experimentally observed phenomena, detailed experimental studies of the nuclei to which the model is applied provide the crucial tests of the theoretical predictions. The present work extends previous ONISOR studies of the light odd-mass gold isotopes[11] to include ^{187}Au and forms the beginning of a study of the light odd-mass platinum isotopes. It not only extends several features systematically observed in the gold nuclei, but also encounters some results previously unobserved in $^{189\text{-}195}$Au.

Earlier studies of the ^{187}Pt nucleus can be roughly classified as low-spin studies from ^{187}Au decay and high-spin in-beam studies. The ground state spin of ^{187}Pt (3/2) has been measured by Rubinsztein and Gustafsson[12], Ekström et al.[13], and Berkes et al.[14]. Early decay studies[15] assigned seven gamma rays to ^{187}Au decay and reported the halflife for ^{187}Au as 8.5 min but did not give a decay scheme. Simultaneous in-beam reaction spectroscopy studies of ^{187}Pt and studies of mass-separated ^{187}Au decay have yielded information on low- and high-spin states in ^{187}Pt[16,17]. Mass-separated ^{187}Au decay studies by Bourgeois et al.[18] have also yielded low-spin information. The lifetimes and multipolarities of transitions between the low-spin, low energy states

have been reported by Bourgeois et al.[19]. Beta strength functions of ^{187}Au decay have been deduced by Hornshøj et al.[20] and Duke et al.[21]. Finally, in-beam studies have provided information on the $i_{13/2}$ neutron band structure[22-25] including the measurement of the bandhead spin[22] and lifetime[23,25], and have also indicated several negative parity cascades[22]. The present study adds to the previous low-spin studies.

Decay studies of ^{187}Hg by Finger et al.[15] reported ten gamma rays with halflife $T_{1/2}$ = 2.4 min and two gamma rays with $T_{1/2}$ = 1.8 min. Of the two gamma rays with 1.8 min halflife, one has been identified in the present study with a halflife of 2.4 min. All ten gamma rays with $T_{1/2}$ = 2.4 min are seen in the present work. Berg et al.[26] and Deleplanque et al.[27] report a 103 keV isomeric transition in ^{187}Hg decay with $T_{1/2}$ = 50 ns. This transition is observed in the present study with the same halflife, within experimental error (see Chapt. IV). The ground state spin of ^{187}Au (1/2) has been measured by Ekström et al.[28]. Heiser et al.[29] reported an E3 isomeric transition in ^{187}Au with $T_{1/2}$ = 142 ms, but no line of the reported energy (166 keV) is observed in the present work. The most recent study of ^{187}Hg decay is that of Bourgeois et al.[30] who assign 70 gamma rays to the decay and place 49 of these in an energy level scheme. Of the 70 gamma rays assigned, 45 have conversion coefficients and probable multipolarity assignments reported. They report a halflife of 133 sec for both the ground state and the 13/2+ isomeric state in ^{187}Hg and report $T_{1/2}$ = 50 ± 8 ns for the 103 keV isomeric transition in ^{187}Au. Alpha decay studies[31] on ^{187}Hg report two alpha branches with halflife 2.4 ± 0.3 min and 1.9 ± 0.3 min. In much earlier studies, Albouy et al.[32] measured the halflife

of ^{187}Hg as 3 min and Hansen et al.[33] reported three gamma rays, which are seen in the present work, and mentioned the observation of others, but did not report a decay scheme. The present study builds upon the results of these earlier investigations and is, for the most part, in agreement with them, but makes a number of major additions.

The four primary goals of this research are:

1) Search for the coupling of the $h_{9/2}$ proton particle state in ^{187}Au to the excited 0^+ state of the ^{186}Pt core.
2) Search for the coupling of the odd proton in ^{187}Au to the deformed excited 0^+ state of the ^{188}Hg core, i.e., establish the existence of Nilsson states in ^{187}Au.
3) Extend the systematics of the $h_{9/2}$, $h_{11/2}$, $s_{1/2}$, $d_{3/2}$, and $d_{5/2}$ collective bands to ^{187}Au and use these bands to test the asymmetric rotor model of odd-A nuclei.
4) Measure the low-spin states in ^{187}Pt populated in the decay of ^{187}Au.

Chapter II develops the theoretical basis of this study. Chapter III discusses the experimental facilities and procedures. Chapter IV presents the data analysis in tabular and graphic form. Chapter V presents the interpretation of the results, gives a brief summary, and suggests future measurements.

CHAPTER II

NUCLEAR MODELS

The study of nuclear structure is the study of a many-body problem in which the laws governing the interactions between the particles (the nuclear forces) are not well known. Because nuclear forces are not understood, and since the many-body problem has no simple solution, simplifying assumptions based on empirical evidence are made. Each set of assumptions leads to a specific nuclear model. The ultimate goal of nuclear structure theory is to develop a unified model which works equally well throughout the chart of nuclides. At present, there are many models, each of which has a limited scope of applicability. After an historical introduction, this chapter presents the models which describe the types of nuclei studied in the present work.

Single Particle Models

The first model to predict successfully nuclear properties for a broad range of nuclei was the shell model developed by Mayer, Jensen, Haxel, and Suess (see, e.g. ref. 1). This model replaces the interaction between the A^{th} nucleon and the other A-1 nucleons with an average single-particle potential and includes a strong spin-orbit interaction. The model successfully predicts the nuclear "magic numbers", many ground state spins and parities, islands of isomerism, and magnetic moments of nuclei. It can not, however, account for the low-lying energy levels and large static quadrupole moments seen experimentally in many nuclei

away from closed shells. Thus Nilsson[34] extended the shell model to include permanent deformation by using an axially symmetric potential:

$$H = \frac{\vec{p}^2}{2m} + \frac{m}{2}\left[\omega_\perp^2 (x^2+y^2) + \omega_z^2 z^2\right] + C\,\vec{\ell}\cdot\vec{s} + D\,\vec{\ell}^2 \qquad (2\text{-}1)$$

The parameters C, D, $\omega_\perp$ and ω_z are determined empirically and m is the nucleon mass. The $\vec{\ell}^2$ term has the effect of flattening the oscillator well into a more box-like shape and lowering the energies of the high angular momentum states relative to those predicted by a simple harmonic oscillator potential. The oscillator constants $\omega_\perp$ and ω_z are related by requiring nuclear volume conservation. Several articles[35,36,37] examine the volume conservation conditions and give expressions relating the different shape parameters used in the literature.

Neglecting the spin-orbit and $\vec{\ell}^2$ terms, the energy eigenvalues are

$$E_N = (n_\perp + 1)\hbar\omega_\perp + (n_z + \tfrac{1}{2})\hbar\omega_z \qquad (2\text{-}2)$$

$$N = n_\perp + n_z$$

where n_z and $n_\perp$ are the total number of oscillator quanta along and perpendicular to the z-axis, respectively. The usual notation for labelling Nilsson states is with the "asymptotic" quantum numbers: $N=n_\perp+n_z$, n_z, $\Lambda = \ell_z$, the z-component of the orbital angular momentum, and Σ, the z-component of the spin (where z is chosen to be the symmetry axis). None of these are good quantum numbers but as the deformation $|\varepsilon|$ increases, the eigenvectors of the Nilsson Hamiltonian asymptotically approach $|N\, n_z \Lambda\Sigma\rangle$. With the inclusion of $\vec{\ell}\cdot\vec{s}$ in the Hamiltonian, the z-component of the total angular momentum,

$$j_z - \lambda + \quad = \tag{2-3}$$

remains a good quantum number in the model as does the parity

$$\pi = (-1)^N. \tag{2-4}$$

Thus the complete set of quantum numbers for a Nilsson state is

$$\pi[N\ n_z\ \Lambda]. \tag{2-5}$$

The Nilsson Hamiltonian, as written in Eq. 2-1, accounts only for quadrupole deformations. In addition to quadrupole deformation, hexadecapole deformation has been considered[38,39]. Kleinheinz et al.[38] give a very lucid description of the effects of hexadecapole deformation on the Nilsson levels. A deformation parameter, ε_4 or α_4, is then needed in addition to ε or β to define the potential. It is noted that Nilsson states have been shown recently to exist in the region of interest in the present work[40,41,42], despite the proximity of this region to the Z=82 closed shell. Axially asymmetric potentials are discussed below.

Collective Models

Both the shell model and the Nilsson model are single particle models. A model incorporating collective nuclear motion has been developed by Bohr and Mottelson[2,3]. The collective motion consists of shape oscillations of the nuclear surface about an equilibrium spherical shape (the vibrational model), or of rotations of the nucleus as a permanently deformed rigid body (the rotational model). Bohr[2] expresses the nuclear surface

$$R(\theta,\phi) = R_0 \left(1+\sum_{\lambda,\mu} \alpha_{\lambda\mu} Y_{\lambda\mu}(\theta,\phi)\right) \qquad (2\text{-}6)$$

where R_0 is the nuclear radius in its spherical equilibrium shape, $Y_{\lambda\mu}(\theta,\phi)$ are normalized spherical harmonics, and $\alpha_{\lambda\mu}$ are coordinates describing the deformation of the nuclear surface. Expressing the potential energy of deformation in terms of the coordinates $\alpha_{\lambda\mu}$, and the kinetic energy in terms of the generalized conjugate momenta, $\pi_{\lambda\mu}$, the Bohr Hamiltonian can be written

$$H = \frac{1}{2} \sum_{\lambda,\mu} \left(\frac{1}{B_\lambda} |\pi_{\lambda\mu}|^2 + C_\lambda |\alpha_{\lambda\mu}|^2 \right). \qquad (2\text{-}7)$$

This is just the Hamiltonian of a system of harmonic oscillators with frequencies

$$\omega_\lambda = \sqrt{\frac{C_\lambda}{B_\lambda}} \qquad (2\text{-}8)$$

where the C_λ's are analogous to classical spring constants, and the B_λ's are analogous to classical masses.

In the vibrational limit of the collective model, the energy levels and parity are

$$E = \sum_\lambda n_\lambda \hbar\omega_\lambda \qquad \pi = (-1)^\lambda \qquad (2\text{-}9)$$

where n_λ is the number of surface quanta of order λ with energy $\hbar\omega_\lambda$. Experimentally, only $\lambda = 2, 3$ have been seen at low energies. The ground state is then a state with no quanta present, a 0^+ state; the first excited state has one $\lambda = 2$ quantum, a 2^+ state; and the second

excited state has either one $\lambda = 3$ quantum, a 3^- state, or two $\lambda = 2$ quanta, a degenerate 0^+, 2^+, 4^+ triplet of states (see Fig. 2-1). This vibrational limit has met with some success describing even-even nuclei near closed shells (see e.g., ref. 43).

In the rotational limit of the Bohr-Mottelson model, the Hamiltonian for rotations built on the ground state of even-even nuclei is just that of a rigid rotor. The energy eigenvalues are

$$E_I = \frac{\hbar^2}{2\mathcal{I}_0} I(I+1) \qquad (2\text{-}10)$$

where $\mathcal{I}_0$ is the moment of inertia and I, the angular momentum quantum number, can have only even integral values in order to symmetrize the wavefunctions properly.

The rotational model for even-even nuclei has been extended by Davydov and co-workers (see, e.g., ref. 44 and references therein) to include rigid axially asymmetric, or triaxial, shapes. The major change in the energy spectrum of a rigid triaxial rotor is the appearance of new states of angular momentum 2, 3, 4, . . . at low energy. The shape of the nucleus is defined[45]) by the deformation parameter β ($\beta = 0$ is spherical, $\beta > 0$ is prolate, and $\beta < 0$ is oblate) and the asymmetry parameter γ ($0^o \leq \gamma < 30$ is prolate and $30^o < \gamma \leq 60^o$ is oblate). As the nuclear shape deviates more from axial symmetry, the new states decrease in energy. Low-lying 2_2^+ and 3_1^+ states (where the notation 2_2^+ indicates the second lowest 2^+ state observed) are thus characteristic of a triaxial rotor.

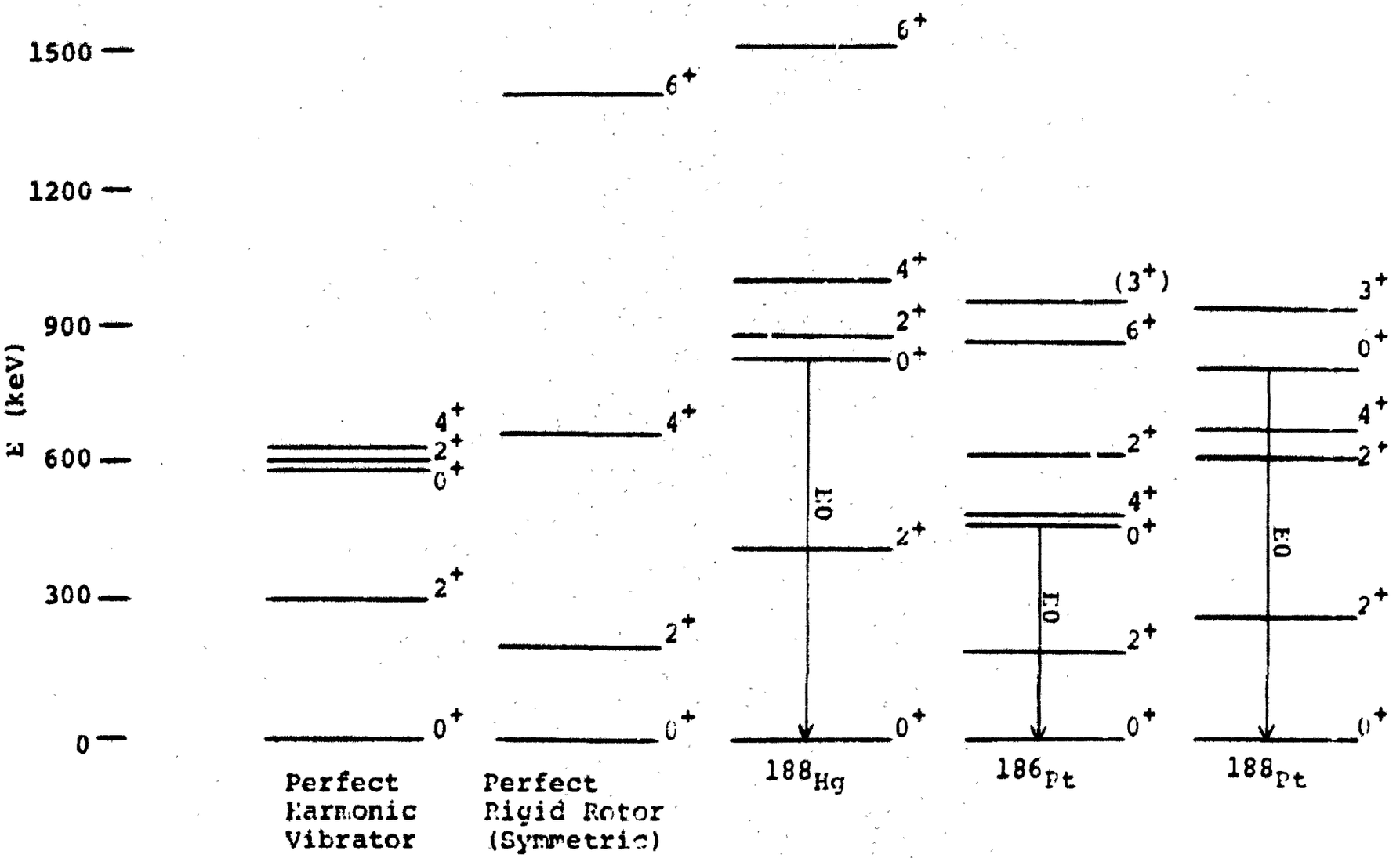

Figure 2-1. Even-Even Core Spectra for the Nuclei of the Present Study and Examples of the Energy Spectra for a Perfect Harmonic Vibrator and a Perfect Rigid Rotor. Although the ^{188}Hg and $^{186,188}Pt$ spectra resemble vibrational spectra, the existence of strong E0 transitions between the 0^+ states, and other structures not included in the figure, indicate that they are not vibrators. The experimental spectra are taken from refs. 70 (^{188}Hg) and 71 ($^{186,188}Pt$).

Residual Interactions

Both the shell and collective models fail to account for few-nucleon correlations. One very important correlation results from the residual pairing interaction, an attractive force between like nucleons which favors the correlations of nucleon pairs in time-reversed single-particle states. The pairing intereaction is readily treated by the occupation number or second-quantization formalism (see, e.g., refs. 46 and 47). The monopole pairing energy for a single j-shell is given by

$$V_{pair} = - G \sum_{m\bar{m}'} a^{+}_{jm} \; a^{+}_{j\bar{m}} \; a_{j\bar{m}'} \; a_{jm'} \qquad (2\text{-}11)$$

where a^{+}_{jm} (a_{jm}) are creation (annihilation) operators for a particle state $|j\ m\rangle$, $\bar{m}$ denotes the time-reversed state and G is defined below. This formalism, applied by Bardeen, Cooper, and Schrieffer (BCS) to superconductivity[48], was first applied to nuclei by Bohr, Mottelson, and Pines[49]. The BCS theory introduces four parameters: Δ is the pairing energy gap parameter (2Δ is related to the neutron separation energies by $2\Delta = S_n(A+1) - S_n(A)$, where A denotes an even-z, odd-N nucleus and A+1 denotes an even-even nucleus), λ is the Fermi energy, and U_ν and V_ν are variational parameters where U^2_ν and V^2_ν represent the probability that state ν is unoccupied and occupied, respectively. The parameters are related by:

$$U^2_\nu + V^2_\nu = 1,$$

$$V^2_\nu = \frac{1}{2}\left[1 - \frac{e_\nu - \lambda}{(e_\nu-\lambda)^2 + \Delta^2}\right] \qquad (2\text{-}12)$$

$$\Delta = G \sum_\nu U_\nu V_\nu, \text{ and}$$

$$E_\nu = (e_\nu - \lambda)^2 + \Delta^2 ,$$

where e_ν are the single-particle energy eigenvalues and G is the pairing force strength parameter. This theory leads to the concept of a quasiparticle: a mixture of a particle state ν with amplitude U_ν and a hole state $-\nu$ with amplitude V_ν. Far below the Fermi surface the quasiparticle behaves like a hole, far above it like a particle. An unpaired nucleon in state ν blocks that state from occupation by a nucleon pair, due to the Pauli exclusion principle, thus disrupting pairing correlations and modifying the single particle energies through this disruption.

In addition to the monopole pairing term (Eq. 2-11), there can be higher order multipole pairing correlations[50]. In particular, quadrupole pairing has been explored in the transition region[51] and the actinide region[52,53,54]. The pairing Hamiltonian that includes monopole and quadrupole pairing can be written[51].

$$H_P = -g_0 P_0^\dagger P_0 - g_2 P_2^\dagger P_2 , \qquad (2\text{-}13)$$

where

$$P_0^\dagger = \Sigma a_\nu^\dagger a_\nu^\dagger , \qquad P_2^\dagger = \Sigma q_{\nu\nu} a_\nu^\dagger a_\nu^\dagger$$

and $q_{\nu\nu}$ are matrix elements of the quadrupole pairing operator. The monopole pairing gap parameter, $\Delta = \Delta_0$, is assumed to be independent of the states between which the paired particles scatter. With the inclusion of quadrupole pairing, the gap parameter becomes state dependent:

$$\Delta_\nu = \Delta_\nu + G_2 \sum_\nu q_{\mu\nu} U_\mu V_\nu \qquad (2\text{-}14)$$

The quadrupole pairing force is important in regions where many down-sloping and up-sloping Nilsson orbitals cross, e.g., $\epsilon \sim 0.2$, $Z = 80$ (see Fig. 2-2). The matrix elements representing the scattering of a pair between oblate (up-sloping for $\epsilon > 0$) and prolate (down-sloping for $\epsilon > 0$) orbitals is weaker than the matrix elements for scattering the pair between like orbitals. Therefore, in regions like $\epsilon = 0.2$, $Z = 80$, there is a relative weakening of the total pair correlation energy, and the potential energy surface minimum tends to move away from this deformation to restore the pairing energy (see, e.g., Fig. 10 of ref. 51). The quadrupole pairing correlation also manifests itself in pairing isomers which have enhanced two-nucleon transfer cross sections (see, e.g., ref. 50 and references therein) and a reduced blocking effect for coupling to unpaired nucleons, e.g., the 0_2^+ state in the uranium isotopes[55].

Odd-A Nuclei

Collective models have been extended to include odd-A nuclei by coupling the odd nucleon to collective states of an even-even core. In the weak coupling limit, the odd-A spectrum consists of degenerate sets of levels at the core energy spacings. Each set consists of levels of all possible angular momenta obtained by coupling the odd nucleon angular momentum to the core angular momentum. Thus, an $h_{9/2}$ nucleon coupled to a 2^+ core state in the weak coupling limit yields degenerate 13/2, 11/2, 9/2, 7/2, and 5/2 states at the core 2^+ energy.

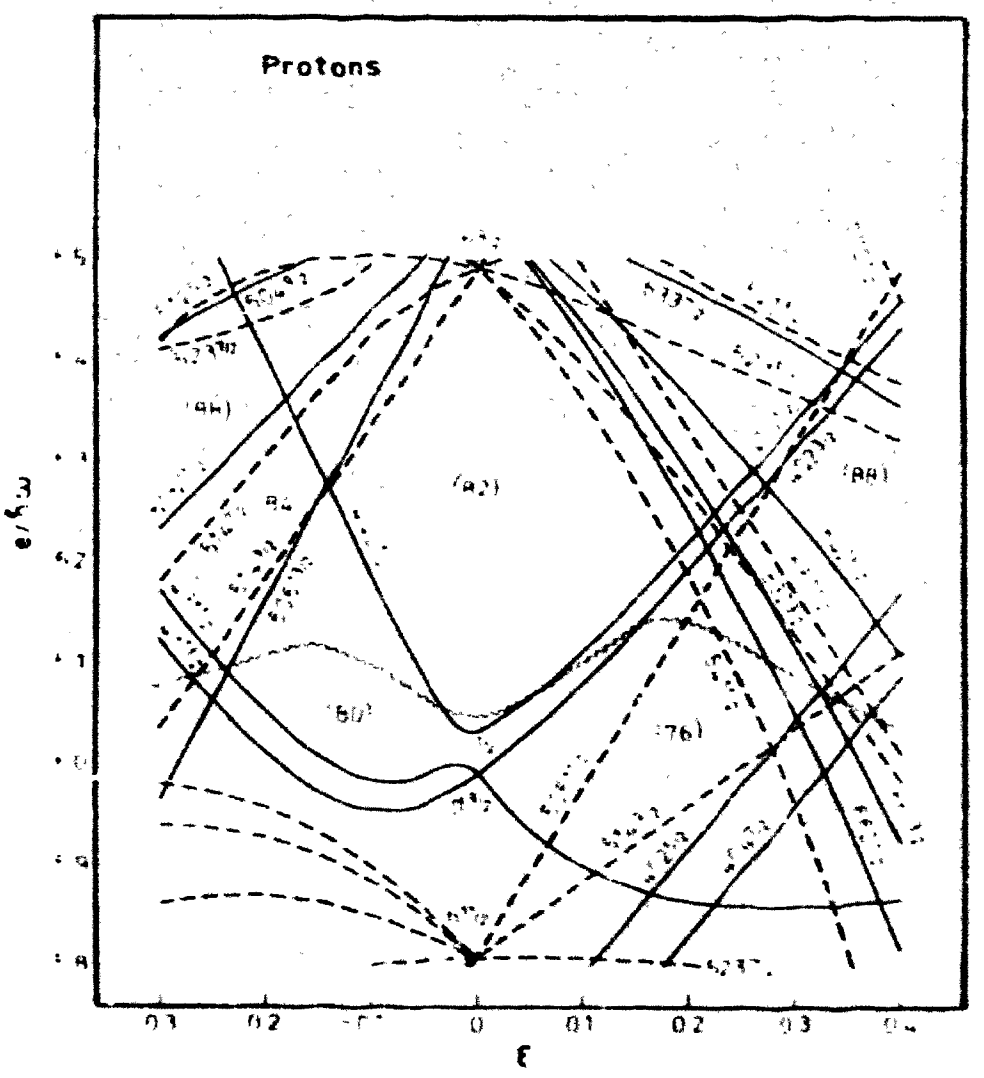

Figure 2-2. Nilsson Levels for Protons in the Z = 82 Closed Shell Region. Note the large number of up-sloping and down-sloping level crossings near ϵ = 0.2 and Z = 80.

Coupling an odd nucleon to quadrupole vibrations (= 2 in Eq. 2-7) can be described by the Hamiltonian

$$H = H_v + H_{int} \tag{2-15}$$

where H_c is the core Hamiltonian and the interaction between particle and core is

$$H_{int} \propto \hat{q} \cdot \hat{Q} \tag{2-16}$$

where q (Q) is the single-particle (core) quadrupole operator given by

$$\hat{q}_\mu = r^2 Y_{2\mu} \tag{2-17}$$

If $H_{int} = 0$, the weak coupling limit described above results in degenerate sets of levels at the core energy spacings. H_{int} removes the degeneracy (see Fig. 2-3). The effect of H_{int} on the odd-A energy spectrum depends on its sign and magnitude (see Fig. 2-3). For $\hat{q} \cdot \hat{Q} < 0$, the level order resulting from coupling the odd particle to the 2_1^+ state tends toward the strong coupling limit (j, j+1, j+2, . . .)[7,8]. For $\hat{q} \cdot \hat{Q} > 0$, the level order tends toward the decoupled limit (j, j+2, . . .)[7].

Let us consider an odd nucleon coupled to an axially symmetric rigid rotor in the strong coupling limit. If the odd-particle angular momentum j is added to the rotational angular momentum R to give the total nuclear spin I (see Fig. 2-4),

$$I = R + j, \tag{2-18}$$

the rotational limit of the Bohr Hamiltonian results in the energy spectrum

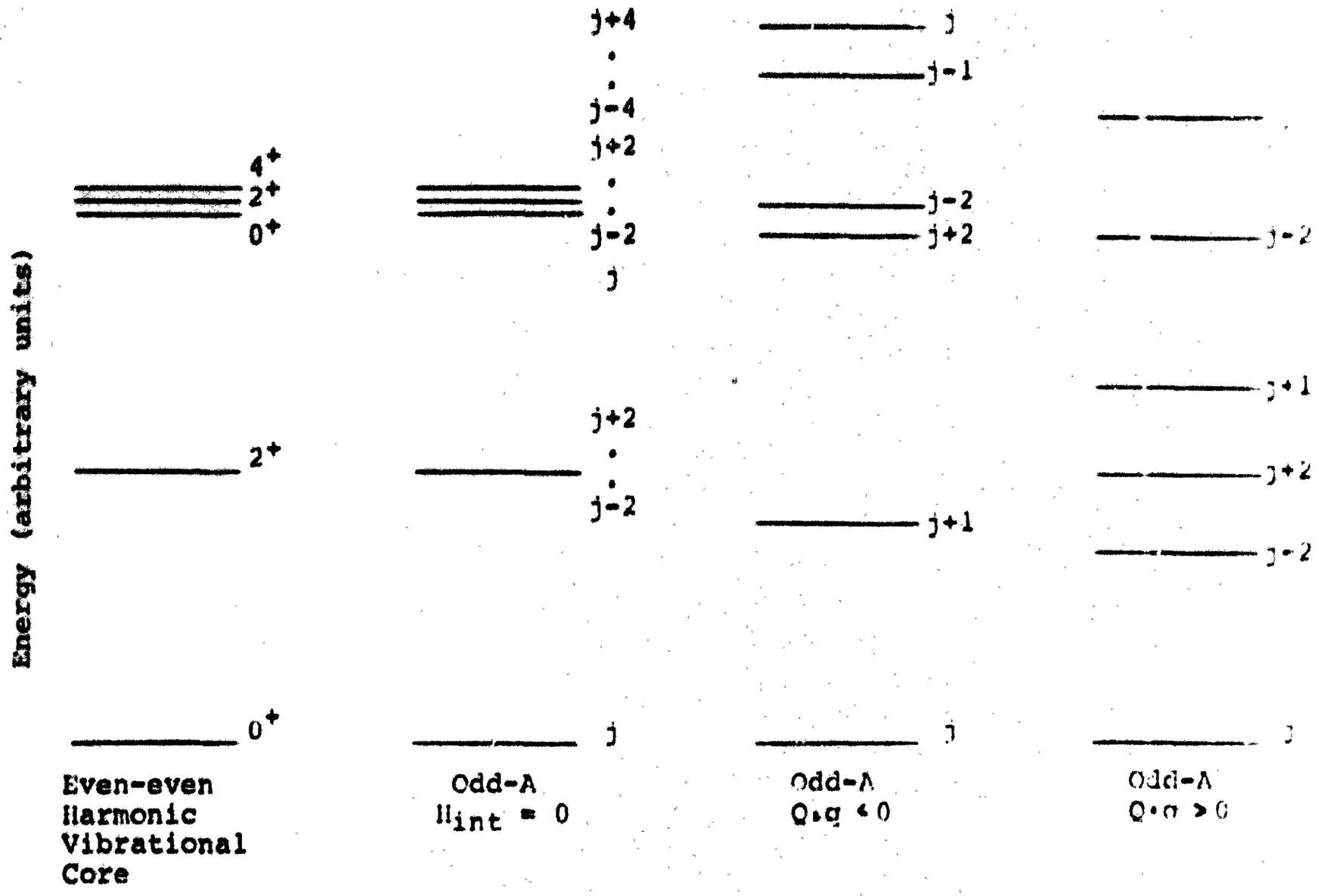

Figure 2-3. Odd-A Particle-Vibrational Core Coupling Schemes. The odd particle angular momentum is j; Q(q) is the core (particle) electronic quadrupole moment.

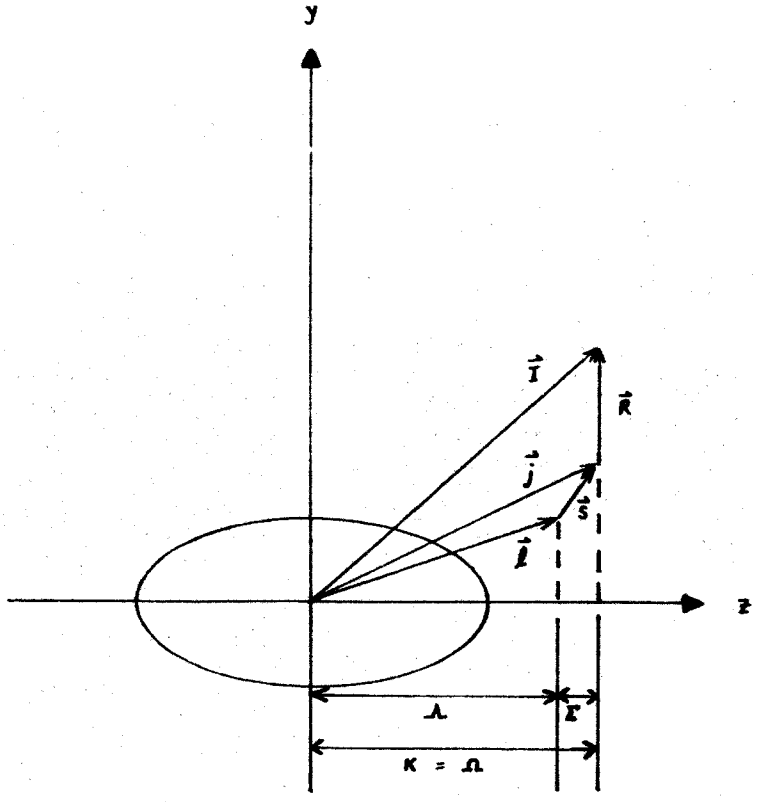

Figure 2-4. Diagrammatic Representation of the Coupling of an Odd Nucleon, with Angular Momentum $\vec{j}$, to a Symmetric Rotor, with Angular Momentum $\vec{R}$, to a Resultant Angular Momentum $\vec{I}$. The odd-particle orbital angular momentum and spin are $\vec{\ell}$ and $\vec{s}$, respectively, and their projections on the symmetry axis are Λ and Σ , respectively.

$$E_{IK} = \epsilon_K + \frac{\hbar^2}{2\mathcal{I}} [I(I+1) + a\delta_{K,1/2}(-1)^{I+1/2}(I+1/2) - 2K^2] \quad (2\text{-}19)$$

where a is called the decoupling parameter, $K = I_3$, and ϵ_K are the single-particle energies. Therefore, the energy spectrum consists of rotational bands built on each single-particle state. The term in Eq. 2-19 involving the decoupling parameter, a, arises from Coriolis effects discussed later. Eq. 2-19 is valid only if the odd particle is strongly bound to the core, i.e., it is deformation-aligned. In this limit, the rotational bands built on each single-particle state exhibit strong coupling, and $j_3 = \Omega = K = I_3$ is a good quantum number. The term involving a only enters Eq. 2-19 when $K = 1/2$ because all other values of K contribute only small, off-diagonal terms for a deformation-aligned particle.

If, however, the particle does not rotate with the core, i.e., if j is rotation aligned, Coriolis effects are large. The Coriolis term

$$H_{cor} = -2\frac{\hbar^2}{2\mathcal{I}} I \cdot j \quad (2\text{-}20)$$

is largest for small $\mathcal{I}$ (small deformation), large j, and/or large I. Stephens[4] has solved the Hamiltonian:

$$H = H_A + A[I(I+1) - K^2] - 2A[I_x j_x + I_y j_y] + A[j_x - \alpha]^2 \quad (2\text{-}21)$$

for cases where Coriolis coupling is large. Here H_p is the single-particle Hamiltonian and $A = \hbar^2/2\mathcal{I}$. The resulting energy expression for $I \geq j$ is

$$E(I,j,\alpha) = \epsilon_j + A[(I-\alpha)(I-\alpha+1) + j(j+1) - \alpha^2] \quad (2\text{-}22)$$

when ε_j is the single-particle energy and Ω is the projection of j on the rotation axis. The lowest lying band is decoupled with $\Omega = j$.

The nuclei studied in the present work have certain single-particle states of high angular momentum coupled to cores with small deformation so that Coriolis effects are expected to be large. The even-even core spectra for these nuclei are shown in Fig. 2-1. From Eqs. 2-4 and 2-5, it can be seen that the E_{4+}/E_{2+} ratios for pure vibrators and pure rotors are 2.0 and 3.3, respectively. From Fig. 2-1, the E_{4+}/E_{2+} ratios are seen to be between 2.4 and 2.6. Therefore, these belong to the transitional nuclei lying between the rotational and vibrational regions. Also evident in Fig. 2-1, at least for the platinum cores, are low-lying 3^+ states, implying triaxial shapes. Therefore, a rotational description of the nuclei studied in the present work should include a triaxial shape degree of freedom.

Paar et al.[56]) have used a vibrational model to describe ^{193,195}Au. In this model, a cluster of three proton holes is coupled to quadrupole vibrations. The three proton hole cluster is used to describe normal parity states (positive parity for gold nuclei) and also the unique parity states (negative parity for gold nuclei) built on the $h_{11/2}$ state. To describe the $h_{9/2}$ band, however, rather than use a four hole-one particle cluster, which would complicate the calculations, they couple one j = 9/2 particle to the quadrupole vibrations of the neighboring platinum nuclei.

Tanaka and Sheline[8]), Donau and Frauendorf[57]), and Leander[10]) have studied the transitional nuclei in terms of the particle-core

coupling model. Tanaka and Sheline[8] treat the core as γ-stable (triaxial), γ-vibrational, axially symmetric and spherically vibrational. Their results are in fair agreement with experiment for the transitional nuclei with A = 197-199. In particular, they examine the $h_{11/2}$ proton system in $^{189-195}$Au and note that the removal of one proton from the even-even Hg cores seems to increase the collectivity of the γ-degree of freedom, since the inclusion of the γ-degree of freedom in the core reproduces the experimental spectra better than a symmetric rotor model. The $h_{9/2}$ band in ^{189}Au is also better reproduced by including the γ-degree of freedom.

Donau and Frauendorf[57] treat the core as a triaxial rotor (γ = 30°) and as γ-unstable but treat the odd nucleon as a quasiparticle. They consider the coupling of an $h_{11/2}$ quasiparticle to both cores and find similar behavior for each core. They also report similar results for the $i_{13/2}$ quasiparticle band in ^{191}Pt and conclude that the odd quasiparticle is not sensitive enough to distinguish between the two types of cores considered. The Leander calculations[10] are discussed below.

The first extension of the asymmetric rotor[44] to odd-A nuclei in the gold region was made by Hecht and Satchler[58]. They used the adiabatic approximation in which the odd nucleon is considered to be in a definite single-particle state, i.e., it is a single-j model. As pointed out in ref. 58, the nuclei to which this model is applied should have large asymmetry and a well defined equilibrium shape.

Recently, Vieu et al.[59,60] used an extended Hecht and Satchler model, which includes an arbitrary number of Nilsson orbitals

simultaneously, i.e., a mixed-j model. They use it to describe the positive parity states and the $h_{11/2}$ system of states in $^{193-199}$Au. Their calculated wavefunctions show significant amounts of K-mixing in the positive parity states, as would be expected for loss of axial symmetry, which they use to explain the existence of interband transitions which are as intense as intraband transitions in these nuclei. These results, and their relation to the ^{187}Au nucleus studied in the present work, are discussed in Chapter V.

Meyer ter Vehn[5,6] has also extended the asymmetric rotor model to odd-A nuclei and applied it to nuclei in the gold region. This triaxial rotor model differs from that of Hecht and Satchler[58] in that a complete j-level is used for the single-particle configuration space, and it also differs from a similar model by Pashkevich and Sardaryan[61] in that it treats the odd nucleon as a quasiparticle, thus including pairing correlations. The Meyer ter Vehn model is applied specifically to unique-parity, high-j states ($h_{9/2}$, $h_{11/2}$ proton states and $i_{13/2}$ neutron states) which exist in the A = 190 region. The model can account for the transition from decoupled particle bands to strongly coupled particle bands as the asymmetry parameter, γ, varies from 0^o (prolate) to 60^o (oblate) throughout the triaxial region. Such a transition is seen to occur in the $h_{9/2}$ bands in the odd mass gold isotopes[26] (Fig. 2-5). The model is also successful in describing the spin sequence of the energy levels not only for the favored (j+2, j+4, j+6, . . .) decoupled levels, but also for the unfavored (j+1, j+3, j+5, . . .) levels. Both the favored and unfavored levels are populated in the beta decay experiments of the present work, so they provide a test for the validity of the model.

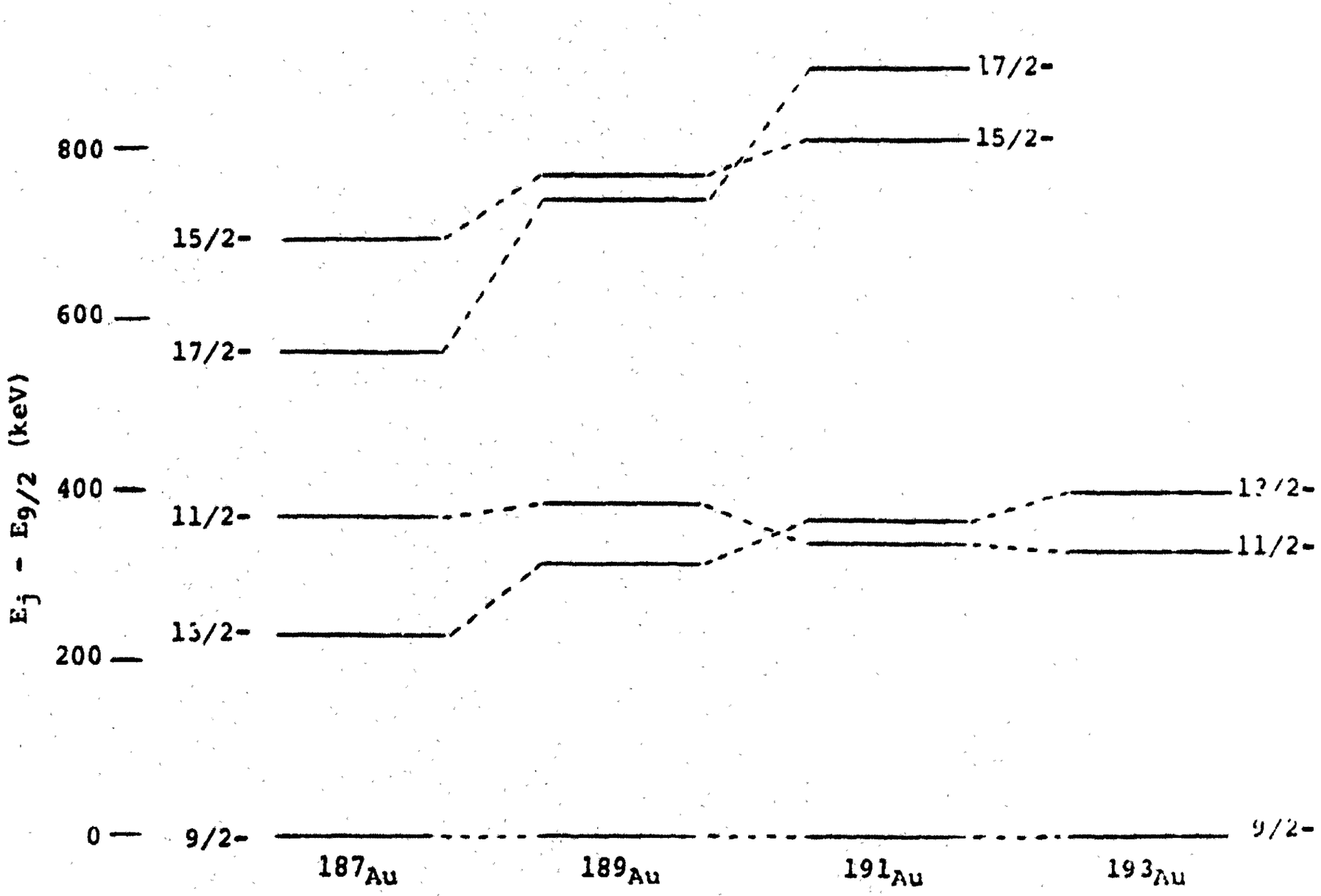

Figure 2-5. Partial Systematics of the $h_{9/2}$ Level System for ^{187} - ^{193}Au Showing the Transition from a Strongly Coupled Pattern to a Decoupled Pattern as the Isotopes Become More Neutron Deficient. The spectra are taken from refs. 72 (^{189}Au), 89 (^{191}Au) and 26 (^{193}Au).

One of the shortcomings of the Meyer ter Vehn model is an observed compression of the experimental energy spectrum as compared to the predicted spectrum. This is especially true of the high-spin states and is the result of assuming a rigid shape. A more realistic approach is taken by Toki and Faessler[62,63] who use a variable moment-of-inertia (VMI) model. Their results are in much better agreement with experiment for the high-spin states in the cases they consider. Faessler and Toki[64] have also extended the triaxial rotor model to include mixed-j calculations. They apply this model to the mixed $h_{9/2}$ and $f_{5/2}$ proton single-particle levels in ^{187}Ir and achieve better agreement with experiment for the low-spin ($I < 9/2$) states in the $h_{9/2}$ band than either their VMI model or the Meyer ter Vehn calculations. A semi-microscopic model for the $h_{11/2}$ system in ^{195}Au has also been developed by Hecht[65].

Leander[10] has studied the odd-mass transitional nuclei by coupling the odd nucleon to core states obtained from numerical diagonalization of the Bohr collective Hamiltonian (Eq. 2-3). He points out that the odd particle may have a large polarizing effect on the core due to the minima in the core potential being insufficient to stabilize the core deformation. He also points out that the core can assume various shapes for different states in the same odd-mass nucleus due to instability of the minima in the γ-degree of freedom. This model is as successful as the Meyer ter Vehn model in describing the transition from prolate to oblate shapes through the triaxial region. The parameters in Leander's model are those associated with the potential energy, $V(\beta,\gamma)$, and the inertia parameter, B (see Eq. 2-7). The potential energy parameters have been well explored (see, e.g., refs. 66, 67, 68).

Recently the inertial parameters (or inertial functions) have been explored by Pomorski et al.[69]. They find rather large fluctuations of the inertial parameters across the β - γ plane. These fluctuations in the inertial parameters are discussed further in Chapter V relative to the ^{187}Au nucleus.

CHAPTER III

EXPERIMENTAL SYSTEMS AND METHODS

All experimental work was performed at the University Isotope Separator Oak Ridge (UNISOR) facility which is operated on-line to the Oak Ridge Isochronous Cyclotron (ORIC) at Oak Ridge National Laboratory (ORNL) in Oak Ridge, Tennessee. UNISOR is a consortium of 14 member institutions and was formed primarily for the investigation of nuclei far from stability [73]. Detailed descriptions of the UNISOR separator and the ORIC cyclotron can be found in refs. 74, 75, respectively.

Source Production

Radioactive sources are produced at UNISOR by the continuous bombardment of a target in the UNISOR ion source [76] by the ORIC heavy-ion beam and the continous extraction of the reaction products to the separator. The separated beam travels down the beam pipe and is collected on aluminum coated Mylar tape (Fig. 3-1). After a preset collection time (usually one to two halflives of the nucleus being studied), the collection tape is advanced to one of the detector ports for counting. This entire system is kept at high vacuum ($\leq 10^{-6}$ torr) and is referred to as the "on-line" system.

The energy of the ORIC heavy-ion beam is chosen to maximize production of a given mass number. However, other neighboring masses are also produced in the target and passed to the separator which is capable of focusing eight to ten masses besides the primary mass [77].

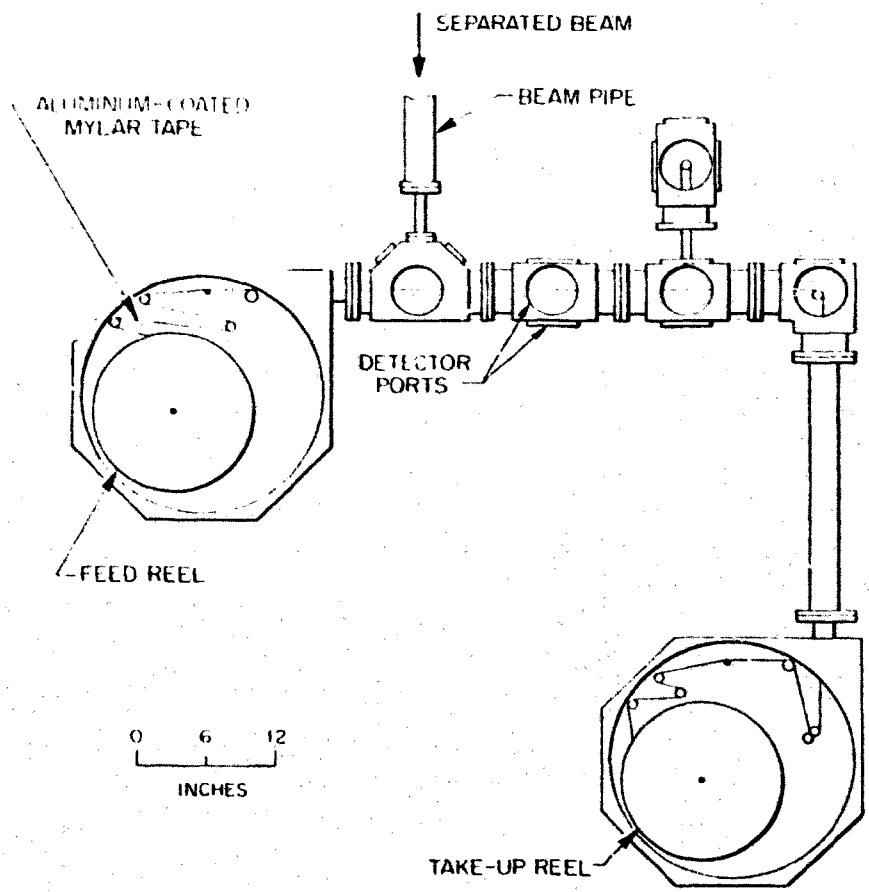

Figure 3-1. The Tape-Transport System on the Main (0°) Beam Line at UNISOR.

Therefore, two other beam lines have been installed 30° to either side of the main beam line, giving three on-line systems.

Techniques have also been developed to collect and remove still other masses from the separator, in order to use the cyclotron time more efficiently. These other masses are collected in the focal plane of the separator on aluminum coated Mylar tape, removed via a tape vacuum seal [78] and placed manually in front of detectors for counting. This experimental configuration is referred to as "off-line".

Three separate experiments were run, two off-line and one on-line on the 0° (main) beam line. All three were "parasite" runs in the sense that ^{185}Au was the primary nucleus being studied.

In the first run, γ-γ-t coincidence and γ-singles multiscaled data were taken off-line for 2.4 and 2.2 min ^{187m,g}Hg and 8.4 min ^{187}Au decays. In order to populate both the low- and high-spin states, the mass chain was entered at 18 sec ^{187}Tl by the reactions ^{180}W(^{14}N,7n)^{187}Tl and ^{182}W(^{14}N,9n)^{187}Tl. In the subsequent β^+, EC decays ^{187}Tl→^{187}Hg→^{187}Au→^{187}Pt, both high-spin and low-spin states, respectively, feed both high- and low-spin levels in the daughter nuclei.

The target consisted of 2.47 mg/cm^2 ^{182}W deposited on a 1.03 mg/cm^2 tantalum backing with a 1 mg/cm^2 tantalum cover, and behind this the ^{180}W was mounted directly on a graphite felt as described in ref. 76. This target was mounted in the modified UNISOR ion source [76] for the entire ^{187}Hg decay experiment and most of the ^{187}Au decay experiment. For the remainder of the ^{187}Au decay experiments, the UNISOR "high-temperature" ion source was used with only the ^{180}W-graphite felt target and Ta cover. These two ion sources are shown in Figs. 3-2 and 3-3.

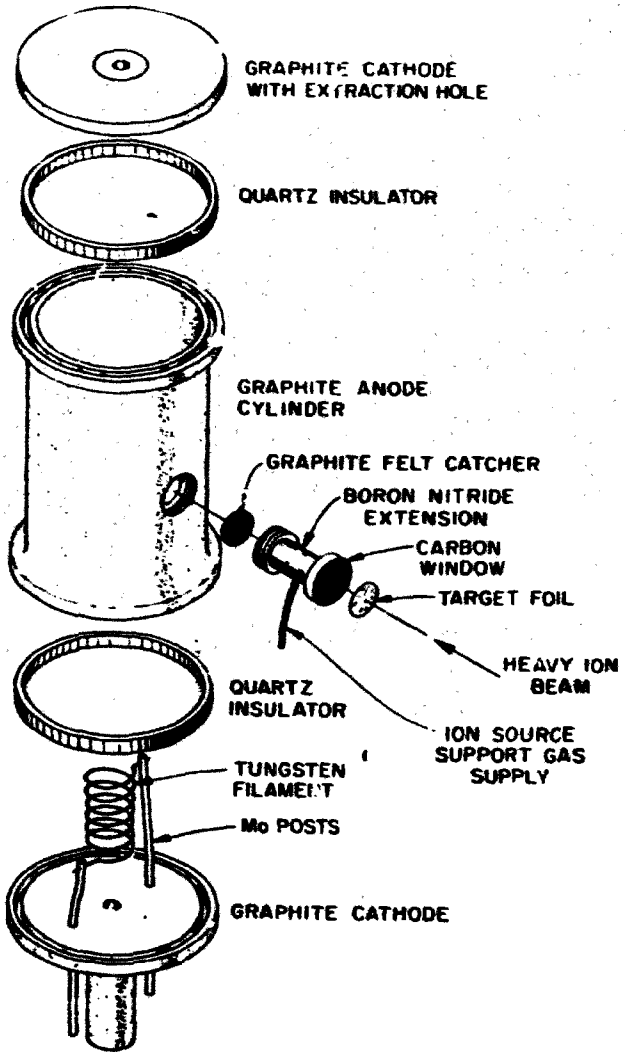

Figure 3-2. The Modified UNISOR Ion Source Using a Graphite Felt Catcher.

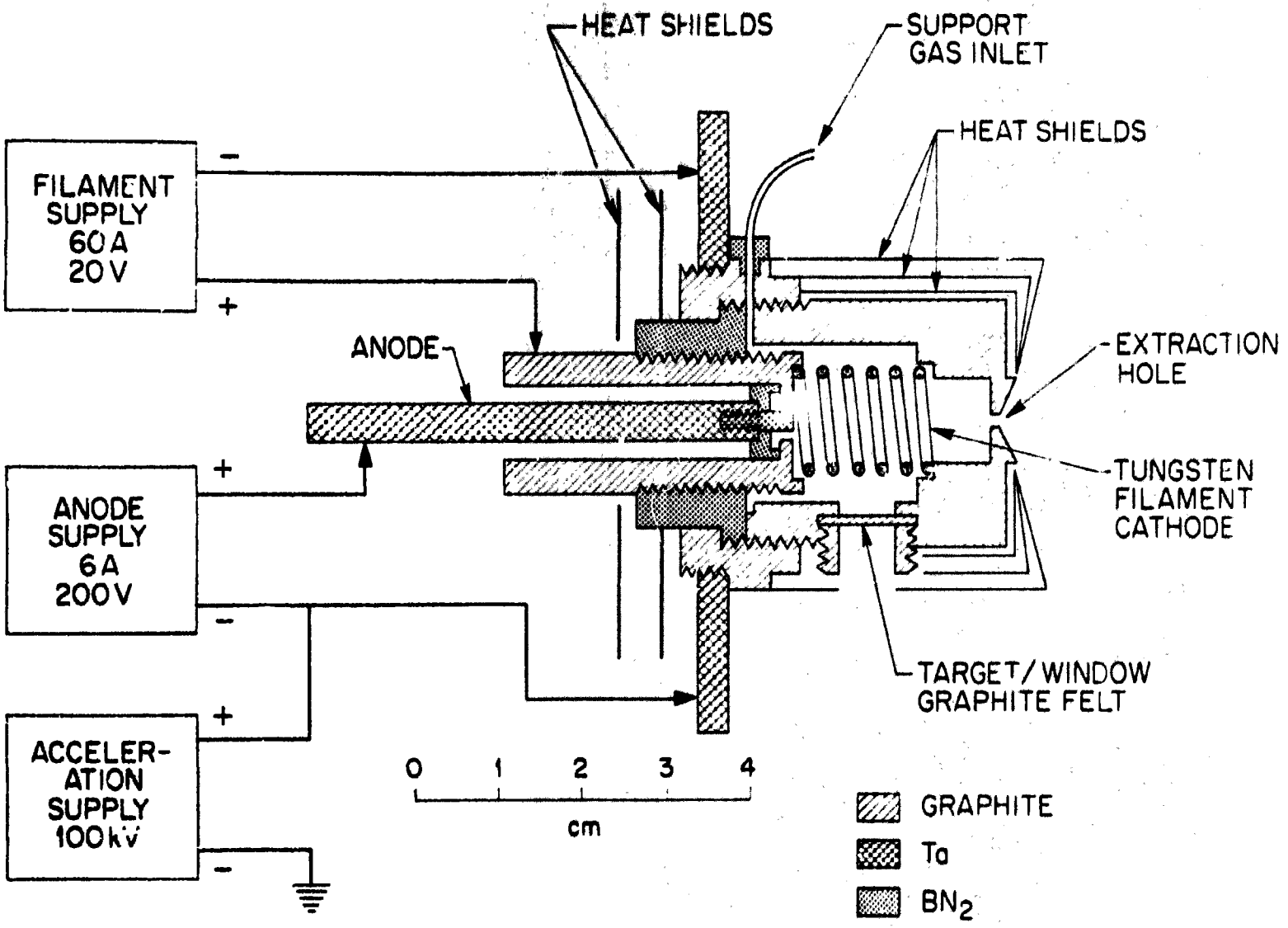

Figure 3-3. The UNISOR High-Temperature Ion Source.

The $^{14}N^{5+}$ cyclotron beam energy was 162.1 MeV.

In the second run, e-γ-t coincidence and electron singles multiscaled data were taken off-line for the decay of 8.4 min ^{187}Au. The mass chain was again entered at ^{187}Tl. The high-temperature ion source was used with ^{180}W as the target. The $^{14}N^{5+}$ cyclotron beam energy was 159.3 MeV.

In third run, e-γ-t coincidence and electron and gamma singles multiscaled data were taken on-line from the decay of 2.4 and 2.2 min ^{187}Hg isomers. In order to emphasize the population of high-spin states, ^{187}Hg was produced directly by the reaction ^{180}W (^{12}C,5n) ^{187}Hg. The target was ^{180}W with a 2 mg/cm^2 tantulum cover and graphite felt catcher mounted in the modified UNISOR ion source. The $^{12}C^{4+}$ cyclotron beam energy was 119.9 MeV.

Detectors

Large volume ORTEC Ge(Li) detectors were used for the gamma-ray measurements and KEVEX Si(Li) detectors for the conversion electron measurements. In the γ-γ-t experiments the Ge(Li) detectors used had efficiencies of 17% and 15%, respectively, measured relative to a 3"x3" NaI(Tl) detector at 1332 keV. The Ge(Li) detectors typically had resolution of 2.1 keV full-width at half-maximum (FWHM) at 1332 keV, a peak-to-Compton ratio of 40:1, and window-to-detector distance of 5 mm. The Ge(Li) detectors used in the ^{187}Au and ^{187}Hg e-γ-t experiments had efficiencies of 15% and 16%, respectively, with other characteristics similar to those of the 17% and 15% detectors discussed above.

The off-line electron detector had a 200 mm^2 surface area with a 3 mm depletion depth and FWHM of 2.4 keV for the 976 keV electron line

in the decay of ^{207}Bi. It was mounted in a vacuum chamber with a cup arrangement to allow a Ge(Li) detector to be positioned close to the source. The chamber was kept under vacuum by a cryosorption pump cooled in the same liquid nitrogen dewar as the detector cold finger. Access to the detector was provided by an airlock above the detector chamber. During the course of a run, a source was placed in this airlock in a source holder, the airlock pumped down to a pressure of less than 3×10^{-3} Torr, and the gate valve opened to allow positioning of the source in front of the detectors.

The airlock was originally pumped by a cryosorption pump, but this method was improved by connecting the airlock to the turbomolecular pump in the main beam line via a flexible metal tube. The cryosorption pump is used first to attain a vacuum of less than 10^{-1} Torr, so that the turbomolecular pump can be opened to the airlock with no appreciable pressure rise in the beam line. This was found to decrease the airlock pumpdown time by one to two minutes.

The on-line electron detector also was a KEVEX detector with 200 mm^2 surface area and 3 mm depletion depth. It gave better resolution (FWHM of 2.1 keV at 976 keV) than the off-line detector. The on-line detector was part of a system designed and built as a "mini-orange" spectrometer at the LSU Physics Department by Drs. A. Visvanathan and E. F. Zganjar to be used specifically on the UNISOR tape transport system. It consists of a bellows apparatus enclosing the detector, a liquid nitrogen cryostat, a cryosorption pumping system, an ion pump, a gate valve between the tape transport system and the bellows, and a "mini-orange" magnet (Fig. 3-4). The system was used in this work without

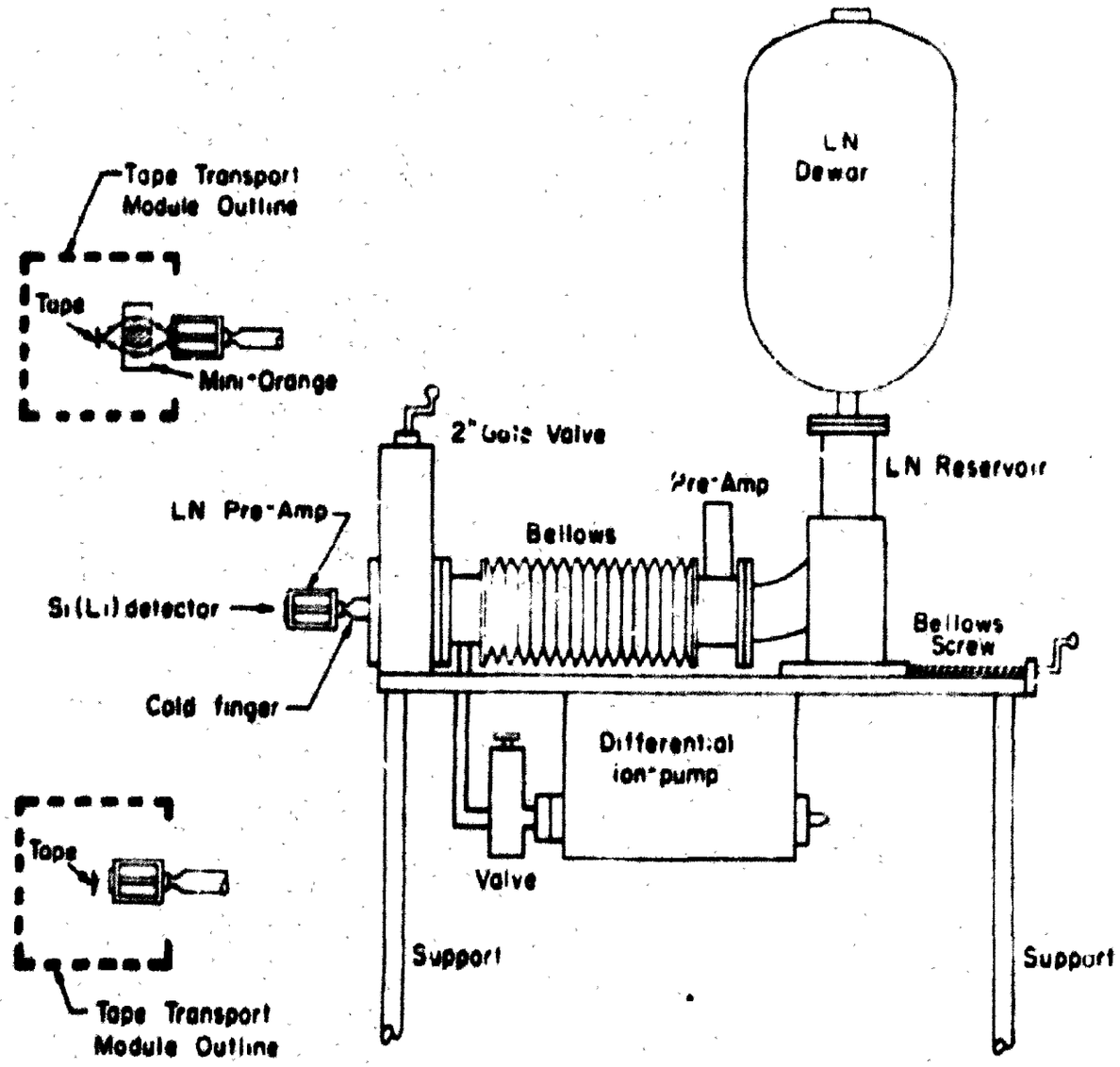

Figure 3-4. The LSU "Mini-Orange" Electron Detector System.

the magnet in order to increase the counting efficiency by allowing the detector to be positioned closer to the source than is possible when the magnet is in place. The advantage of this system is that it allows the tape transport to be brought to atmospheric pressure when necessary without having to warm the electron detector before exposure to air and later recool it.

Data Acquisition

Since detailed descriptions of the UNISOR data acquisition system are given in ref. 77, only a brief summary is given here. The three primary data acquisition systems at UNISOR are Tennecomp TP-5000 computers. These are essentially identical, differing only in the peripheral equipment used by each and as otherwise noted below.

The signals from the detectors are shaped and amplified using standard NIM module electronics (see Fig. 3-5). Two of the Tennecomp systems were interfaced via Tennelec PACE analog-to-digital converters (ADC units) which are capable of 8192 channel resolution. The third Tennecomp system, used only in the electron experiment for coincidence data from ^{187}Au decay, was interfaced via Nuclear Data ND-560 ADC units which are capable of only 4096 channel resolution.

The γ-γ-t data were taken off-line. The experiment was broken into two parts. The first part emphasized the ^{187m,g}Hg decay ($T_{1/2}$ = 2.4, 2.2 min) by collecting and counting sources for 150 sec. These sources were removed from the collection point in the separator via the tape-seal described above and mounted in a source holder between two detectors in 180^{0} coincidence geometry. The source holder is a 1.5 cm thick lead shield, lined with 1 mm thick Cd and 0.25 mm thick Cu on each

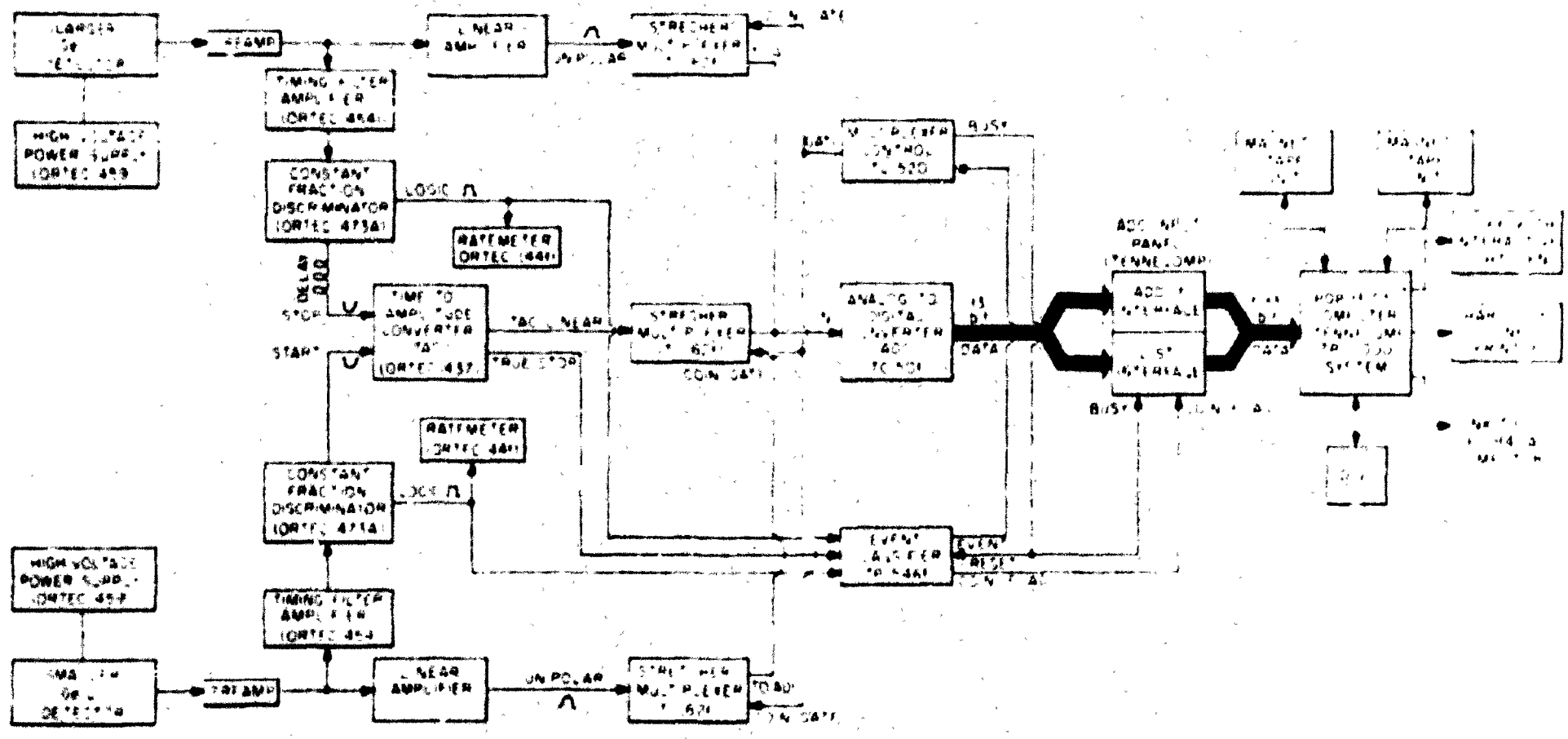

Figure 3-5. Block Diagram of Electronics Used in a Typical Coincidence/Singles UNISOR Experiment.

side, with a 2 cm diameter hole through the middle. The source holder was used to minimize Compton back-scattering and insure reproducible geometry. Sources were collected and counted for 150 sec with ten 8192 channel multiscaled planes, each of 14 sec duration with 1 sec between planes. Coincidence data were stored event-by-event on magnetic tape for later analysis. A software program on the Tennecomp system allowed simultaneous collection of coincidence data on magnetic tape and singles multiscaled spectra on disk. The multiscaled data allowed the determination of halflives of the different peaks in the spectrum and aided in assigning these peaks to the proper nucleus by following their decay or growth from plane to plane. As one source was counted, another fresh source was collected to replace it after the 150 sec counting time.

The second part of the γ-γ-t experiment emphasized the ^{187}Au decay ($T_{1/2}$ = 8.4 min) by collecting and counting sources for 1000 sec with ten 8192 channel multiscaled planes, each of 98 sec duration with 2 sec between planes. In both parts of the experiment the energy ranges were from about 40 keV to 2.5 MeV for one detector, and from about 40 keV to 3.5 MeV for the other detector, with the multiscaled data being taken from the former.

Coincidence data in both e-γ-t experiments were taken with a Tennecomp TP-5000 system. In the ^{187}Au decay experiment, however, the Tennecomp system was not interfaced to take simultaneous singles and coincidence data. Therefore, a Tracor Northern TN-1700 system was used for singles multiscaling of the electron data. Ten planes of 4096 channels and 100 sec counting time each were taken for each source. No γ-multiscaled data were collected during this run. The electron detector

energy range was from about 20 keV to 1900 keV, and that of the gamma detector was from about 40 keV to 1900 keV.

In the ^{187}Hg decay e-γ-t experiment, both electron and gamma multiscaled data were taken on a Tennecomp system. Ten 4096 channel planes of 15 sec counting time each were taken for γ-rays and electrons. Energy ranges were from about 40 keV to 1600 keV for gammas and from about 20 keV to 1600 keV for electrons.

In addition to the data taken during these runs, some UNISOR data taken on ^{187}Tl decay[79] were also analyzed for ^{187}Hg decay lines. These data consisted of e-γ-t coincidence, electron singles multiscaled and gamma singles multiscaled in 20 planes of 3 sec each. It was found from the singles spectra that the relative intensities of transitions between low-spin states in ^{187}Hg decay were higher in this experiment than in the ^{187}Hg decay experiments described above. Thus, these data were used further to establish coincidences with transitions between low-spin states and to look for other weaker coincidences between γ-rays connecting these states.

Calibrations

Energy and efficiency calibrations were performed before and after each run. In the γ-γ-t run, two standard sources were used: a National Bureau of Standards (NBS) mixed source (containing ^{109}Cd, ^{57}Co, ^{113}Sn, ^{139}Ce, ^{203}Hg, ^{85}Sr, ^{137}Cs, ^{60}Co, and ^{88}Y) and, since one detector had an energy range to 3.5 MeV, a ^{56}Co source was also used, which has γ-ray lines as high as 3.5 MeV. Efficiency calibrations were made for each detector using the NBS source and γ-ray intensities were computed relative to this.

In both e-.-t experiments, calibrations were performed with a mixed source of ^{133}Ba and ^{207}Bi. Known conversion coefficients[80,81] were used to obtain efficiency calibrations for the electron detectors, in order to calculate electron intensities. The gamma singles and electron singles intensities, corrected for efficiency, were then used to determine the internal conversion coefficients and hence the multipolarities.

A time-to-amplitude-converter (TAC) calibration also was done as part of each experiment by using a precision pulser to generate pulses 20 nanosec apart. This calibration was used in determining the nanosec lifetime of the 103.5 keV transition in ^{187}Au as described in the next chapter. The TAC resolution (FWHM) was about 10 nanosec.

Table 3-1. Summary of Experiments Performed

Run No.	Reaction(s) and Beam Energy	Type of Data Taken and Mode	Analyzer Used
1	^{180}W (^{14}N,7n) ^{187}Tl ^{182}W (^{14}N,9n) ^{187}Tl 162.1 MeV $^{14}N^{5+}$	(A) $^{187}Hg \rightarrow ^{187}Au$ off-line γ-γ-t γ multiscaled (B) $^{187}Au \rightarrow ^{187}Pt$ off-line γ-γ- γ multiscaled	Tennecomp TP-5000
2	^{180}W (^{14}N,7n) ^{187}Tl 159.3 MeV $^{14}N^{5+}$	$^{137}Au \rightarrow ^{187}Pt$ off-line e-γ-t e multiscaled	Tennecomp TP-5000 Tracor-Northern TN-1700
3	^{180}W (^{12}C,5n) ^{187}Hg 119.9 MeV $^{12}C^{4+}$	$^{187}Hg \rightarrow ^{187}Au$ e-γ-t e multiscaled γ multiscaled	Tennecomp TP-5000

CHAPTER IV

DATA ANALYSIS AND RESULTS

Aside from some preliminary analysis of the test data with the Georgia Tech CDC-Cyber-70 computer, all data analysis was done with the Tennecomp TP-5000 systems and SEL-840A computers at ORNL. Gated coincidence spectra were generated with the Tennecomp from the coincidence data stored on magnetic tape during each experiment. These gated spectra, the singles multiscaled spectra, and the calibration spectra were transmitted to the larger SEL-840A computers via an interface between the Tennecomp core and an SEL disk unit.

Once in the SEL, the spectra were analyzed with two in-house peak-fitting programs, LIZA[82] and PKFT[33]. Both peak-fitting programs compute least-squares fits to Gaussian shapes for up to five peaks at a time in a spectral region of up to 150 channels in length. Other available software allowed line-printer plots of the spectra to be made for later hand analysis.

The gated coincidence spectra were analyzed exclusively with LIZA, as it has options available for computing centroids and areas of peaks without performing a fit to the data. The areas in these cases were computed from the sum of the counts between two given channels and the centroids determined from a weighted average between these same channel limits. This feature is convenient in analyzing weak

coincidence peaks where statistics prevent a good fit, but a coincident line can be seen in the spectrum display.

The multiscaled data were analyzed primarily with PKFT. The summed multiscaled data of each experiment were used to determine accurate energy and relative intensity values for each peak (see Tables 4-1). For selected strong peaks, fits were made in each multiscaled plane and the resulting areas used for halflife measurements (see Fig. 4-1).

As part of the error analysis, the nonlinearity of the Tennecomp TP-5000 system was measured using the three-source method developed by Gehrke, Cline, and Heath[84]. The nonlinearity was found to be less than 0.4 channels between channels 400 and 7400 (corresponding to an energy range of 145 keV to 2360 keV for the detector from which energy values were determined) and between 0.4 and 1.0 channels above and below this range. In addition to the nonlinearity measurement, the error in the detector efficiency was established by performing efficiency calibrations with a National Bureau of Standards mixed source in three different positions, representing the uncertainty in positioning the samples in front of the detector during a run. These results are included in the errors quoted in Tables 4-1 and 4-4.

Data on ^{187}Hg decay and ^{187}Au decay were taken as described in the last chapter. A detailed description of the data analysis for ^{187}Hg decay is given below, and the ^{187}Au decay data are presented in an abbreviated form.

Table 4-1(a). Energies and Relative Intensities of Gamma Rays Placed in the Decay $^{197m,g}Hg$-^{197}Au.

Present Work		Bourgeois et al. [a]	
E_γ (keV) [b]	I_γ [b,c]	E_γ (keV) [b]	I_γ [c]
19.5*(3)		19.5	
51.0			
101.2 (4)	7.4 (6)	101.1 (2)	6.5
103.5 (4)[d]	26.7 (21)	103.4 (2)	32.4
137.9 (3)	10.3 (6)		
143.1 (3)	3.9 (3)	143.0 (2)	2.7
153.7 (2)	10.5 (7)	153.8 (2)	8.8
185.8 (2)[e]	3.2 (2)	185.8 (3)	2.2
203.4 (2)	25.0 (17)	203.4 (2)	18.9
205.4 (2)	12.9 (9)	205.5 (2)	10.4
214.9 (2)	<2		
220.8 (2)	20.9 (18)	220.8 (2)	24
221.0 (4)	<4		
233.4 (2)	100	233.4 (2)	100
235.9 (4)[e]	<5		
240.3 (2)	34.5 (26)	240.3 (2)	33.1
245.3 (3)	1.1 (7)		
252.0 (2)	17.9 (16)	252.7 (2)	8
255.2 (3)	8.0 (8)	255.2 (2)	8.9
257.7 (3)	5.0 (7)	257.0 (4)	3.4
258.8 (3)	2.2 (5)	258.8 (4)	1.8
265.9 (3)[e]	<2		
271.2 (4)	9.1 (6)		
271.6 (2)	28.0 (20)	271.5 (2)	30.8
272.2 (5)	5.5 (4)		
284.2 (2)	10.0 (8)	284.2 (2)	7
292.1 (3)	2.2 (3)		
298.2 (3)	7.5 (6)	298.5 (2)	10.6
298.7 (3)	7.8 (6)		
305.1 (2)	3.5 (10)	305.7 (3)	4
319.0 (2)	8.4 (6)	319.2 (2)	6.7
322.8 (2)	14.6 (10)	322.9 (2)	11.8
327.3 (4)	3.4 (4)		
332.1 (4)	<4		
332.2 (4)	<4		
334.6 (2)	19.7 (14)	334.7 (2)	16.4
336.4 (3)	3.5 (6)	336.5 (4)	2.4
342.3 (4)	<2		
349.2 (2)	10.6 (8)	349.4 (2)	5.8
354.8 (2)	1.8 (2)		

Table 4-1(a) (continued)

Present Work		Bourgeois et al. [a]	
E_γ (keV) [b]	I_γ [b,c]	E_γ (keV) [b]	I_γ [c]
363.4 (2)	3.1 (4)	363.6 (3)	2.9
372.9 (5)	<3		
374.9 (5)[e]	<5		
376.1 (2)	44.9 (30)	376.3 (2)	38.3
381.9 (2)	3.2 (4)		
385.4 (2)	2.8 (3)		
387.7 (2)	<4	388.1 (3)	2.5
389.0 (7)	<2		
391.5 (2)	6.4 (6)		
393.1 (2)	11.1 (9)	393.4 (2)	8.3
407.3 (2)	1.8 (2)		
410.7 (3)	5.7 (9)	410.3 (2)	4.6
426.1 (2)[e]	3.5 (2)		
429.4 (4)	3.8 (3)		
430.0 (3)	5.8 (4)	430.0 (2)	7.1
435.5 (2)	4.8 (9)		
438.7 (2)	11.6 (9)	438.7 (2)	11.3
446.5 (3)	<2		
446.9 (3)	<2	447.2 (2)	5.8
449.3 (2)	34.6 (22)	449.5 (2)	29.2
459.4 (3)	5.7 (5)	459.4 (4)	4.2
461.9 (2)	12.3 (9)	462.0 (2)	10.3
470.1 (2)	35.1 (22)	470.3 (2)	28.8
472.6 (2)	14.4 (10)	472.7 (2)	10.6
474.9 (5)	3.9 (3)		
475.7 (2)	14.2 (9)	475.8 (2)	22.3
476.1 (5)	9.3 (6)		
476.7 (2)	14.3 (9)	476.6 (2)	11.1
480.0 (2)	2.9 (8)		
484.2 (2)	6.1 (7)	484.4 (4)	2.6
486.6 (3)	2.9 (5)		
499.2 (2)	26.3 (17)	499.4 (2)	19.2
501.8 (2)	4.2 (4)	502.1 (3)	3.5
525.0 (5)	5.0 (3)		
525.2 (2)	29.2 (18)	525.4 (2)	30.1
525.4 (5)	3.6 (2)		
527.5 (3)	4.2 (8)		
536.8 (2)	4.2 (5)		
555.9 (4)	<2		
564.4 (2)	7.0 (8)	565.0 (2)	4.7
569.3 (4)	3.2 (6)		

Table 4-1(a) (continued)

Present Work		Bourgeois et al. [a]	
E_γ (keV) [b]	I_γ [b,c]	E_γ (keV) [b]	I_γ [c]
579.3 (3)	4.7 (9)		
582.5 (2)	7.6 (6)		
594.9 (3)	4.7 (3)		
602.5 (2)	3.3 (3)	602.7 (3)	2.1
616.2 (3)	3.3 (3)	616.3 (3)	1.9
619.4 (4)	2.1 (2)		
622.9 (5)	<2		
624.4 (4)	10.0 (6)		
624.8 (2)	9.0 (6)	625.0 (2)	14
629.5 (5)	1.8 (6)		
639.1 (2)	11.4 (9)	639.3 (2)	7.5
642.8 (3)	2.1 (6)		
646.3 (3)	2.4 (4)		
651.1 (3)	6.2 (6)	652.4 (4)	1.6
653.1 (3)	2.7 (4)		
657.3 (2)	10.8 (10)		
658.9 (5)	3.1 (4)		
659.6 (5)	3.1 (4)	659.2 (3)	3.5
669.2 (3)	3.2 (4)	669.0 (3)	4.3
669.8 (5)	2.5 (3)		
700.1 (3)	6.1 (6)		
709.7 (3)	9.8 (7)	709.6 (3)	6.4
745.8 (3)	2.6 (5)		
752.4 (3)	2.0 (3)		
760.8 (3)	2.1 (2)		
767.7 (2)	5.0 (4)	767.9 (2)	3.5
835.6 (4)	5.6 (6)	836.0 (3)	2.4
860.6 (3)	3.3 (3)		
873.0 (3)	3.2 (3)		
879.0 (5)	1.2 (3)		
895.3 (4)	4.2 (7)		
932.3 (3)	4.3 (5)		
1066.4 (2)	4.4 (3)		
1142.5 (4)	2.5 (5)		
1168.7 (6)	<2		
1179.5 (5)	5.4 (4)		
1236.1 (5)	2.9 (6)		
1283.7 (3)	3.6 (4)		
1314.7 (3)	6.0 (5)		
1350.1 (8)	2.0 (5)		
1357.7 (4)	6.2 (6)		
1363.3 (6)	2.8 (6)		

Table 4-1(a) (continued)

Present Work		Bourgeois et al. [a]	
E_γ (keV) [b]	I_γ [b,c]	E_γ (keV) [b]	I_γ [c]
1419.3 (5)	2.7 (8)		
1454.0 (9)	2		
1532.8 (3)	5.7 (8)		
1579.7 (3)	5.7 (5)	1579.7 (4)	3.8
1583.6 (3)	3.5 (4)		
1588.4 (3)	3.1 (5)		
1617.6 (5)	2.5 (5)		
1627.0 (3)	3.2 (3)		
1627.9 (3)	2		
1646.9 (3)	8.2 (6)	1647.3 (5)	4.7
1651.6 (3)	3.2 (4)		
1661.6 (3)	3.4 (5)		
1667.7 (4)	6.1 (11)		
1669.8 (5)	4.8 (11)		
1701.5 (3)	4.7 (5)		
1715.6 (6)	1.5 (4)		
1727.0 (3)	8.6 (7)		
1737.0 (5)	1.4 (5)		
1740.8 (3)	3.4 (3)		
1803.3 (7)	5.9 (19)	1803.8 (6)	3.3
1857.4 (3)	3.0 (4)		
1864.3 (5)	5.3 (5)		
1881.9 (4)	2.6 (3)		
1899.7 (3)	3.9 (6)		
1914.6 (3)	6.5 (8)		
1919.0 (6)	<2		
1952.0 (5)	<3		
1952.2 (5)	<2		
1997.0 (6)	1.3 (4)	1998.1 (8)	10.8
2014.0 (3)	14.2 (9)	2012.6 (8)	10.3
2047.4 (3)	1.6 (2)		
2076.7 (3)	18.6 (10)	2074.5 (9)	12.9
2103.1 (5)	2.2 (3)		
2155.4 (5)	1.4 (2)		
2180.1 (3)	30.5 (16)		

* Seen only in electron singles spectrum.

(a) ref. 30

(b) Errors are in parentheses and indicate uncertainties in the last significant figures reported.

Table 4-1(a). (continued)

(c) Intensities are relative to I (233.4) = 100.0. Intensities for multiplets unresolved in the singles data were obtained as described in the text.

(d) Intensity includes prompt and delayed component.

(e) Also in ^{187}Au-^{187}Pt decay.

Table 1-I(b). Energies and Relative Intensities of Gamma Rays Assigned to $^{187m,g}Hg$-^{187}Au Decay but not Placed in the Decay Scheme. Only lines with $I_\gamma \geq 3$ are included.

E_γ (keV) [a]	I_γ [a,b]	E_γ (keV) [a]	I_γ [a,b]
253.2 (2)	8.8 (8)	1023.7 (4)	3.3 (6)
277.1 (3)	3.3 (5)	1055.9 (3)	4.1 (6)
306.0 (3)	3.4 (6)	1094.4 (4)	4.0 (7)
326.4 (3)	3.4 (6)	1135.5 (3)	4.9 (6)
424.8 (2)	3.7 (5)	1196.6 (2)	6.1 (6)
437.1 (3)	3.1 (5)	1357.4 (3)	5.3 (6)
503.6 (3)	6.2 (7)	1365.5 (3)	4.6 (6)
515.8 (2)	4.5 (8)	1491.4 (3)	3.7 (5)
517.9 (3)	3.8 (8)	1502.8 (4)	3.3 (5)
571.2 (2)	8.6 (7)	1517.3 (3)	3.4 (5)
575.7 (3)	3.0 (6)	1549.9 (4)	3.1 (5)
581.2 (3)	3.5 (6)	1576.5 (3)	3.5 (5)
585.1 (3)	3.8 (6)	1729.8 (5)	3.5 (5)
661.0 (3)	3.1 (6)	1743.9 (5)	3.8 (6)
698.6 (3)	3.3 (7)	1958.3 (4)	3.4 (6)
723.6 (3)	3.2 (7)	1961.5 (5)	3.1 (6)
829.9 (3)	5.2 (6)	2030.0 (2)	13.9 (9)
848.2 (3)	4.0 (6)	2065.6 (5)	4.1 (6)
963.1 (2)	5.4 (6)	2081.9 (3)	9.1 (8)
982.9 (3)	3.0 (6)	2207.6 (3)	3.1 (3)
1000.9 (3)	3.6 (6)	2223.4 (2)	5.8 (4)

(a) Errors are in parentheses and indicate uncertainties in the last significant figures reported.

(b) Intensities are relative to I_γ (233.4) = 100.0.

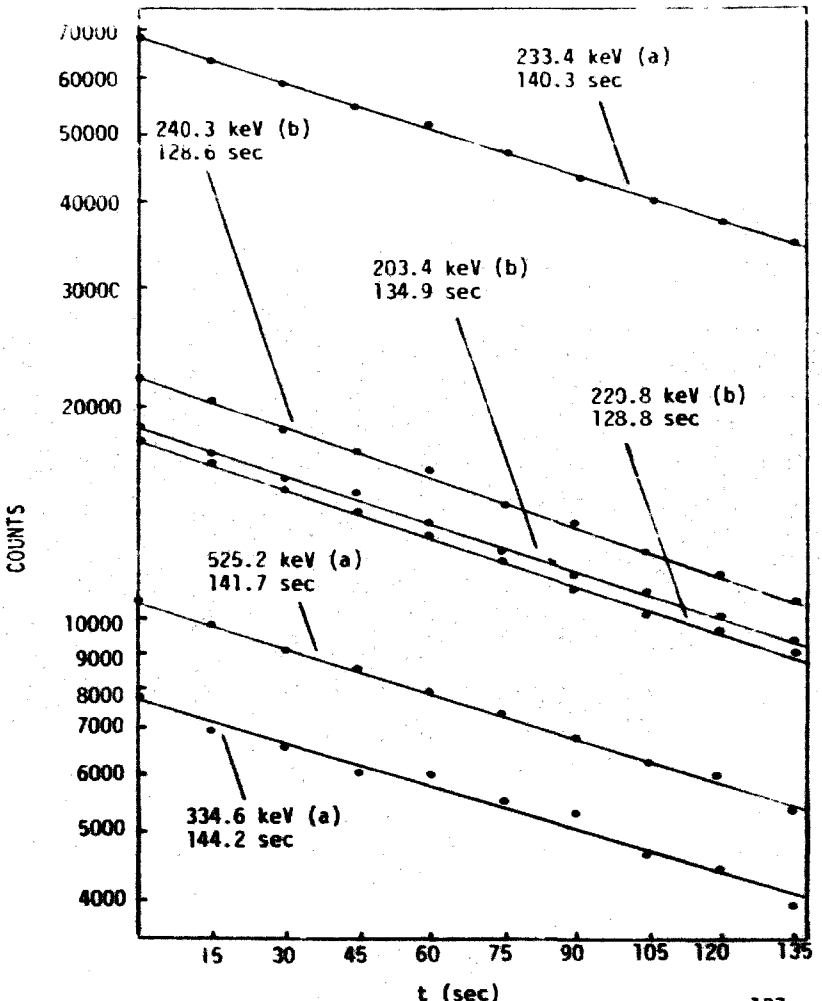

Figure 4-1. Decay Curves of Selected Transitions in the Decay $^{187m,g}Hg \rightarrow {}^{187}Au$. Transitions between high-spin states, denoted by (a), are populated in ^{187m}Hg decay and assigned $T_{1/2} = 2.4 \pm 0.1$ min and those between low-spin states, denoted by (b) are populated in ^{187g}Hg decay and assigned $T_{1/2} = 2.2 \pm 0.1$ min.

Decay of (2.4 min, 2.2 min) ^{187m,g}Hg (2.4 min) ^{187}Au

The summed multiscaled singles data (Figures 4-2) were analyzed as described above. This analysis yielded peak centroids and areas which were converted to energies and relative intensities with the calibrations taken during each experiment. Several of the peaks which appear to be singlets in the multiscaled data are actually unresolved multiplets. For these multiplets, energies and intensities were determined from coincidence gated spectra. For many of the less intense peaks, areas and centroids were determined by hand analysis of line-printer plots generated by the SEL-840A computer. The energies and relative intensities derived from these analyses are presented in Tables 4-1 along with the values reported in ref. 30.

Decay curves for selected lines in the gamma multiscaled data are presented in Fig. 4-1. Earlier work at CERN[15] reported two halflife components for the ^{187m,g}Hg decay: 2.4 ± 0.2 min and 1.6 ± 0.3 min. The two lines assigned $T_{1/2}$ = 1.6 min have energies 112 keV and 335 keV, respectively. The 335 keV line is assigned to ^{187}Hg decay in the present work but with $T_{1/2}$ = 2.4 min. The 112 keV line might be due to ^{186}Hg decay also reported in ref. 15. Since two states are decaying, a high-spin isomeric state and a low-spin ground state, two halflife components would be expected. However, it is found in the present work, and in ref. 30, that the difference in these halflife components is much smaller than the 0.8 min measured at CERN. In ref. 30, the metastable and ground states in ^{187}Hg are both assigned to $T_{1/2}$ = 2.2 min. The values measured in the present work, however, are $T_{1/2}$ = 2.4 ± 0.1 min for ^{187m}Hg and $T_{1/2}$ = 2.2 ± 0.1 min for ^{187g}Hg.

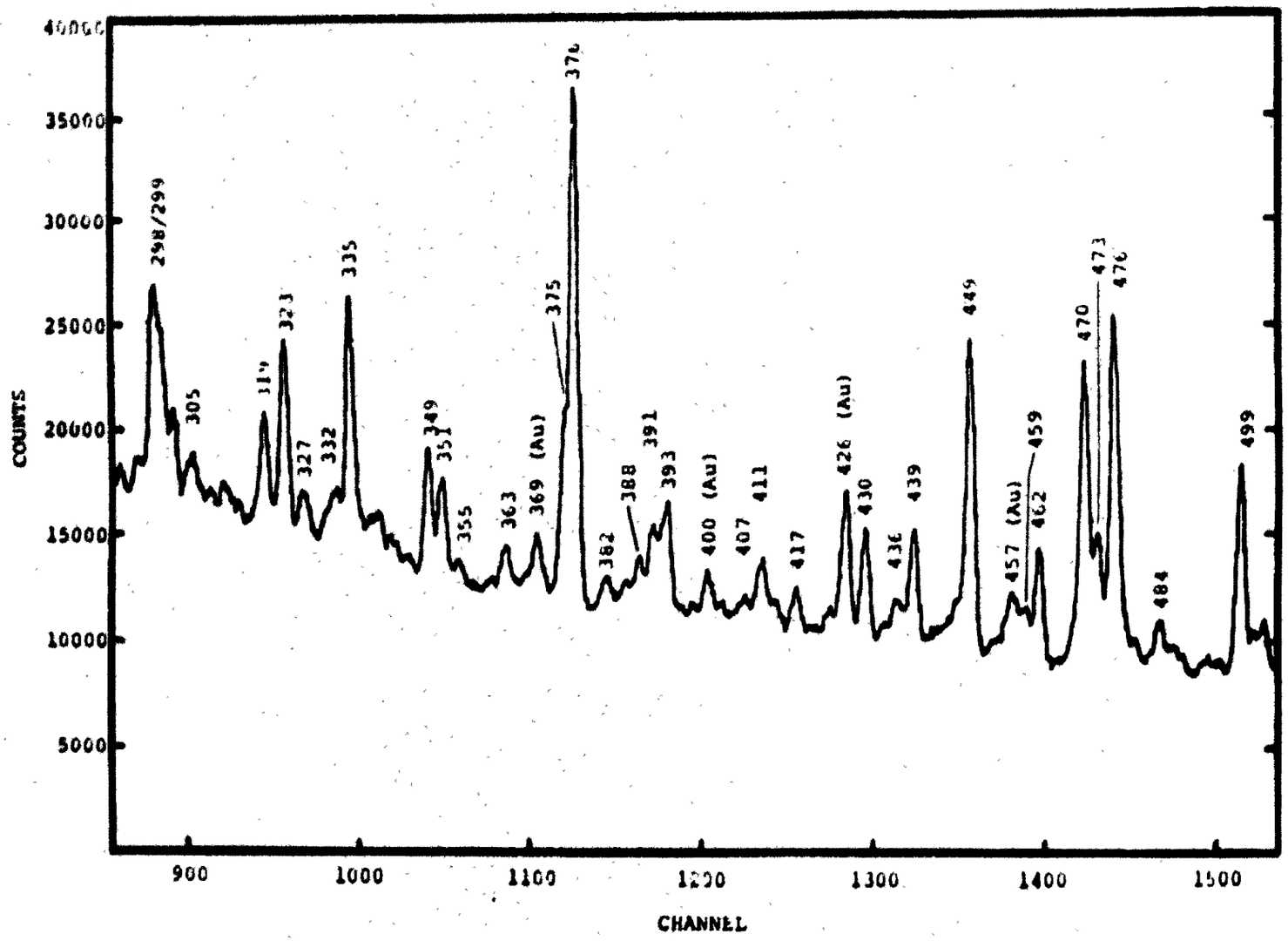

Figure 4-2 (a). Singles Gamma-Ray Spectrum of ^{187m,g}Hg Decay: Part I - Low-Energy Region from 298 keV to 501 keV.

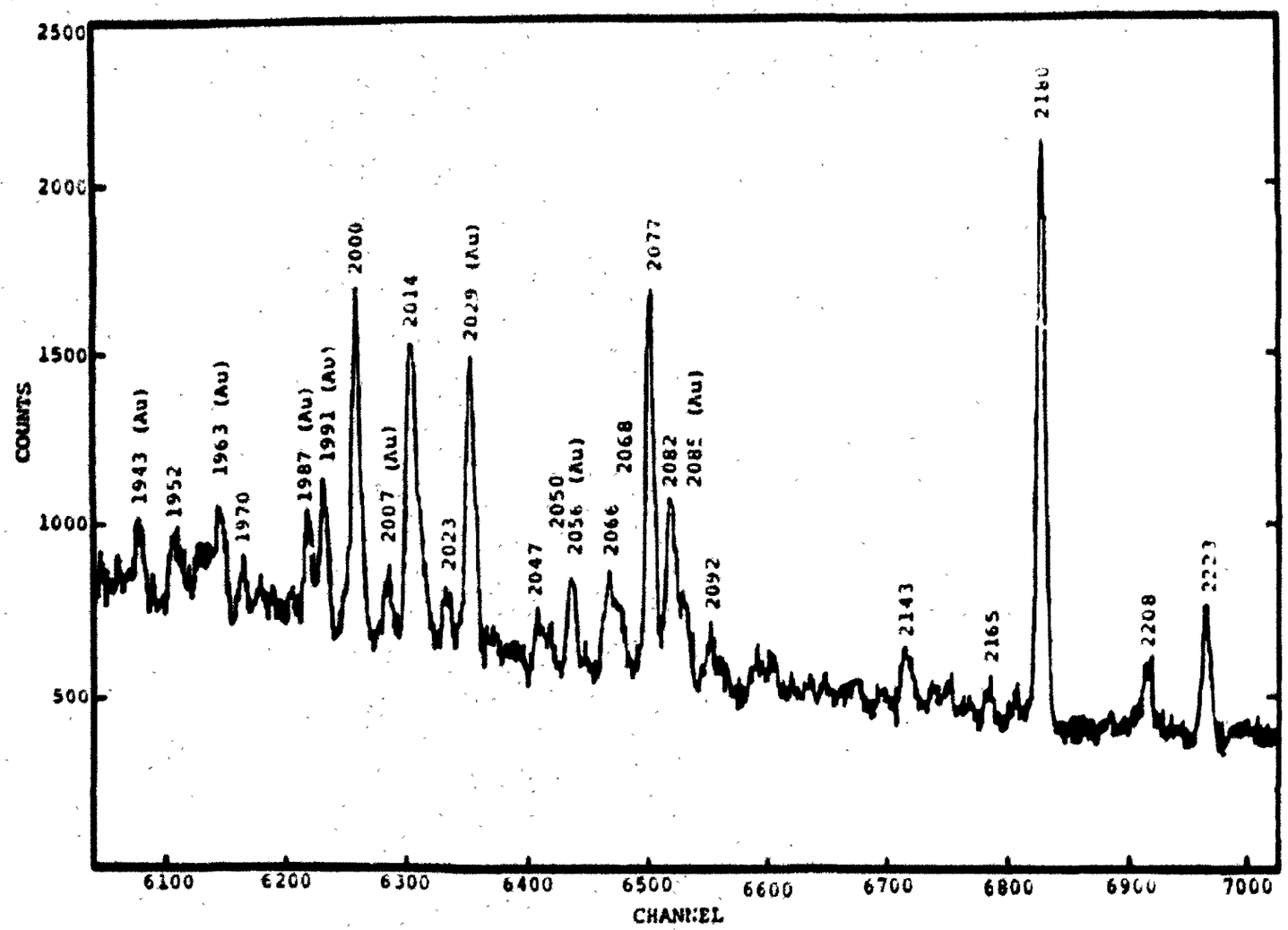

Figure 4-2 (b). Singles Gamma-Ray Spectrum of ^{187m,g}Hg Decay: Part II - High-Energy Region Near 2 MeV.

Gated coincidence spectra were generated from the coincidence data by setting energy "windows" on peaks recorded in the spectrum of one detector and a time window on the time-to-amplitude-converter (TAC) spectrum. Histograms were then constructed of the energy events in the second detector that occur within the two windows set. Typical coincidence spectra are shown in Figs. 4-3. A list of all assigned coincidence gates and their coincidences is given in Tables 4-2.

As mentioned above, several apparent singlets were actually multiplets unresolved in the singles data. To establish this, energy gate limits were moved across a suspected multiplet peak and the relative intensities of the concident lines in the gated spectrum were observed, e.g., as the upper channel limit on a gate was lowered, lines in coincidence with the high energy component of the multiplet would diminish relative to those in coincidence with the lower energy component of the multiplet. Energy and intensity values of these unresolved multiplet components were extracted from the coincidence data by looking in gates which "saw" the component in question in coincidence. Energies were then determined directly from the centroids in the coincidence spectra. Intensities were determined by comparison with other lines in the coincidence spectra whose intensities were known. Similarly, intensities of lines appearing both in the nucleus under study and in a neighboring nucleus were determined from coincidence spectra.

In general the TAC window was set to include only prompt events. The prompt TAC window corresponded to about 30 nanosec. The 103.5 keV transition, however, is known to depopulate an isomeric state with a lifetime of about 50 nanosec[26,30]. Thus, in addition to the prompt

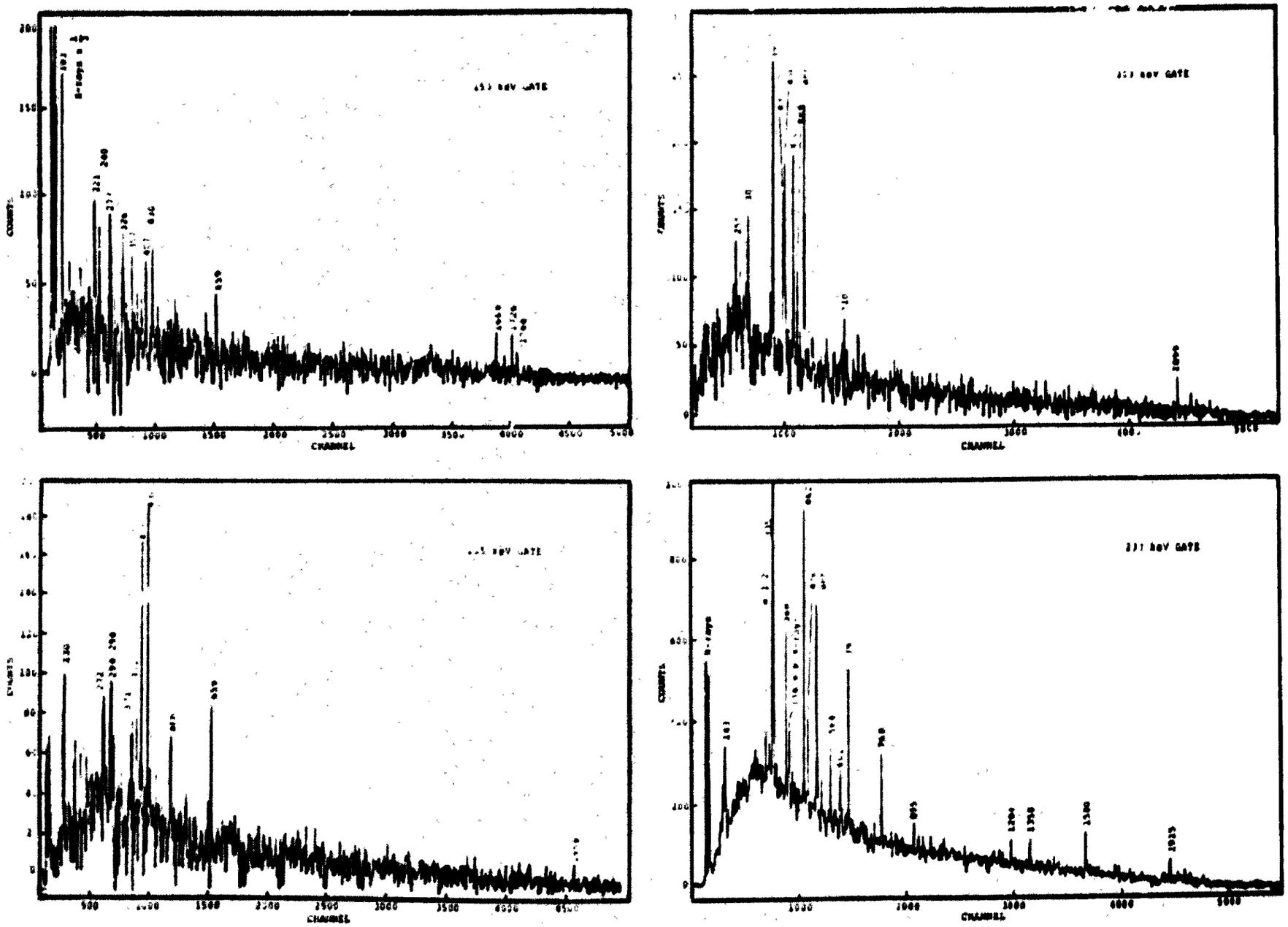

Figure 4-3 (a). Background- Subtracted Coincidence Gates for the 153, 203, 204, and 233 keV Lines in $^{187m,g}Hg$.

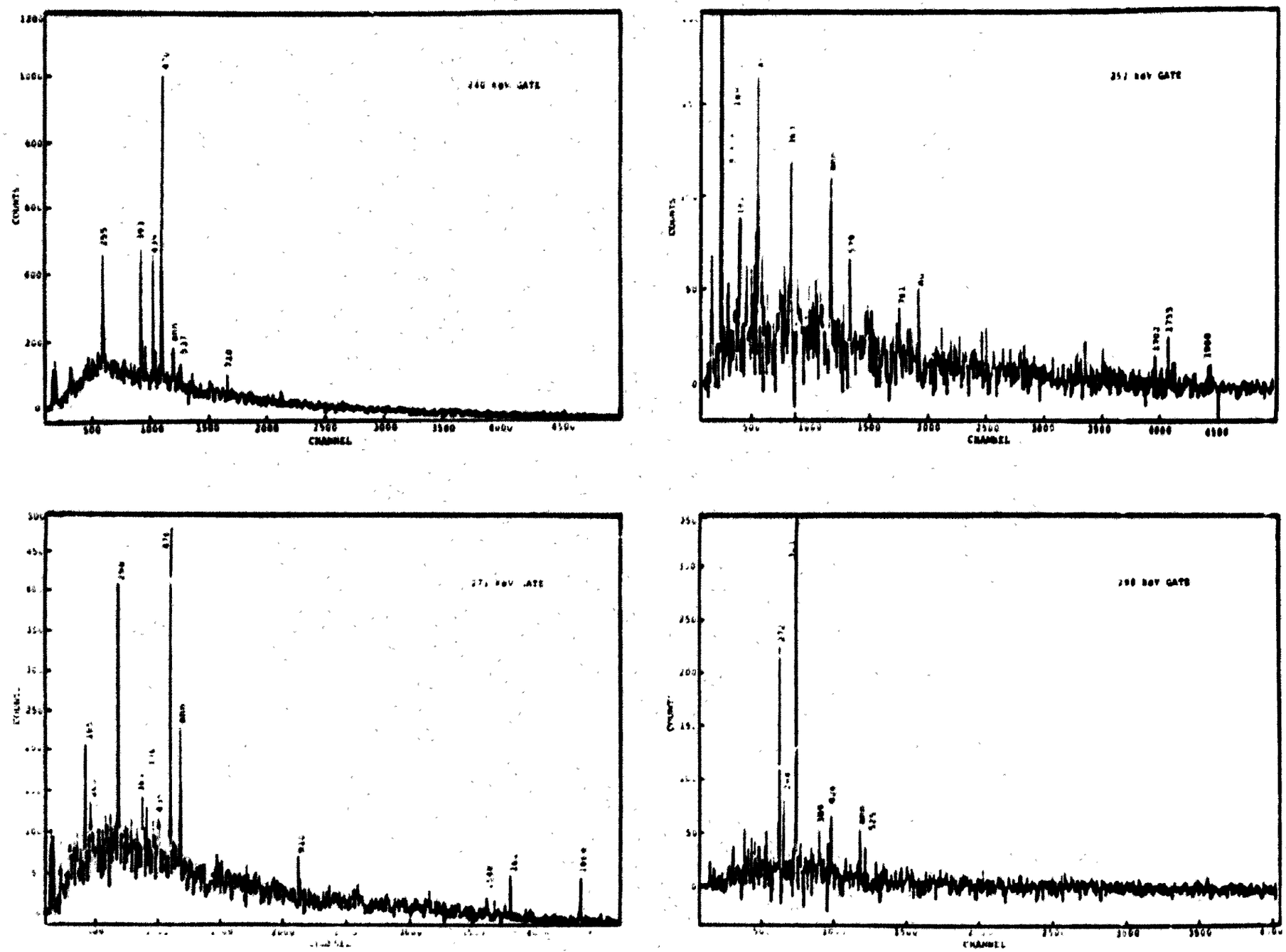

Figure 4-3 (b). Background- Subtracted Coincidence Gates for the 240, 252, 271, and 298 keV Lines in $^{187m,g}Hg$.

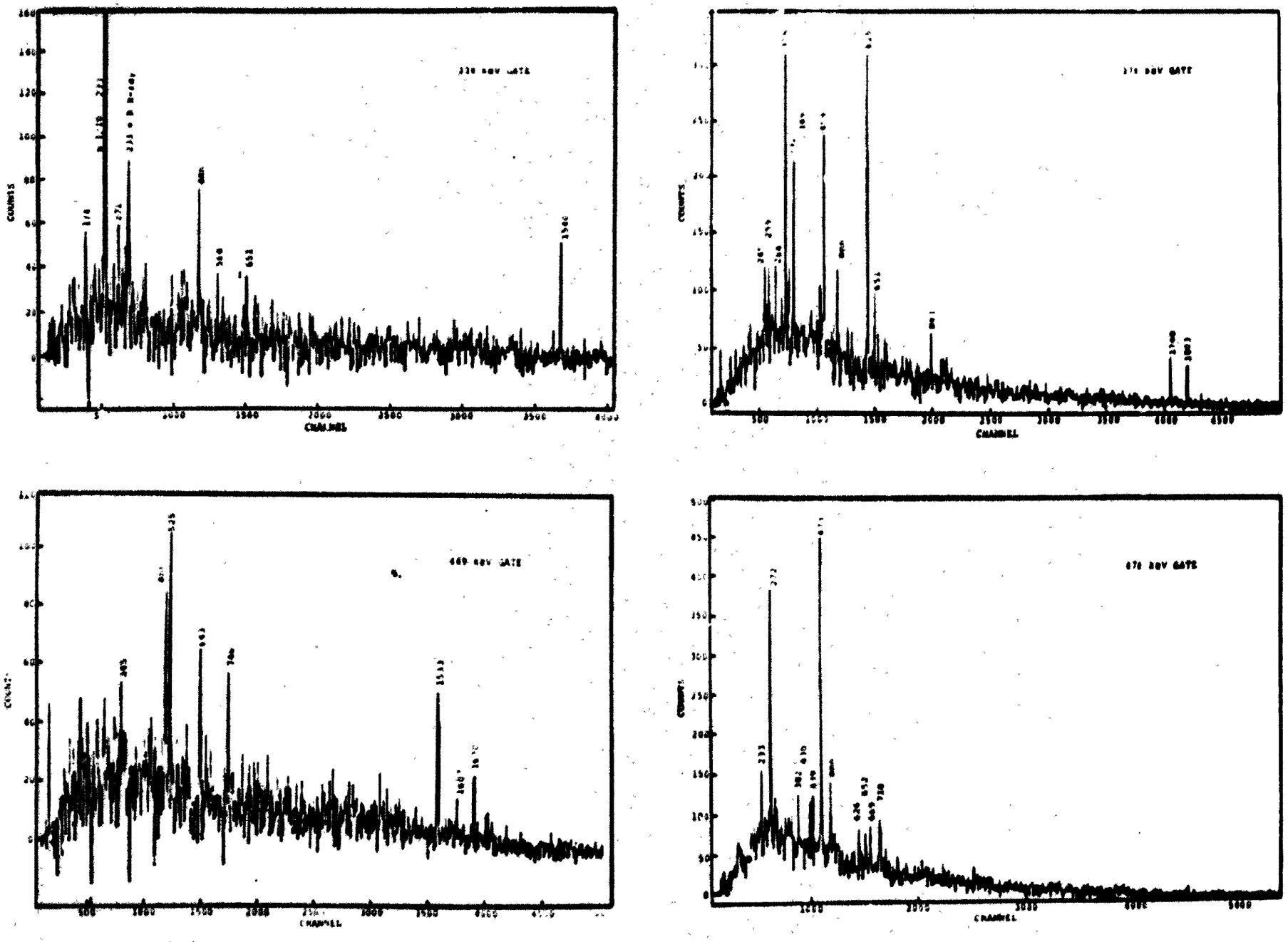

Figure 4-3 (c). Background- Subtracted Coincidence Gates for the 334, 376, 449, and 476 keV Lines in $^{187m,g}Hg$.

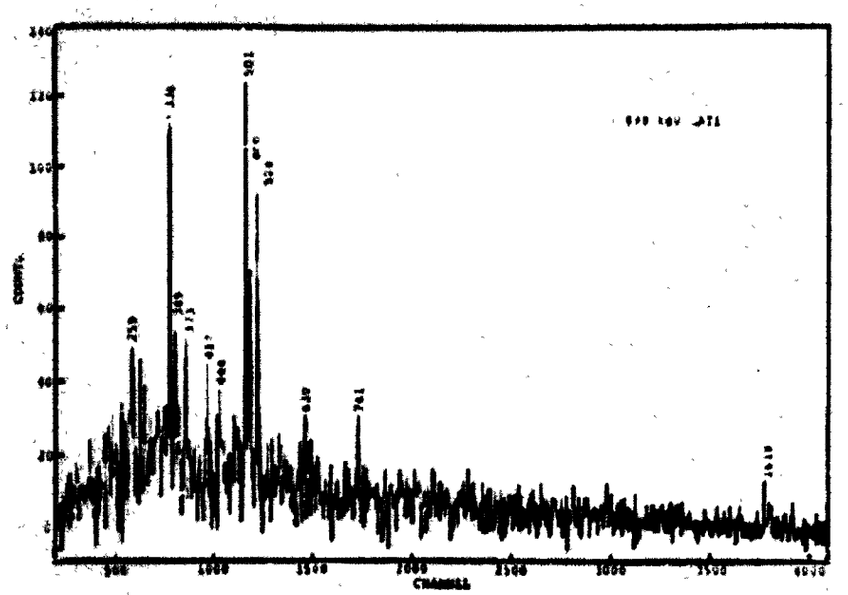

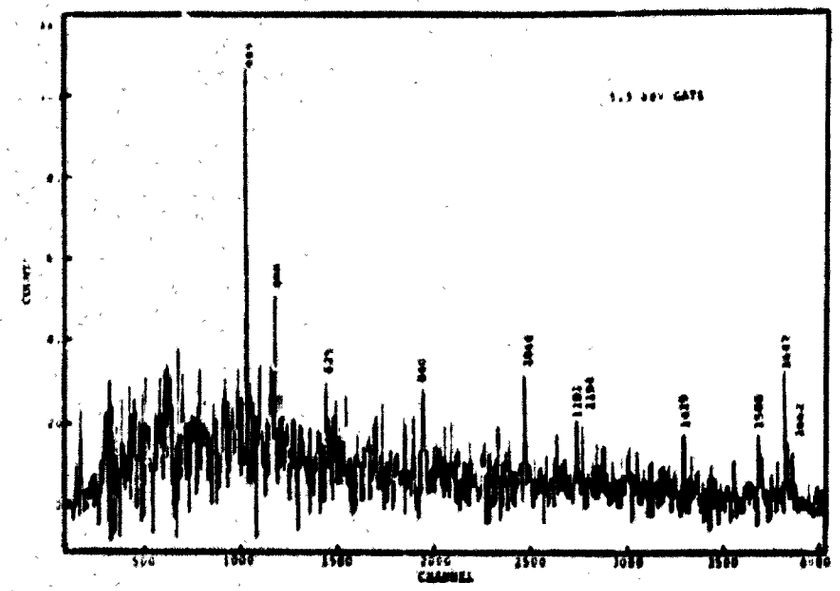

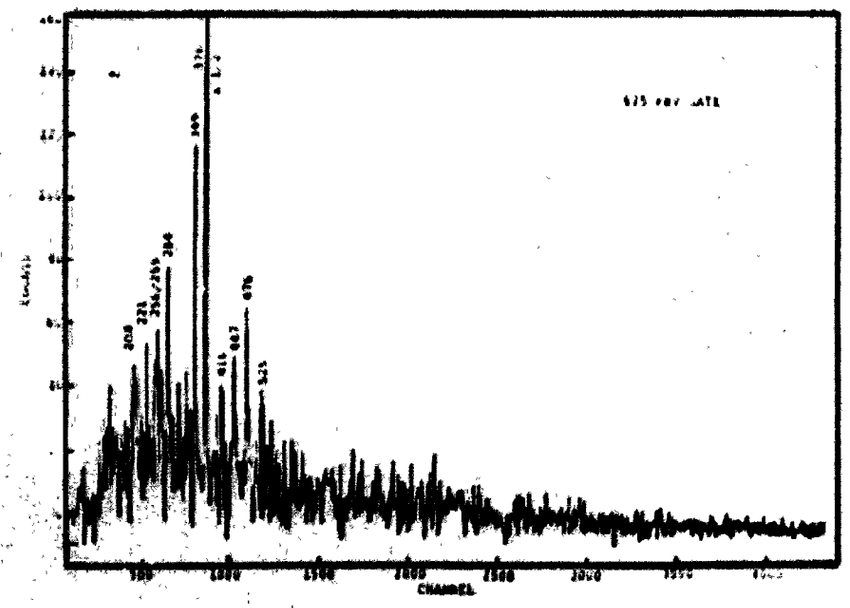

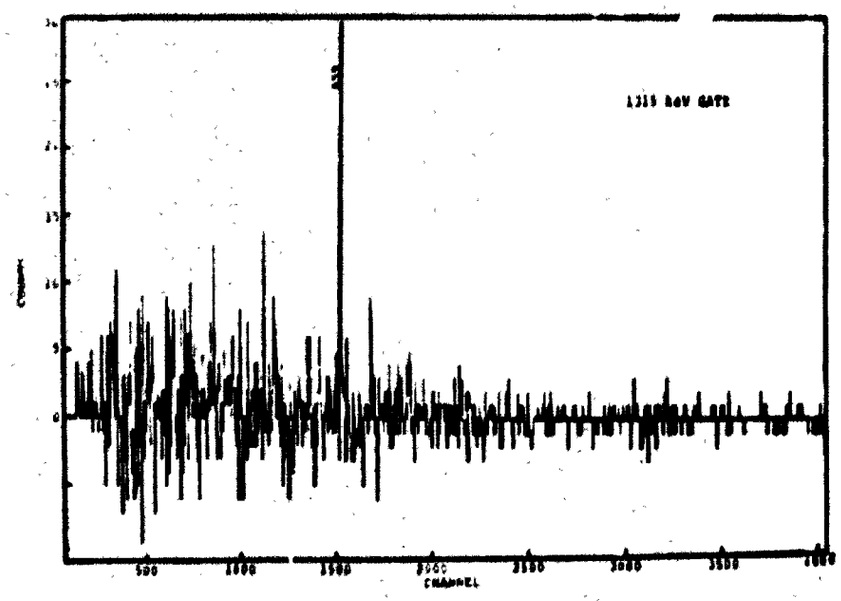

Figure 4-3 (d). Background- Subtracted Coincidence Gates for the 499, 525, 625, and 1315 keV Lines in $^{187m,g}Hg$.

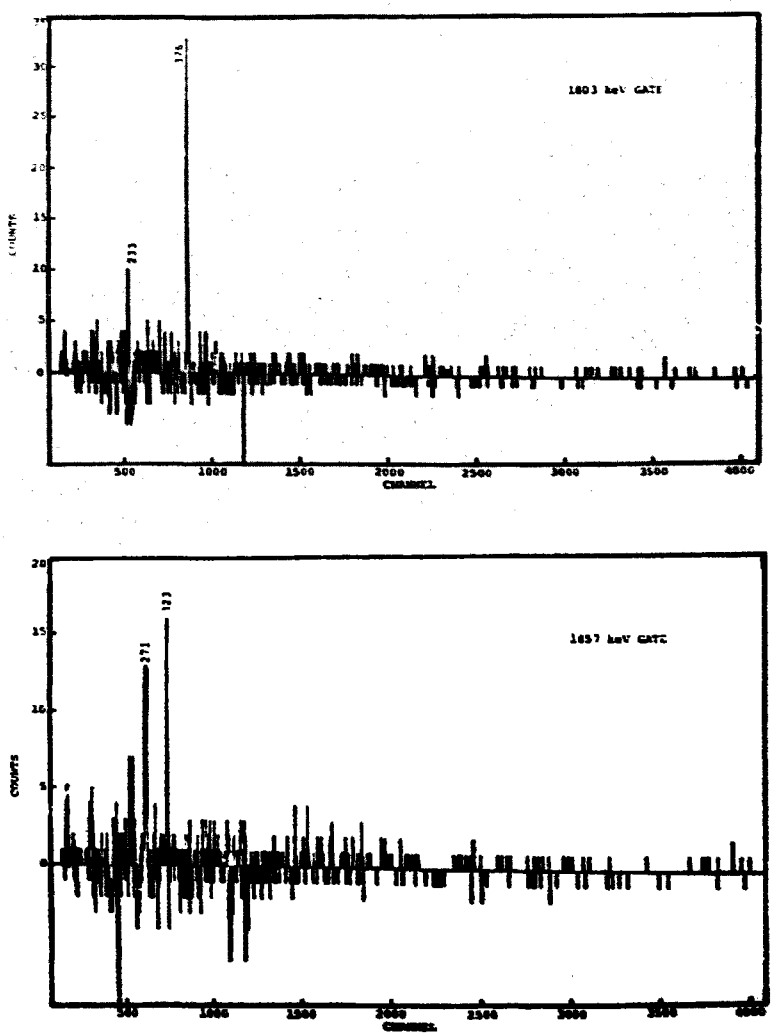

Figure 4-3 (e). Background-Subtracted Coincidence Gates for the 1803 and 1857 keV Lines in ^{187m,g}Hg Decay.

Table 4-2(a). Coincidence Relationships of Gamma Rays Placed in the $^{187m,g}Hg$-^{187}Au Decay Scheme.

Gate Energy (keV) [a]	Coincidences [b]
51.0 [c]	S: 153.7, 271.2 M: 103.5, 374.7 W: 181, 238, 299, 426.1
103.5 (prompt)	S: 154, 271.2 M: ann (d) W: 670
103.5 (delayed)	S: 252.0, 449.3, 525.4 M: 700.1 W: 622.9, 657, 674, 879.0, 931
143.1	S: 233.4 M: 240 W: 624.8
153.7	S: 103.5, 221.0 M: 240, 326, 392, 407.3, 429.4, 658.9 W: 357, 376, 1429, 1668, 1726, 1744
185.8 [e]	S: 271.6 M: 135, 326
203.5	S: 255, 391.5, 435.5, 470.1, 484.2, ann
205.4	S: 407.3, 430.0, 658.9 M: 130, 271.2, 294/298, 371, ann W: 170, 469, 602, 682, 798, 802, 849, 1315, 1360, 1581, 1958
214.9	W: 221, 476.1
220.8	S: 255.2, 393.1, 438.7, 470.1 M: ann
233.4	S: 143.1, 334.6, 387.9, 461.9, 474.9, 564.4, 639.1, 767.7 M: 602.5, 895.3, 1283.7, 1357.7, 1579.7, 1914.6 W: 1235, 1247, 1694, 1705, 1753, 1882, 1944, 1974, 2046, 2063, 2110, 2270, 2550, 2588, 2968

Table 4-2(a). (continued)

Gate Energy (keV) [a]	Coincidences [b]
235.9 [e]	S: 220.8, 240.3
240.3	S: 255.2, 393.1, 438.7, 470.1 M: 536.8 W: 709.7, 906/909, 1938
245.3	S: 568.5 M: 376.1
252.0	S:363.4 M: 181, 579.3, 760.8, 1702, 1755 W: 1728, 1766, 1777, 1908, 2144
255.2	S: 220.8, 240.3, 472.6 M: 327.3 W: 271, 669
257.7	S: 240.3, 470.1
258.8	S: 376.2, 624.8 M: 233.4 W: 501.4
265.9 [e]	M: 233.4
271.2	S: 298.7
271.6	S: 185.8, 395.8, 476.1 M: 342.3, 381.9, 1627.9, 1864.3
272.2	M: 103.5
271/272 (unassigned)	M: 154, 205, 265, 272, 419, 435 W: 1576, 1702, 1747, 1992
284.2	S: 298.7, 376.[illegible], 624.8 M: 203, 233.4, 390, 767.7 W: 165, 354, 470, 553, 1018, 1246, 1354
292.1	W: 203.4, 233, 376, 447, 47[illegible], 525
298.2	S: 284.2

Table 4-2(a) (continued)

Gate Energy (keV) [a]	Coincidences [b]
298.7	S: 271.8, 322.8 M: 426.1, ann
298 (unassigned)	W: 137, 170, 191, 200, 217, 233, 349, 418, 469, 525, 729, 1526, 1599
305.1	S: 233.4 M: 319.0, 334.6, 461.9, 470 W: 137, 165, 259, 364, 374, 525.0, 584, 593, 657, 740
319.0	S: 233.4, 376.2, 564.4 M: 178, 190, 585, 669, 932.3 W: 143.1, 236, 305.1, 393, 400, 416, 436/440, 525.0, 541, 805, 1234, 1499
322.8	S: 298.7, 385.4 M: 366, 426.1, 1857.4 W: 311, ann, 525
327.3	M: 153, 233, 240.3, 255.2, 436, 476.0 W: 220.8
332	M: 220.8, 240.3, 393.1
332.1	M: 233.4, 271, 323, 376.2
334.6	S: 233.4, 1579.7 M: 174, 271, ann, 564, 651, 677
336.4	M: 174, 499.2 W: 1085
342.3	M: 271.6, 381.9, 476.1 W: 166, 460, 517, 672, 758
349.2	S: 376.2, 624. M: 233.4, 237, 499.2, 501.4, 767.7 W: 220, ann, 848, 872, 1001, 1532
354.8	M: 220.8, 240.3, 277/282, 427, 450, 560 W: 301, 463, 635, 708

Table 4-2(a). (continued)

Gate Energy (keV) [a]	Coincidences [b]
363.4	S: 252.0 M: 135, 277, 389.0, 476.7, 745 W: 222, 449
372.9	M: 499.2
376.1	S: 245.3, 258.8, 284.2, 319.0, 332.2, 349.2, 454, 459.4, 624.8, 651.1 M: 446.3, 564.4, 860.6, 1740.1, 1803.3 W: 1175, 1283, 1526, 1713, 1883, 1929, 1945, 1952.2
381.9	M: 271.6, 342.2, 476.1 W: 123, 205, 298, 376, 392
385.4	M: 271.2, 322.8, 376 W: 160, 231, 292, 343, 350, 438, 470, 539, 665, 855, 1006
387.7	S: 233.4
389.0	M: 363.4, 426.1
388/389 (unassigned)	M: 437, 639 W: 550, 745, 757, 1249, 1490
391.5	M: 203.4 W: 272, 298, 330, 351, 488, ann, 538, 634, 705, 741, 822, 917
393.1	S: 220.8, 240.3 M: 133, 308, 332.2, 486.6, ann, 646.3 W: 284, 298, 382, 386, 437, 449, 565
407.3	S: 204.7 M: 153.7 W: 198, 222, 256, 275, 498, 544, 658, 669, 780, 808, 1032, 1066
410.7	S: 240.3, 470.1 M: 220.8, 836
426.1 [e]	M: 279, 298.7, 322.8

Table 4-2(a). (continued)

Gate Energy (keV) [a]	Coincidences [b]
429.4	S: 204.7 M: 153.7
430.0	S: 472.6 M: 255.2
429/430 (unassigned)	M: 302, 349, 370 W: 525, 552, 661, 669, 705, 915
435.5	M: 203.4
438.7	S: 220.8, 240.3, 470.1 M: 476.0
446.5	S: 376.2, 624.8
446.9	S: 220.8, 240.3
449.3	S: 525.4 M: 254, 285, 345, 440, ann, 642.8, 745.8, 1532.9, 1669.8 W: 213, 295, 318, 458, 498, 555.9, 590/593, 663, 683, 825, 860, 896, 1031, 1204, 1320, 1466, 1607
453.4	S: 376.2 M: 274 W: 1103, 1177, 1362
461.9	S: 233.4, 564.4 W: ann
470.1	S: 220.8, 240.3, 410.7, 438.7 M: 257.7, 309.0, 390, 475, 594.0 W: 455, 569
472.6	S: 220.8, 240.3, 255.2, 430.0, 476.0 M: ann
474.9	S: 233.4
475.7	S: 472.6 M: 430.0, 625.6, 709.7

Table 4-2(a). (continued)

Gate Energy (keV) [a]	Coincidences [b]
476.1	S: 271.6, 381.9
475/477 (unassigned)	M: 292, 341, 439, 669 W: 604, 652, 874, 1094
480.0	M: 277, 471, 525.2 W: 207, 226
484.2	M: 203.4, 240, 275, 349, 804, 908, 1181 W: 168, 220, 339, 648, 1652
486.6	M: 233, 393.1 W: 350, 438, 995, 1052
499.2	S: 336.4, 501.8, 527.5 M: 258.8, 349.2, 372.9, ann, 629.5 W: 1439, 1489, 1617.6, 1627.0, 1680
501.8	S: 499.2 M: 233.4 W: 284.2, 349.2
525.0	M: 305.1, 624.8 W: 501.4
525.2	M: 1066.4, 1646.9 W: 566, 669
525.4	S: 449.3 W: 1588.4
525 (unassigned)	M: ann, 840 W: 372, 1032, 1181, 1419
527.5	S: 499.2 M: 240, 452
536.8	M: 271.6, 476.1
538.9	M: 220.8, 240.3
564.4	S: 233.4, 319.0, 376.2, 461.9 ann

Table 4-2(a). (continued)

Gate Energy (keV) [a]	Coincidences [b]
579.3	S: ann M: 252.0 W: 185.8, 200, 333, 384, 640, 686
582.5	S: ann M: 220.8, 240.3 W: 200, 350, 383, 669
594.0	M: 470.1
602.5	S: 233.4
616.2	M: 389.0
619.4	M: 203.4, 284, ann
624.4	S: 476.0 M: 220.8, 255.2
624.8	S: 284.2, 349.2, 376.2 M: 446.9 W: 253.8, 525.0
624/625 (unassigned)	W: 144, 306, 416
629.5	W: 246, 271, 499.2
639.1	S: 233.4 M: ann
642.8	M: 271, 449.3 W: 300, 350, 473
646.3	M: 393.1 W: 203, 240.3, 300, 462, 474
651.1	S: 376.2 M: 233.4
653.1	S: 476.1 M: 271.6, 340

Table 4-2(a). (continued)

Gate Energy (keV) [a]	Coincidences [b]
657.3	M: 306, 1419.3 W: 233, 439, 538
658.9	S: 204.7, 1314.7 W: 153.7
659.6	M: 221.3, 272.2
669.2	S: 271.6, 476.1
669.8	W: 525.4
669/670 (unassigned)	M: 240 W: 220, 255
694.2	W: 564.4
700.1	M: 1179.5
709.7	S: 476.0 M: 220.8, 240.3, 255.2
745.8	M: 233, 240, 449,3 W: 272, 378. 410, ann
752.4	M: 376.2
760.8	M: 252.0 W: 335, 462, 753, 875
767.7	S: 233.4 M: 284.2, 349.2
860.6	M: 376.2
873.0	M: 233.4, 349.2, 624.8
895.3	M: 233.4 W: 380, 476, ann, 697, 932
1066.4	S: 525.2

Table 4-2(a). (continued)

Gate Energy (keV) [a]	Coincidences [b]
1142.5	M: 449.3 W: ann
1168.7	M: 221.0, 272.2 W: 182, 341
1179.5	S: 700.1
1236.1	M: 233.4 W: 376, 399, 476, ann
1283.7	S: 233.4 M: ann
1314.7	S: 658.9 M: ann
1350.1	M: 233.4
1357.7	S: 233.4
1363.3	M: 336.4, 499.2, 836 W: 459, 545
1419.3	M: ann, 657.3 W: 233, 525, 541, 724
1454.0	M: 233.4 W: 298
1532.8	S: 449.3 W: 350, ann
1579.7	S: 233.4, 334.6
1583.6	M: ann
1588.4	M: 525.4 W: 449.3
1617.6	W: 205, 233, 40.2
1627.0	W: 499.2

Table 4-2(a). (continued)

Gate Energy (keV) [a]	Coincidences [b]
1627.9	S: 271.6
1646.9	S: 525.2
1651.6	M: 525.2
1661.6	M: 525.4 W: 449.3
1669.8	M: 449.3 W: 270, ann
1701.5	W: 252.0
1715.6	W: 449.3
1727.0	W: 153.7, 233.4, ann
1737.0	W: 449.3
1740.8	S: 376.2 W: 233.4
1803.3	M: 376.2 W: 233.4
1857.4	W: 271.2, 322.8
1864.3	S: 271.6
1881.9	M: 233 W: 271.2, 298.7
1899.7	S: 203.4
1914.6	S: 233.4
1952.0	W: 203.4
1952.2	W: 233.4, 376.2
1997.0	M: 233.4

Table 4-2(a). (continued)

Gate Energy (keV) [a]	Coincidences [b]
2014.0	W: 240.3
2047.4	S: 233.4
2076.7	W: 203
2180.1	M: ann

(a) Energies for multiplets unresolved in the singles data are determined as described in the text. Each multiplet component and its coincidences are listed separately with unassigned coincidences of the multiplet listed after the last component.

(b) Coincidences are identified as S (strong, ~90% confidence in assignment), M (moderate, ~70% confidence in assignment), or W (weak, ~40% confidence in assignment). Exact energies are given for assigned coincidences, approximate energies for unassigned.

(c) Gate pulled in e-γ-t data.

(d) ann denotes annihilation line (511 keV).

(e) Also appears in ^{187}Au+^{187}Pt decay.

Table 4-2(b). Coincidence Relationships of Gamma Rays Assigned to the Decay $^{187m,g}Hg \rightarrow ^{187}Au$ but not Placed in the Decay Scheme. Only lines with $I_\gamma \geq 3$ are included.

Gate Energy (keV)	Coincidences [a]
277.1	M: 256, 284 W: 103, 153, 272, 298, 319, 355, 389, 469, 476, ann, 625, 647, 747, 1068
326.4	M: 153, 233, 257, 436 W: 250, 292
424.8	W: 154, 209, 299
503.6	M: ann W: 255, 275, 525, 1355
515.8	M: 284, 376, 507
517.9	M: 396 W: 476, 650
569.0	M: 181, 232, 332, 630 W: 471, 566, 587, 845, 1028
571.2	W: 220, 240, 288, 376, 424, 470, 476, ann
575.5	S: ann W: 237, 449, 706, 980
581.2	S: ann M: 220, 240 W: 200, 275, 334, 350, 383, 405, 474, 536, 637, 669
585.1	M: ann
723.6	W: 207, 245, 301, 337, 390. 469, 554, 599, 736
829.9	W: 210, 295, 331, 344, 541, 586, 1349
848.2	M: 233, 376 W: 438, 476, 717

Table 4-2(b) (continued)

Gate Energy (keV)	Coincidences [a]
963.1	W: 233, 476, 700
982.9	W: 286, 328, 451, 476
1000.9	W: 220, 287, 349
1023.7	M: 258, 426, 657, 760 W: 205, 210, 447, 477, 499/501
1055.9	M: 233 W: ann, 525
1094.4	M: 233, 448 W: 160, 220
1135.5	M: 476 W: 699
1365.5	M: 220 W: 347, 416, 476
1491.4	M: 237 W: 240, 384, ann
1502.8	W: 233, 319, 467
1517.3	W: 194, 204, 433
1549.9	W: 374
1576.5	W: 233, 271, 374
1743.9	M: ann W: 135, 153, 256
1958.3	W: 205, 223, 233
2030.0	W: ann
2065.6	no coinc.
2081.9	no coinc.

(a) Energies of coincident lines are accurate to ± 2 keV.

Table 4-2(b). (continued)

Gate Energy (keV)	Coincidences [a]
963.1	W: 233, 476, 700
982.9	W: 286, 328, 451, 476
1000.9	W: 220, 287, 349
1023.7	M: 258, 426, 657, 760 W: 205, 210, 447, 477, 499/501
1055.9	M: 233 W: ann, 525
1094.4	M: 233, 448 W: 160, 220
1135.5	M: 476 W: 699
1365.5	M: 220 W: 347, 416, 476
1491.4	M: 237 W: 240, 384, ann
1502.8	W: 233, 319, 467
1517.3	W: 194, 204, 433
1549.9	W: 374
1576.5	W: 233, 271, 374
1743.9	M: ann W: 135, 153, 256
1958.3	W: 205, 223, 233
2030.0	W: ann
2065.6	no coinc.
2081.9	no coinc.

(a) Energies of coincident lines are accurate to ± 2 keV.

gate, one was also set at this energy with a delayed TAC limit. These two gates are shown in Fig. 4-4, where the transitions feeding the isomeric state are seen to be more intense in the delayed gate.

The lifetime of this isomeric state was determined by setting a window on the appropriate energy range and creating a TAC spectrum from the coincidence data. The results are shown in Fig. 4-5, where the prompt component has been subtracted and a fit made to the decay curve. The lifetime obtained is 47.8 ± 4.6 nanosec in agreement with refs. 26, 30.

Similar analysis was carried out on the electron data. Electron gates (see Fig. 4-6) containing coincidences not already seen in the γ-γ-t data are included in Table 4-2. The electron singles data were used to determine internal conversion coefficients. Those lines for which conversion coefficients were deduced are listed in Table 4-3 with probable multipolarity and results of ref. 30 the multipolarities being assigned by comparison with theoretical values computed by Hager and Seltzer[85]. Systematic trends in the odd-mass gold nuclei were used to identify the 233.4 keV line as the transition between the 13/2- and 9/2- levels in the $h_{9/2}$ band (see Chapter V). Therefore, it was assigned a pure E2 multipolarity and used to normalize the electron and gamma efficiency calibrations.

The results of the data analysis are presented in Figs. 4-7 as energy level schemes with spins and parities given where known. Interpretations of these results are given in the next chapter. These schemes are based on coincidence relationships and energy sums and differences. Previous work[26,27,30] was used to help construct the

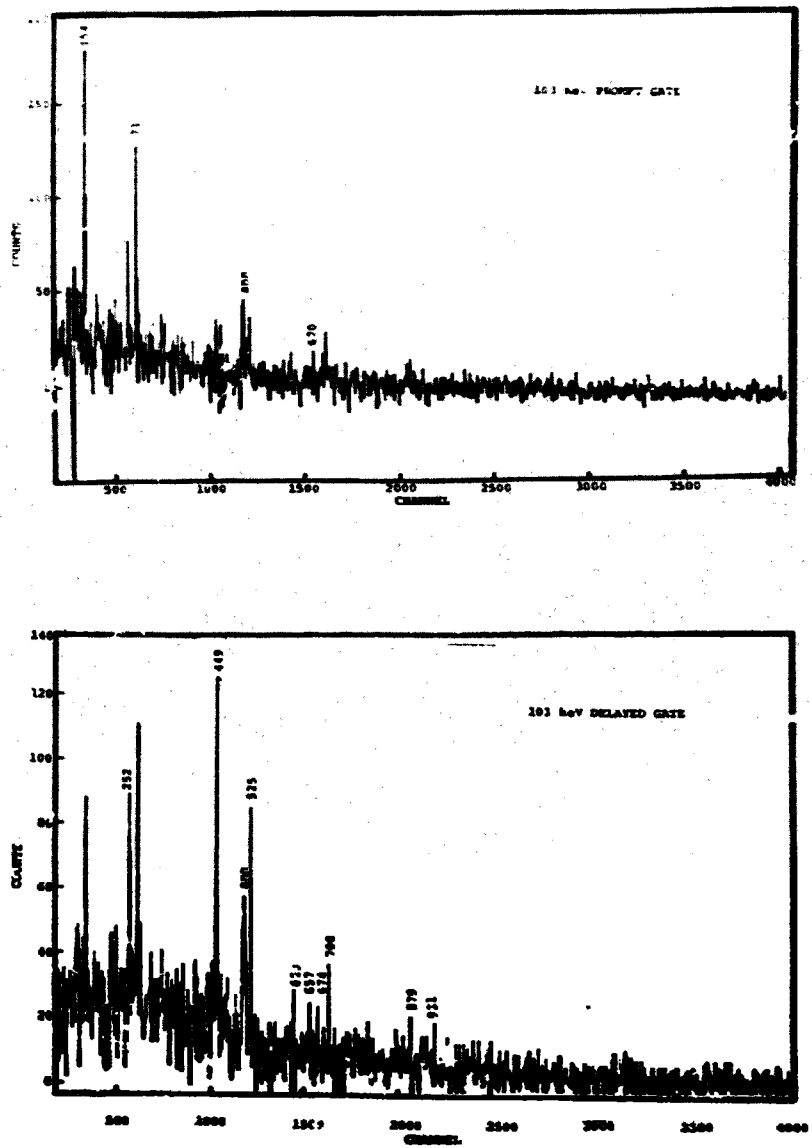

Figure 4-4. Background-Subtracted Coincidence Gates for the 103 keV Line in ^{187m,g}Hg Decay With Prompt and Delayed TAC Bounds.

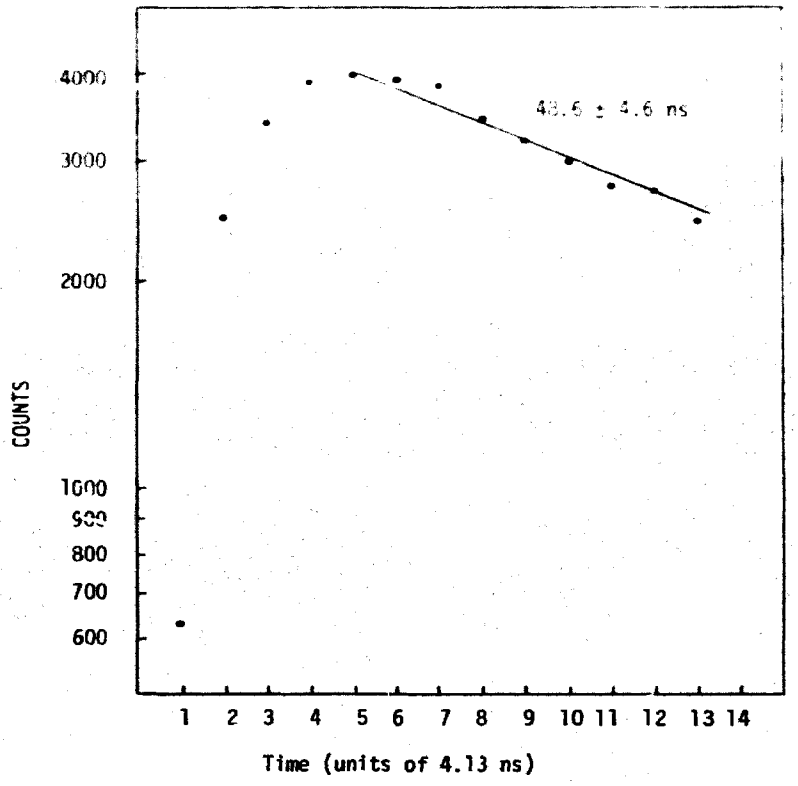

Figure 4-5. TAC Spectrum of the 103 keV Transition Between the $h_{11/2}$ and $h_{5/2}$ Bandheads. The transition is delayed due to shape isomerism, as discussed in Chapt. V.

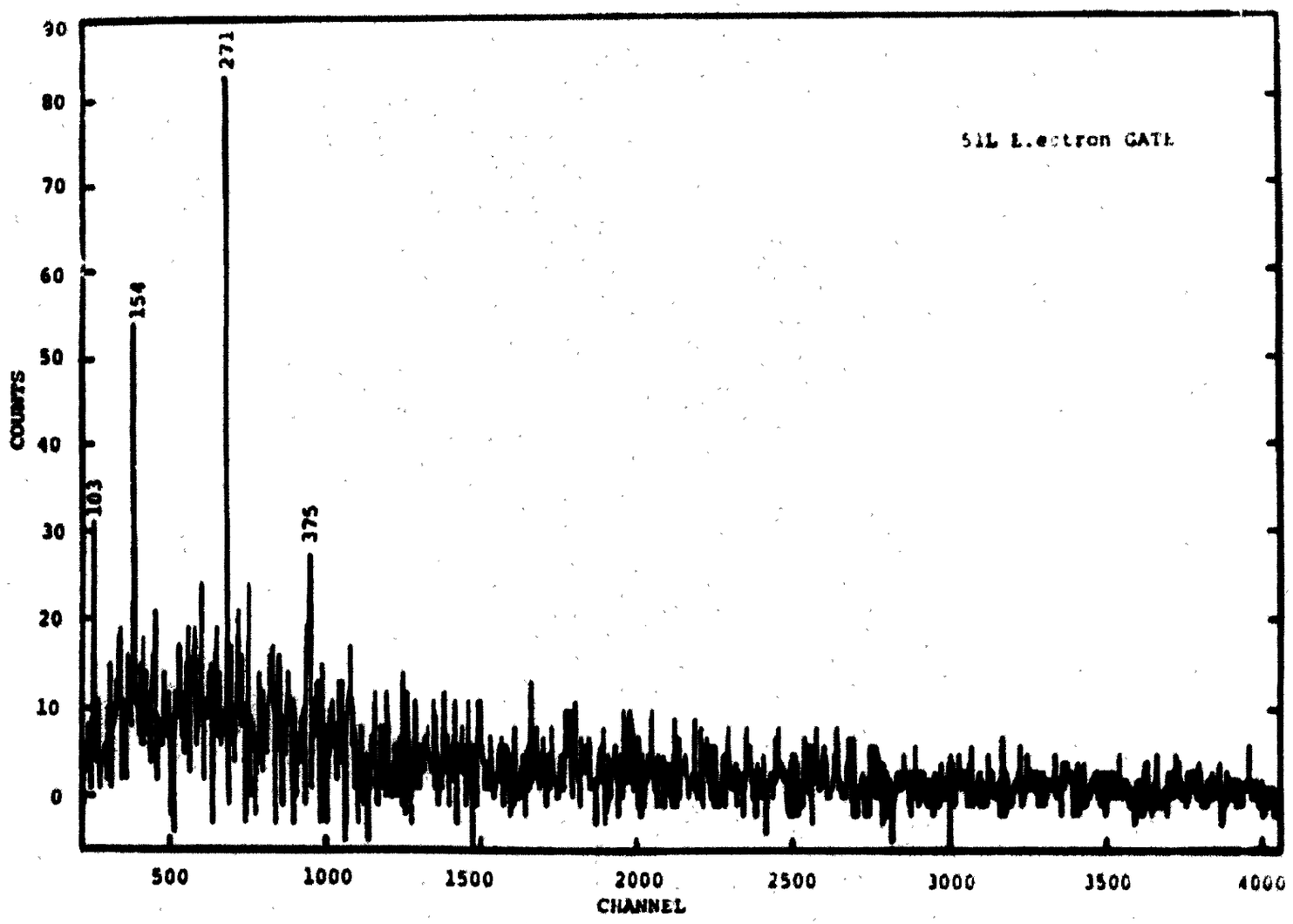

Figure 4-6. Background-Subtracted Coincidence Gate for the 51 keV L Electron Line in ^{187m,g}Hg Decay

Table 4-3. Internal Conversion Coefficients and Multipolarity Assignments for Lines in the Decay $^{187m,g}Hg \rightarrow {}^{187}Au$.

	Theoretical $\alpha_K \times 10^3$ a)			Present Work		Bourgeois et al. b)	
E_γ (keV)	E1	E2	M1	$\alpha_K \times 10^3$ c)	Multipolarity	$\alpha_K \times 10^3$ c)	Multipolarity
143.1	137	376	2225	5980 (1670)	M1	3000 (1000)	M1
153.7	115	321	1816	1702 (884)	M1 + E2	1000 (300)	M1 + E2
203.4	57	164	826	935 (178)	M1	650 (150)	M1 + (E2)
205.4	56	160	804	666 (131)	M1 + E2	700 (150)	M1 + (E2)
220.8*	46	134	658	344 (63)	M1 + E2	280 (60)	M1 + E2
233.4**	41	116	563	116**	E2	110 (30)	E2
240.3	38	108	520	158 (31)	E2	120 (30)	E2
252.0	33	96	456	223 (56)	M1 + E2	<300	(E2)
255.2	33	93	441	393 (106)	M1	380 (100)	M1
265.6	30	85	395	192 (173)	M1 + E2		
271.5	28	80	372	351 (56)	M1 + E2	300 (60)	M1 + E2
284.2	25	71	329	478 (76)	M1		
298.5*	22	63	288			23 (6)	E1
319.0	19	54	240	94 (33)	E2	70	E2
322.8	19	52	233	439 (79)	M1 + E2 +E0		
334.6	17	48	211	47 (7)	E2	42 (12)	E2
349.2	16	43	188	250 (60)	M1	220 (50)	M1

Table 4-2(b). (continued)

Gate Energy (keV)	Coincidences [a]
963.1	W: 233, 476, 700
982.9	W: 286, 328, 451, 476
1000.9	W: 220, 287, 349
1023.7	M: 258, 426, 657, 760 W: 205, 210, 447, 477, 499/501
1055.9	M: 233 W: ann, 525
1094.4	M: 233, 448 W: 160, 220
1135.5	M: 476 W: 699
1365.5	M: 220 W: 347, 416, 476
1491.4	M: 237 W: 240, 384, ann
1502.8	W: 233, 319, 467
1517.3	W: 194, 204, 433
1549.9	W: 374
1576.5	W: 233, 271, 374
1743.9	M: ann W: 135, 153, 256
1958.3	W: 205, 223, 233
2030.0	W: ann
2065.6	no coinc.
2081.9	no coinc.

(a) Energies of coincident lines are accurate to ± 2 keV.

gate, one was also set at this energy with a delayed TAC limit. These two gates are shown in Fig. 4-4, where the transitions feeding the isomeric state are seen to be more intense in the delayed gate.

The lifetime of this isomeric state was determined by setting a window on the appropriate energy range and creating a TAC spectrum from the coincidence data. The results are shown in Fig. 4-5, where the prompt component has been subtracted and a fit made to the decay curve. The lifetime obtained is 47.8 ± 4.6 nanosec in agreement with refs. 26, 30.

Similar analysis was carried out on the electron data. Electron gates (see Fig. 4-6) containing coincidences not already seen in the γ-γ-t data are included in Table 4-2. The electron singles data were used to determine internal conversion coefficients. Those lines for which conversion coefficients were deduced are listed in Table 4-3 with probable multipolarity and results of ref. 30, the multipolarities being assigned by comparison with theoretical values computed by Hager and Seltzer[85]. Systematic trends in the odd-mass gold nuclei were used to identify the 233.4 keV line as the transition between the 13/2- and 9/2- levels in the $h_{9/2}$ band (see Chapter V). Therefore, it was assigned a pure E2 multipolarity and used to normalize the electron and gamma efficiency calibrations.

The results of the data analysis are presented in Figs. 4-7 as energy level schemes with spins and parities given where known. Interpretations of these results are given in the next chapter. These schemes are based on coincidence relationships and energy sums and differences. Previous work[26,27,30] was used to help construct the

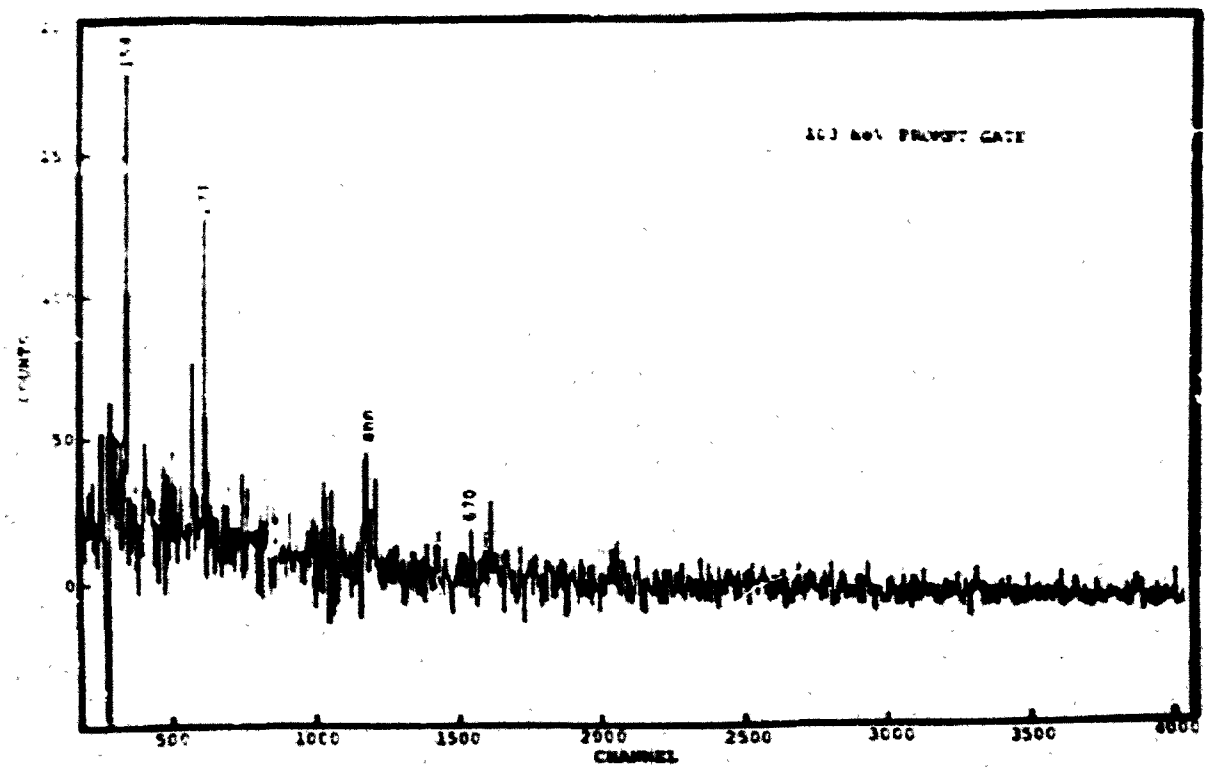

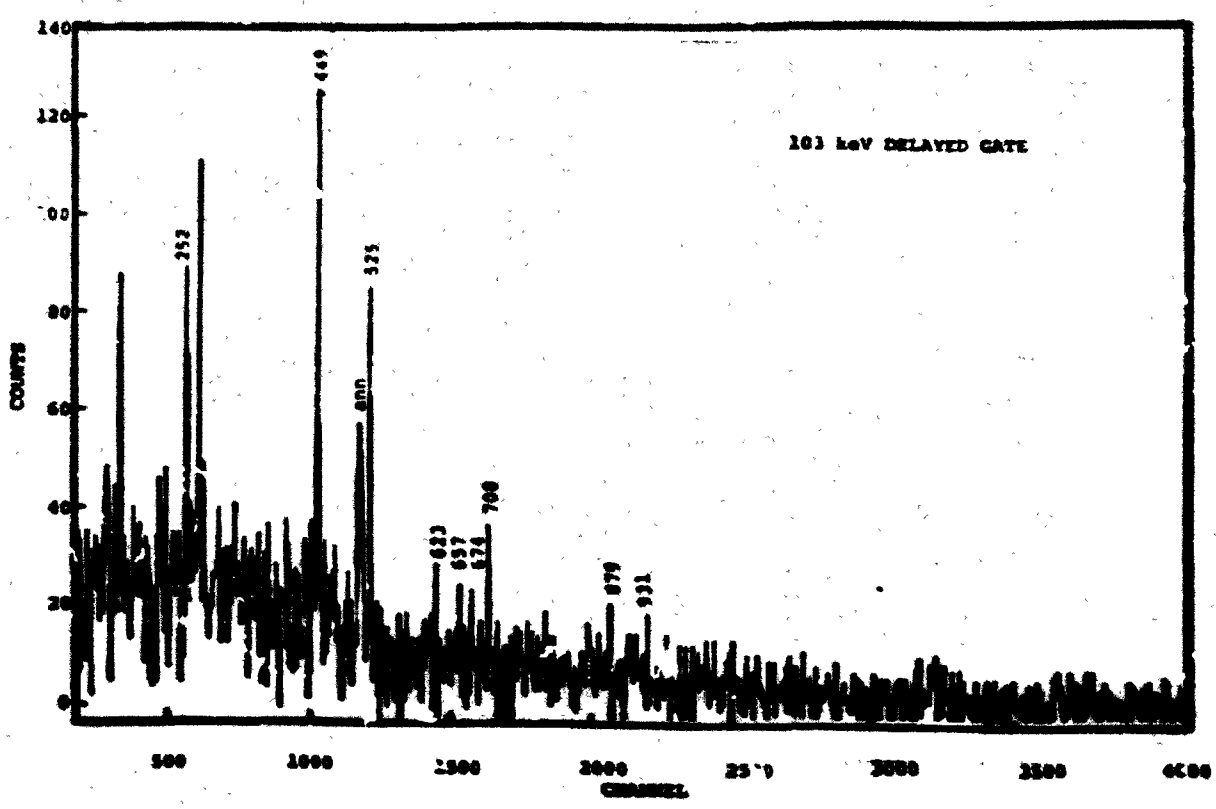

Figure 4-4. Background-Subtracted Coincidence Gates for the 103 keV Line in ^{187m,g}Hg Decay With Prompt and Delayed TAC Bounds.

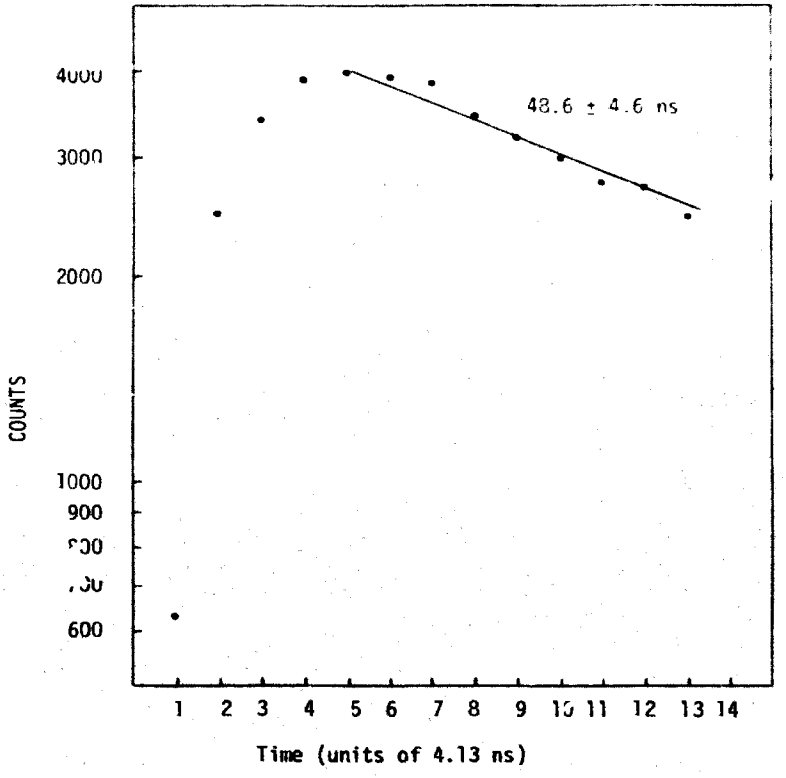

Figure 4-5. TAC Spectrum of the 103 keV Transition Between the $h_{11/2}$ and $h_{9/2}$ Bandheads. The transition is delayed due to shape isomerism, as discussed in Chapt. V.

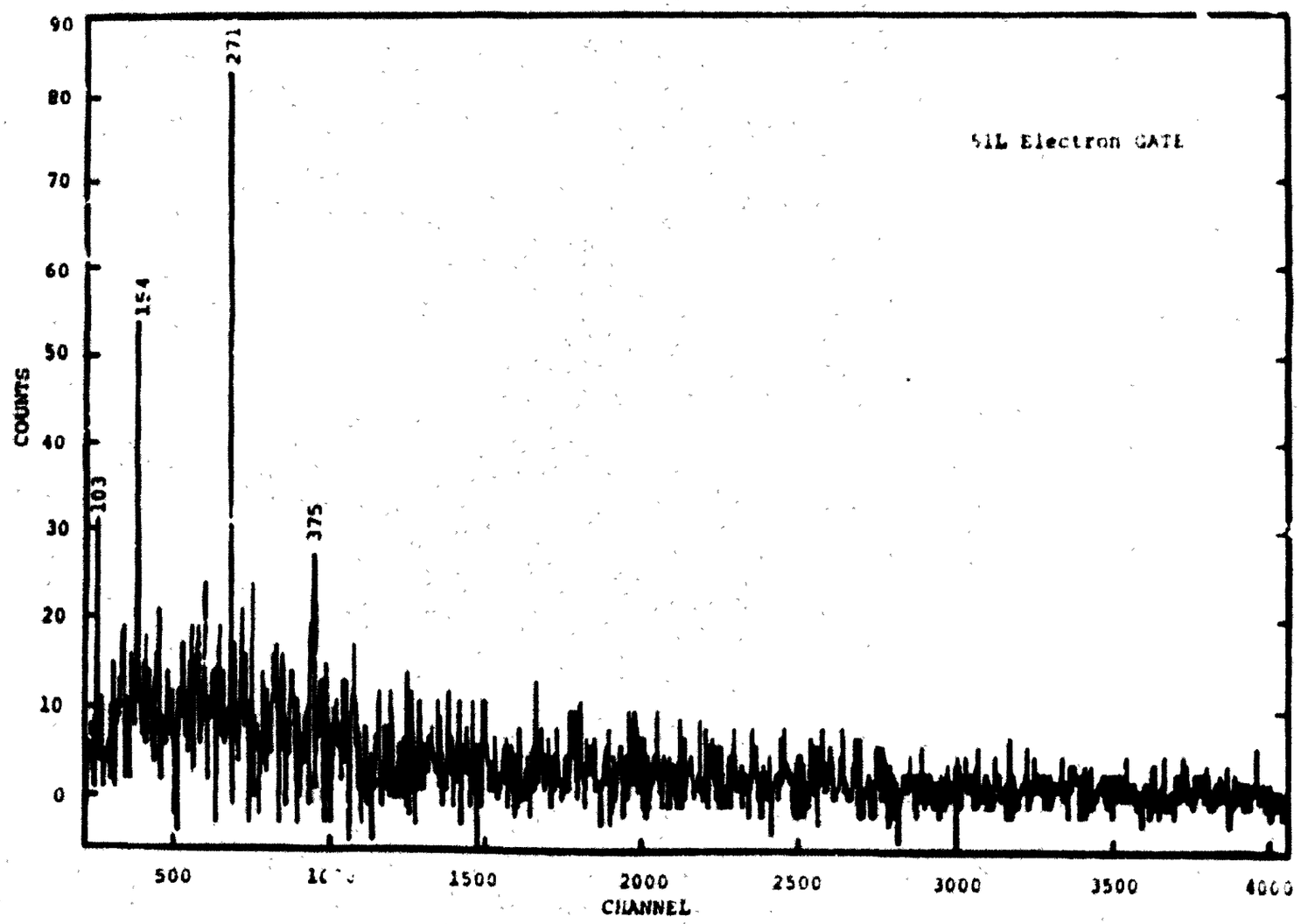

Figure 4-6. Background-Subtracted Coincidence Gate for the 51 keV L Electron Line in ^{187m,g}Hg Decay.

Table 4-3. Internal Conversion Coefficients and Multipolarity Assignments for Lines in the Decay $^{187m,g}Hg \rightarrow {}^{187}Au$.

	Theoretical $\alpha_K \times 10^3$ a)			Present Work		Bourgeois et al. b)	
E_γ (keV)	E1	E2	M1	$\alpha_K \times 10^3$ c)	Multipolarity	$\alpha_K \times 10^3$ c)	Multipolarity
143.1	137	376	2225	5980 (1670)	M1	3000 (1000)	M1
153.7	115	321	1816	1702 (884)	M1 + E2	1000 (300)	M1 + E2
203.4	57	164	826	935 (178)	M1	650 (150)	M1 + (E2)
205.4	56	160	804	666 (131)	M1 + E2	700 (150)	M1 + (E2)
220.8*	46	134	658	344 (63)	M1 + E2	280 (60)	M1 + E2
233.4**	41	116	563	116**	E2	110 (30)	E2
240.3	38	108	520	158 (31)	E2	120 (30)	E2
252.0	33	96	456	223 (56)	M1 + E2	300	(E2)
255.2	33	93	441	393 (106)	M1	380 (100)	M1
265.6	30	85	395	192 (173)	M1 + E2		
271.5	28	80	372	351 (56)	M1 + E2	300 (60)	M1 + E2
284.2	25	71	329	279 (76)	M1		
298.5*	22	63	288			23 (6)	E1
319.0	19	54	240	94 (33)	E2	70	E2
322.8	19	52	233	439 (79)	M1 + E2 +E0		
334.6	17	48	211	47 (7)	E2	42 (12)	E2
349.2	16	43	188	250 (60)	M1	220 (5	M1

Table 4-3. (continued)

	Theoretical $\alpha_K \times 10^3$ a)			Present Work		Bourgeois et al. b)	
E_γ (keV)	E1	E2	M1	$\alpha_K \times 10^3$ c)	Multipolarity	$\alpha_K \times 10^3$ c)	Multipolarity
363.4	14	39	169	<300	M1	230 (60)	M1
376.1	13	36	154	84 (12)	M1 + E2	110 (30)	M1 + E2
381.9	13	35	148	87 (58)	M1 + E2		
387.9	12	34	142	436 (141)	M1 + E2 + E0		
393.1	12	33	137	137 (38)	M1	160 (40)	M1
407.3	11	30	125	287 (165)	M1		
10.7	11	30	122	170 (40)	M1	130 (30)	M1
429.8	10	26	108			88 (10)	M1 + E2
438.7	9	25	102	32 (7)	M1 + E2	34 (8)	M1 + E2
449.3	9	24	96	21 (3)	E2	27 (6)	E2
459.4	9	23	90	62 (26)	M1 + E2	120 (30)	M1
461.9	8	23	89	34 (6)	M1 + E2	80 (20)	M1 + E2
470.1	8	22	85	30 (7)	E2	26 (7)	E2
472.6	8	22	84	28 (9)	E2	<40	M1 + E2
476*	8	21	82			(d)	
484.2	8	20	79	158 (41)	M1		
499.2	7	19	73	61 (10)	M1	80 (20)	M1
501.8	7	19	72			<100	(E1)

Table 4-3. (continued)

	Theoretical $\alpha_K \times 10^3$ a)			Present Work		Bourgeois et al. b)	
E_γ (keV)	E1	E2	M1	$\alpha_K \times 10^3$ c)	Multipolarity	$\alpha_K \times 10^3$ c)	Multipolarity
525.2	6	17	64	44 (6)	M1 + E2	65 (10)	M1
537.0	6	16	60	32 (24)	M1 + E2	10	(E1)
564.4	6	15	53	20 (10)	E2		
582.5	5	14	49	19 (5)	M1 + E2		
602.5	5	13	45	53 (23)	M1	40 (8)	M1
624.8*	4	12	40			6 (1)	E1
639.1	4	11	38	30 (6)	M1 + E2	33 (6)	M1 + (E2)

* Multiply assigned.

** Normalized to pure E2.

(a) ref. 85

(b) ref. 30

(c) Errors are in parentheses and indicate uncertainties in the last significant figures reported.

(d) Bourgeois et al. report $\alpha_K = 0.043 \pm 0.010$ for the 475.8 keV line and $\alpha_K = 0.85 \pm 0.20$ for the 476.6 keV line with multipolarity assignments of M1 + E2 and M1, respectively.

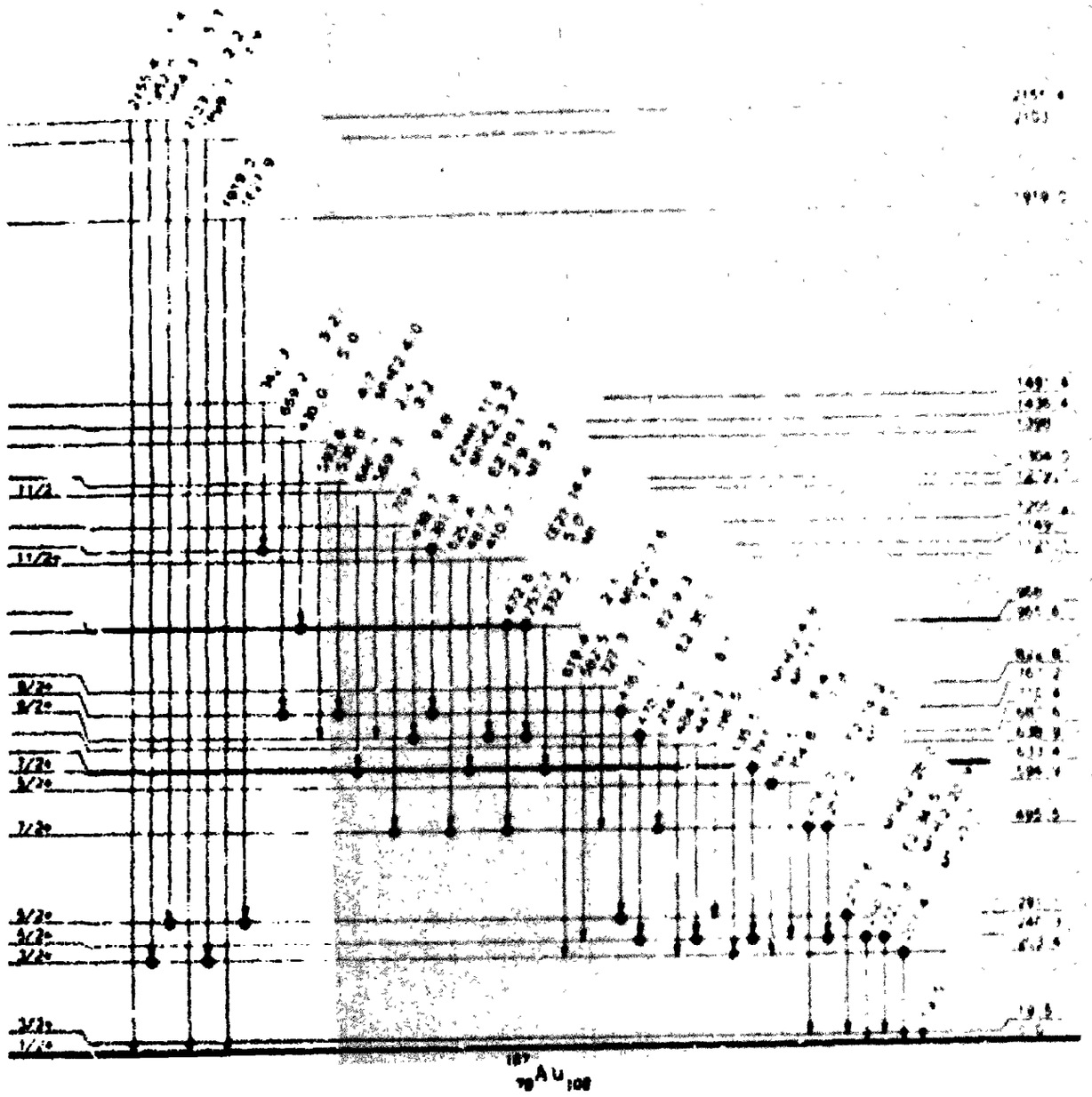

Figure 4-7 (a). Decay Scheme for $^{187m,g}Hg$: Part I - The Level Associated with the $s_{1/2}$, $d_{3/2}$ and $d_{5/2}$ Bands. Coincidences are denoted by ● .

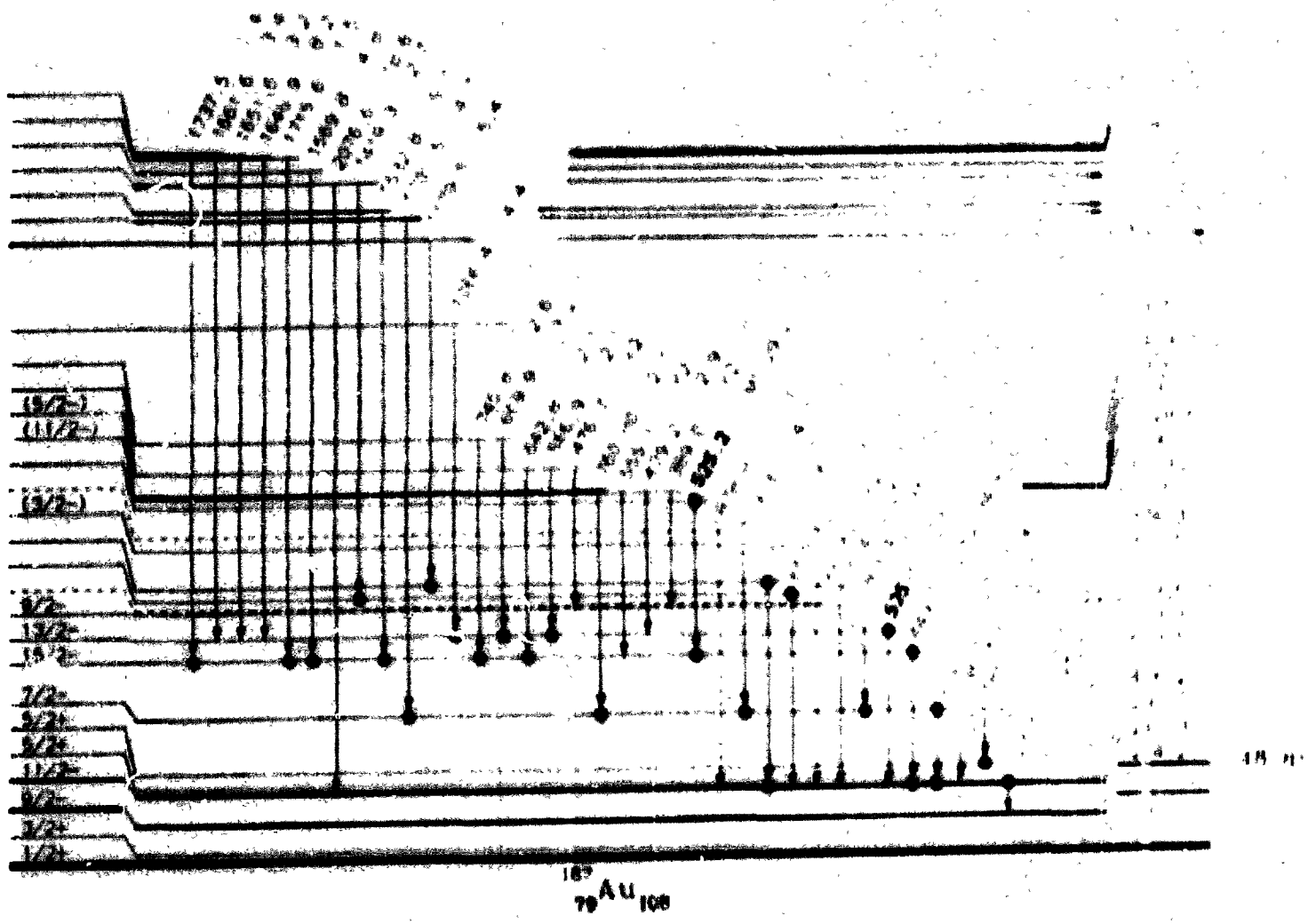

Figure 4-7 (b). Decay Scheme for $^{187m,g}Hg$: Part II - The Levels Associated with the $h_{11/2}$ Band.
Coincidences are denoted by • .

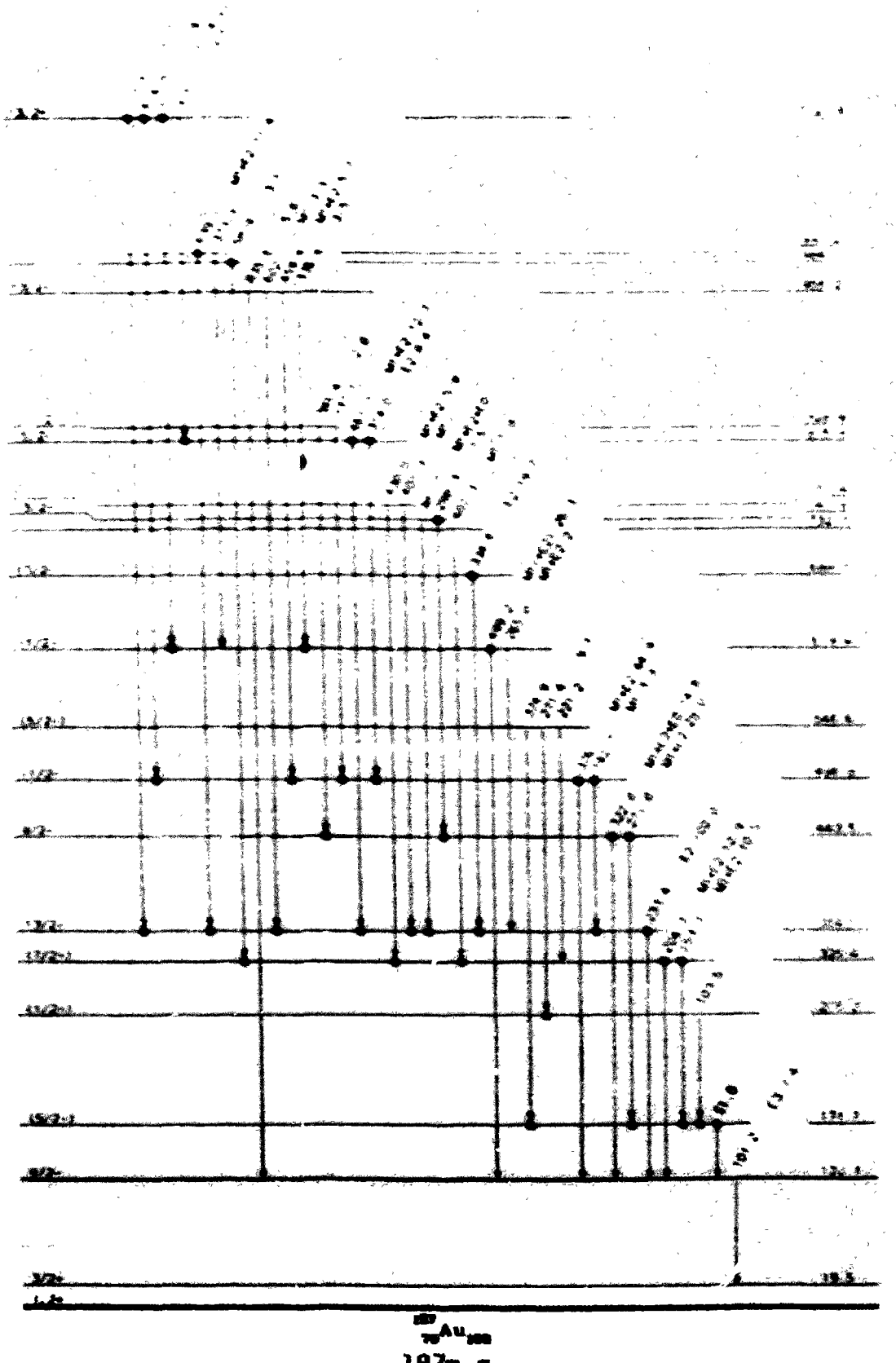

Figure 4-7 (c). Decay Scheme for $^{187m,g}Hg$: Part III - The Levels Below 1122 keV Associated with $h_{9/2}$ and $i_{13/2}$ Bands. Coincidences are denoted by ● .

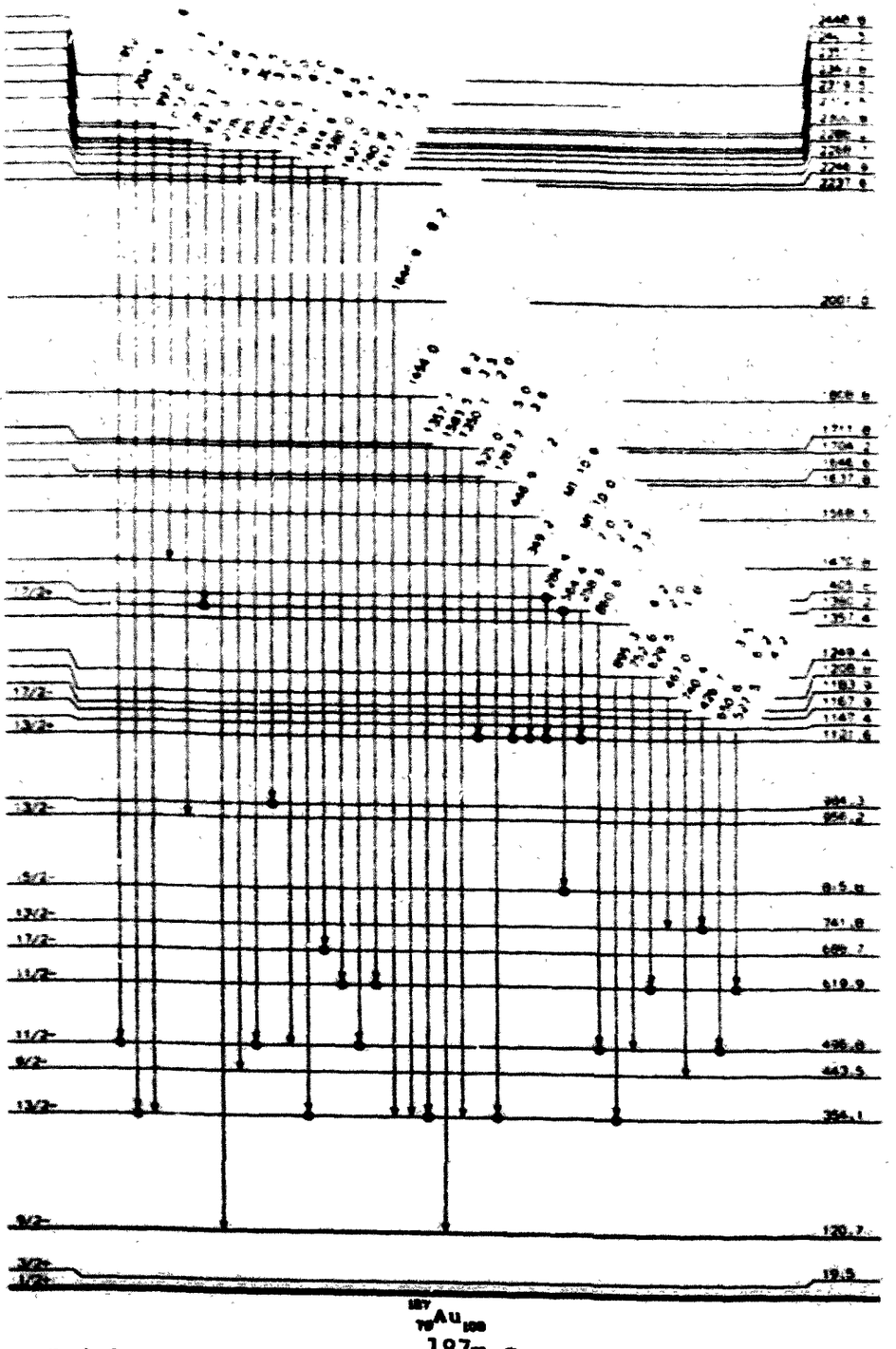

Figure 4-7 (d). Decay Scheme for $^{187m,g}Hg$. Part IV - The Levels Above 1122 keV Associated with the $h_{9/2}$ and $i_{13/2}$ Bands. Coincidences are denoted by ● . Levels below 1122 keV not populated by transitions from levels above 1122 keV are not shown.

intensities from a different experiment (Run 1-b), and a consistent normalization between the two was never achieved. The results presented here were arrived at for the most part from the [illegible]-t and [illegible]-multiscaled data during Run 1-b.

Analysis of the ^{187}Au decay data was similar to that for ^{187}Hg decay. Gated coincidence spectra were generated on the Tennecomp system from list data taken during the experiment and these spectra, with the singles spectra, were analyzed with the SEL-840A. Fits of strong peaks were made in each multiscaled plane, and a halflife of 8.4 $\pm$ 1.8 min was determined for the ^{187}Au decay, in agreement with refs. 15, 28. Energies and intensities of assigned lines are given in Tables 4-4, coincidence relationships are shown in Tables 4-5, and the data are presented in an energy level scheme in Fig. 4-8. Previous work[17,18] was used to help construct the energy level scheme. The ground state spin in ^{187}Pt has been measured as 3/2 in atomic beam experiments at Uppsala[12].

Table 4-4(a). Energies and Relative Intensities of Gamma Rays placed in the Decay $^{187}Au \rightarrow {}^{187}Pt$.

E_γ (keV) [a]	I_γ [a,b]	E_γ (keV) [a]	I_γ [a,b]
49.0 (4)[c]		546.0 (2)	10.7 (5)
51.5 (3)[c]		559.7 (2)	13.7 (6)
64.9 (4)[c]		560.2 (4)	21.3 (8)
74.6 (3)[c]		577.9 (2)	4.1 (3)
112.7 (4)	<1	582.8 (2)	4.8 (3)
116.0 (2)	3.1 (2)	590.9 (2)	7.4 (4)
126.8 (4)	2.9 (9)	595.1 (2)	6.1 (4)
137.9 (4)	5.3 (10)	609.2 (2)	7.8 (4)
165.0 (2)	3.4 (2)	611.0 (4)	1.5 (4)
166.5 (2)	6.1 (3)	620.7 (2)	23.3 (8)
181.3 (2)	14.5 (9)	625.1 (2)	3.1 (5)
185	26.5 (40)	634.8 (2)	16.3 (6)
186.1 (3)	7.3 (40)	706.1 (2)	26.1 (20)
190.7 (2)	17.2 (10)	706.6 (4)	<5
208.5 (3)	1.5 (13)	720.2 (2)	14.0 (5)
209.2 (2)	3.4 (14)	729.9 (2)	5.9 (10)
213.8 (2)	5.9 (3)	731.0 (3)	2.4 (9)
235.6 (3)	8.3 (8)	773.2 (5)	5.3 (11)
236.9 (3)	7.6 (8)	781.2 (2)	2.6 (4)
247.6 (2)	14.6 (9)	832.9 (2)	15.0 (5)
251.4 (2)	14.8 (12)	900.0 (4)	<2
260.7 (2)	2.7 (2)	914.5 (2)	40.7 (10)
263.0 (2)	1.4 (2)	981.7 (3)	2.8 (8)
317.3 (5)	2.6 (5)	1052.4 (5)	<2
351.7 (2)	13.2 (7)	1080.1 (2)	4.6 (4)
354.9 (3)	2.6 (2)	1119.6 (4)	1.8 (3)
369.1 (2)	10.3 (5)	1150.1 (4)	1.9 (5)
374.3 (2)	10.1 (10)	1172.5 (4)	2.4 (9)
374.8 (4)	6.8 (10)	1189.3 (2)	13.2 (5)
390.3 (2)	16.9 (8)	1266.3 (2)	34.0 (7)
400.7 (2)	10.1 (5)	1331.7 (2)	100
416.6 (2)	7.6 (4)	1383.9 (3)	4.5 (5)
422.9 (2)	4.7 (3)	1408.0 (2)	40.5 (7)
426.3 (2)	25.3 (12)	1417.7 (5)	7.6 (4)
429.5 (2)	8.9 (6)	1428.6 (6)	2.0 (5)
433.5 (2)	2.4 (3)	1439.4 (5)	2.4 (5)
456.6 (2)	6.7 (5)	1519.7 (3)	2.4 (3)
468.4 (2)*	6.0 (4)	1601.4 (5)	2.5 (4)
482.4 (2)*	3.6 (3)	1643.0 (5)	1.9 (4)
492.8 (4)**	1.4 (2)	1727.7 (2)	9.7 (6)
508.0 (4)		1756.2 (2)	10.2 (4)
541.9 (2)	5.5 (4)	1767.0 (5)	4.9 (3)

Table 4-4(a) (continued)

E_γ (keV) [a]	I_γ [a,b]	E_γ (keV) [a]	I_γ [a,b]
1777.8 (2)	7.1 (4)	1991.2 (3)	14.9 (14)
1826.1 (3)	4.0 (4)	2007.6 (3)	8.2 (5)
1964.0 (3)	13.8 (10)	2016.8 (2)	10.3 (4)
1987.0 (3)	13.0 (5)	2027.7 (4)	16.4 (5)

* Not placed in decay scheme.

** Seen in electron data only.

(a) Errors are in parentheses and indicate uncertainties in the last significant figures reported.

(b) Intensities are relative to I_γ (1331.7) = 100.0.

(c) Energies determined from energy differences of known levels.

Table 4-4(b). Energies and Relative Intensities of Gamma Rays Assigned to $^{187}Au \rightarrow ^{187}Pt$ Decay but not Placed in the Decay Scheme. Only lines with $I_\gamma \geq 3$ are included.

E_γ (keV) [a]	I_γ [a,b]	E_γ (keV) [a]	I_γ [a,b]
252.6 (2)	9.5 (5)	1399.0 (3)	3.3 (5)
405.6 (2)	3.9 (5)	1433.6 (3)	12.8 (6)
413.3 (3)	5.9 (6)	1452.1 (3)	23.4 (6)
552.7 (4)	3.9 (20)	1474.2 (4)	3.1 (5)
575.7 (2)	3.4 (3)	1477.6 (4)	3.2 (5)
614.0 (2)	4.2 (3)	1612.3 (4)	3.0 (5)
786.0 (2)	3.0 (4)	1640.7 (3)	3.7 (4)
937.5 (3)	5.1 (6)	1805.7 (3)	5.0 (4)
959.1 (2)	3.8 (3)	1834.2 (4)	3.5 (5)
1007.6 (3)	5.0 (17)	1847.7 (4)	5.3 (5)
1145.1 (3)	3.4 (12)	1876.8 (4)	3.4 (6)
1253.1 (3)	3.2 (4)	1909.8 (3)	8.8 (9)
1277.2 (3)	3.5 (4)	1943.1 (4)	3.0 (5)
1313.6 (2)	26.4 (8)	2056.1 (3)	11.1 (4)
1359.2 (3)	6.7 (8)	2085.3 (3)	9.7 (4)
1378.9 (3)	6.7 (6)	2105.5 (5)	3.8 (6)

(a) Errors are in parentheses and indicate uncertainties in the last significant figures reported.

(b) Intensities are relative to I_γ (1331.7) = 100.0.

Table 4-5( ). Coincidence Relationships of Gamma Rays Placed in the $^{187}Au \rightarrow ^{187}Pt$ Decay Scheme.

Gate Energy (keV) [a]	Coincidences [b]
116.0	M: 235.6, ann [c] W: 133, 310, 1374
181.3	S: 235.6, 590.9 M: 559.7 W: 300, 329, 1060, 1149
185 (unassigned)	S: 345, 390.3 M: 131, 469, 602 W: 445, 455, 481, 769, 1459, 1908, 2234
186.1	S: 247.6, 374.3, 832.9 M: 706.1, 1080.1, 1756.1 W: 1767.0, 1777.8
190.7	S: 235.6 M: 319, 559.7, 590.9, 832.9 W: 429, ann, 629, 633, 723, 767, 1088, 1644
208.5	M: 706.1
209.2	M: 247.6 W. 1122
213.8	M: 1118, 1189.3 W: 237, 559, 914, 1052
235.6	S: 181.3, 190.7, 914.6 M: 165.1, 699 W: 174, 1492
236.9	M: 1189.3
247.6	S: 251.4, 832.9 M: 209.2, 260.7 W: 134, ann, 898, 1520, 1573
251.4	S: 247.6, 832.9 M: 374.3, 390, 456 W: ann, 688, 1080
251 (delayed)	M: 162, 170, 187

Table 4-5(a) (continued)

Gate Energy (keV) [a]	Coincidences [b]
260.7	M: 247.6 W: 165.6, 374.3, 390, 621, 705
351.7	S: 914.5 M: 354.9, ann W: 1068, 1172.5
354.9	M: 369.1, 426.3, 559.7
369.1	S: 914.5
374.3	S: 186.1, 251.4, 706.1
374.8	M: 914.5
390.3	S: 185, 469 M: 482.4 W: 204, 251 800, 844, 937, 1384
400.7	S: 914.5 M: 224, 258, 354.9, 426, 1172.5 W: 192, 263, 494, 658, 664, 1100
416.6	M: 220, 625, 959 W: 706, 914.5
422.9	M: 634.8
426.3	S: 914.5 M: 208.5, 354.9, ann, 981.7, 1172.5 W: 172, 193, 410, 450, 608, 1008
456.6	M: 252, 832.9
468.4	S: 390.3 W: 185
482.4	S: 390.3 M: 832.9
541.9	W: 332, 430, 1417.7
546.0	S: 720.2

Table 4-5(a) (continued)

Gate Energy [a]	Coincidences [b]
559.7	S: 354.9, 492.8, 590.9, 706.6, 729.7, 781.2 M: 426.3, ann W: 606, 854
560.2	S: 706.1, 731.0
577.9	S: ann, 706.0 W: 185
582.8	no coinc.
590.9	S: 181.3, 559.7 W: 190.7
599.1	W: ann
609.2	S: 706.1, 731.0
611.0	no coinc.
620.7	S: 720.2 M: 247, 288, ann, 562, 683
625.1	M: 416, 706.1
634.8	S: 422.9, 706.0 M: 234, 376, 772, 799
706.1	S: 208.5, 374.3, 560.2, 577.9, 609.2, 634.8 M: 260.7, 426.3, ann, 625.1
706.6	S: 559.7
706 (unassigned)	M: 310, 327, 486
720.2	S: 546.0, 520.7 M: ann, 595.1, 611.0, 1114
729.9	S: 559.7 W: 249
773.2	W: 233, 560.2, 634.8
781.2	M: 250, 559.7

Table 4-5(a). (continued)

Gate Energy (keV) [a]	Coincidences [b]
832.9	S: 186.1, 247.6, 433.5, 456.6, 482.4, ann M: 251.4, 314 W: 130, 209.2, 323
914.5	S: 235.6, 351.7, 369.1, 400.7, 426.3 M: 190.7, 374.8, ann
981.7	W: 351.7, 426.3, 696
1080.1	M: 251.4
1119.6	W: 209.2, ann
1172.5	W: 400.7, 426.3
1189.3	S: 213.8 M: 236.9 W: 132, 262
1266.3	M: ann
1331.7	S: ann W: 307, 414, 687
1383.0	M: 390.3 W: 185, 251
1408.0	M: ann
1417.7	M: 541.9
1428.6	W: 541.9
1439.4	W: 202, 541.9
1601.4	W: 425.3
1643.0	W: 426.3
1727.7	M: 213.8
1756.2	S: 186.1, 251.4 M: 209.2

Table 4-5(a). (continued)

Gate Energy [a]	Coincidences [b]
1767.0	M: 186.1
1777.8	M: 186.1
1826.1	W: 181.3, 190.7
1964.0	no coinc.
1987.0	no coinc.
1991.2	no coinc.
2007.6	no coinc.
2016.8	no coinc.
2027.7	no coinc.

(a) Energies for multiplets unresolved in the singles data are determined as described in the text. Each multiplet component and its coincidences are listed separately with unassigned coincidences listed after the last component.
(b) Coincidences are identified as S (strong, >90% confidence in assignment), M (moderate, >70% confidence in assignment), or W (weak, >40% confidence in assignment). Exact energies are given for assigned coincidences, approximate energies for unassigned.
(c) ann denotes annihilation line (511 keV).

Table 4-5(b). Coincidence Relationships of Gamma Rays Assigned to the Decay ^{187}Au-^{187}Pt but not Placed in the Decay Scheme. Only lines with I ≥ 3 are included.

Gate Energy (keV)	Coincidences [a]
575.7	S: ann W: 264, 671
614.0	no coinc.
786.0	W: 181, 420, 486, 630
937.5	W: 193, 467, 816
959.1	W: 183, 224, 416, 472
1145.1	W: 182, 237, 334
1229.0	no coinc.
1253.1	no coinc.
1318.6	W: ann
1378.9	no coinc.
1433.6	W: 322, ann
1452.1	M: ann
1805.7	no coinc.
1847.7	W: 190, 234, ann
1909.8	no coinc.
2056.1	no coinc.
2085.3	no coinc.

(a) Coincidence energies are accurate to ± 2 keV.

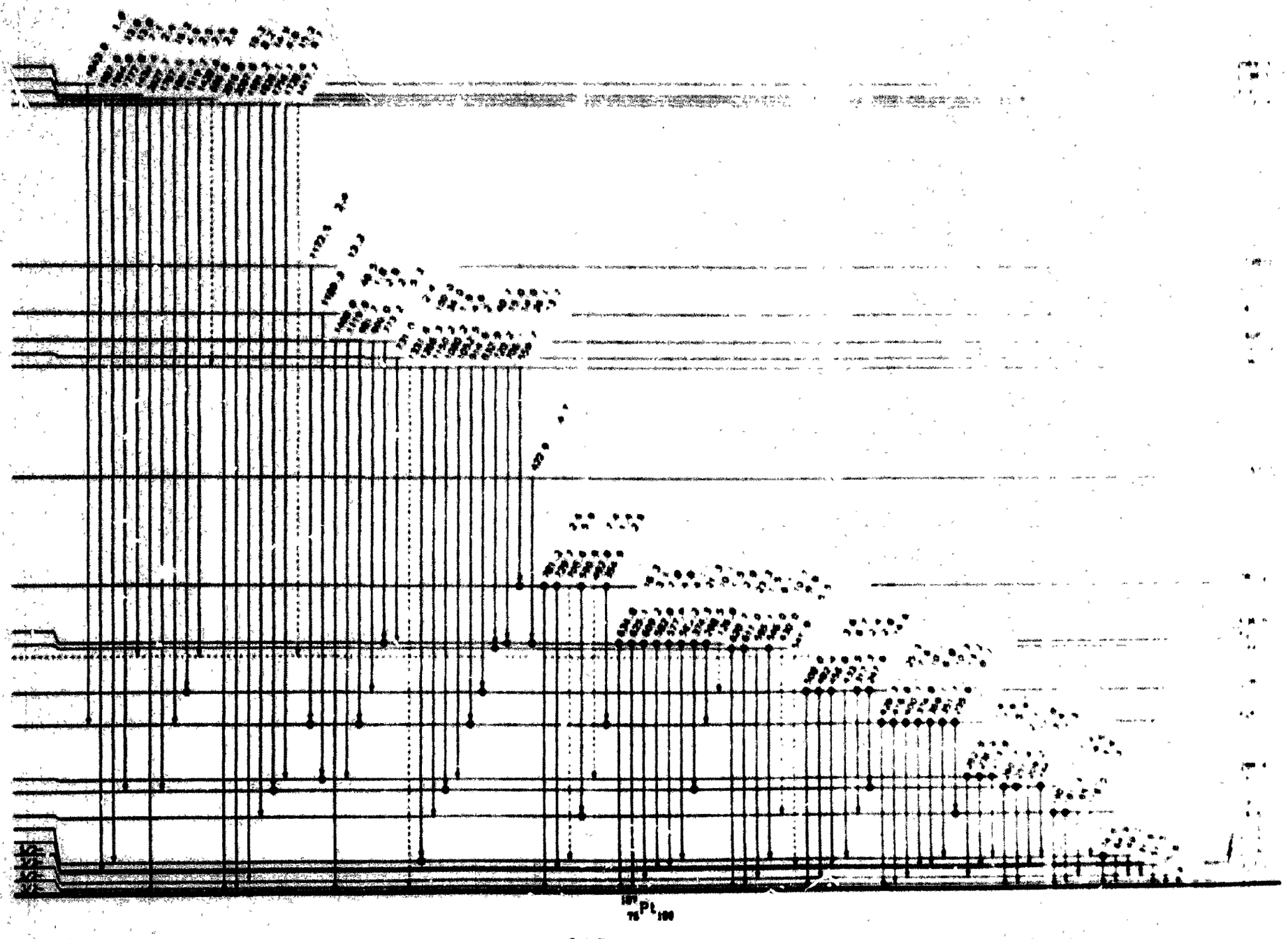

Figure 4-8. Decay Scheme for ^{197}Au. Coincidences are denoted by ● .

CHAPTER V

INTERPRETATION OF RESULTS

The two nuclei studied in this work are in the "transitional" region between the strongly deformed nuclei in mid-shell and the double shell closure at ^{208}Pb. The odd-A transitional nuclei in this region have been interpreted by Meyer ter Vehn[5,6] as the coupling of a pure-j nucleon to a triaxial core. This asymmetric rotor model has met with varying degrees of success and is used as the theoretical basis underlying this work because of its simplicity (see Chapter II). This model readily reproduces several phenomena observed in the transitional region: Both particle and hole spectra are observed, and both oblate and prolate shapes exist in this region. In particular, an oblate-to-prolate shape transition is observed in the $h_{9/2}$ bands of the odd-mass gold nuclei as they become more neutron deficient. This shape change manifests itself in the transition from a strongly coupled $h_{9/2}$ band structure in the nuclei $^{191-195}$Au to a decoupled $h_{9/2}$ band structure in $^{185-189}$Au (see Chapter II and Fig. 5-3). The asymmetric rotor model as interpreted by Meyer ter Vehn is equally capable of describing particle and hole couplings to a triaxial core, oblate or prolate, and can reproduce this trend in the $h_{9/2}$ band in the gold nuclei.

All Meyer ter Vehn calculations presented in this work use the "standard" parameters of refs. 5 and 6. These standard parameters

are determined from experimental energy spectra of the neighboring even-even core nuclei, and no attempt has been made to fit the odd-A spectra by varying these model parameters. The addition of the odd nucleon to the even-even core, however, may polarize the core such that the standard parameters should be modified to represent the effective core seen by the nucleon. This polarization effect raises the question of whether well-defined rigid triaxial shapes exist. Microscopic calculations[66,67] predict that the transitional nuclei are γ-soft, whereas the Meyer ter Vehn calculation of the asymmetric rotor assumes a rigid triaxial shape. This question of triaxiality has recently been explored by Girod and Grammaticos[86] and Baktash et al.[87]. Girod and Grammaticos find that, on the basis of Hartree - Fock - Bogolyubov calculations, static triaxial shapes are rare, but point out that γ-softness leads to dynamic triaxiality in a number of cases. Baktash et al. find that experimental measurements favor a γ-soft core over a rigid triaxial shape for ^{194}Pt. The γ-softness of the transitional nuclei is further discussed below in relation to the ^{187}Au nucleus.

The existence of shape isomerism in the odd-mass gold nuclei has recently been demonstrated[26,72,88]. The ^{187}Au nucleus studied in the present work also exhibits shape isomerism. This isomerism is due to the different core shapes available for coupling to the odd nucleon. For ^{187}Au, the odd proton can couple as a particle (in the $h_{9/2}$ orbital, for example) to the prolate ^{186}Pt core or as a hole (in the $h_{11/2}$ orbital, for example) to the oblate ^{188}Hg core. Gamma-ray transitions between members of the $h_{9/2}$ and $h_{11/2}$ bands will then be

hindered by the shape change, as discussed below. In addition to the ground state bands, there are excited 0^+ states in the ^{186}Pt and ^{188}Hg cores which have collective structure associated with them and which should also couple to the odd nucleon. One of the major objectives of the present work is the location of the states due to the coupling of the odd proton to these 0_2^+ states in the core nuclei. For the ^{188}Hg core, used with hole states in ^{187}Au, the 0_2^+ state has a strongly deformed shape[70] such that Nilsson states should appear in the odd proton coupling. Candidates for these Nilsson states have been found and are discussed below. The ^{186}Pt core, used with the particle states in ^{187}Au, also has an excited 0^+ state but its structure is not understood at present. The coupling of the odd proton to this state has also been observed in the present work and may require the introduction of a new isomeric nuclear degree of freedom, as discussed below.

It should be pointed out that the use of nuclear systematics played an important role in constructing the ^{187}Au energy level scheme. Previous work at UNISOR on $^{189\text{-}195}$Au[11,88,89] and current UNISOR work on ^{185}Au[90] were used to follow systematic trends of the energy levels in the odd-mass gold nuclei from the stable ^{197}Au nucleus to the region far from stability under study in the present work. Further details on the use of these systematics are given below.

^{187}Pt

The nucleus ^{187}Pt was studied in the decay (8.4 min) ^{187}Au→(2.4 hr) ^{187}Pt as described in Chapter III and the energy level scheme (Fig. 4-9) constructed from the coincidence data. Previous work[16,18] is confirmed and supplemented by the present work with a few points of

disagreement. It should be pointed out, however, that the present study is incomplete for the following reasons. First, as noted in Chapter IV, the conversion electron data were of low quality due to poor statistics and the unavailability of equipment to observe low energy ($E_e \leq 30$ keV) conversion electrons of the transitions between the low energy levels in the scheme. Thus, there is a lack of conversion coefficients to help make spin assignments throughout the scheme, and an absence of coincidence information at low energy. Secondly, the ^{187}Au decay spectra were contaminated with ^{187m,g}Hg decay lines, since the mass chain was entered at ^{187}Tl or ^{187}Hg in each experiment (see Table 3-1). Finally, as discussed in greater detail below, the decay scheme is unusually complex.

In-beam reaction spectroscopy[24] has clearly established the existence of the $i_{13/2}$ neutron band in $^{187-193}$Pt. An M2 isomeric transition of 117 keV has been observed with in-beam studies of ^{187}Pt[25] and it has been interpreted as the transition depopulating the 11/2+ bandhead[22] of the $i_{13/2}$ band. The 7/2- level fed by this decay has not been located relative to the ground state, which has a spin of 3/2[13,14]. This 117 keV transition is observed in the gamma and electron singles spectra of the present work, but its isomeric nature ($T_{1/2}$ = 311 μs) prohibits its appearance in coincidence data. Since it appears that only the 1/2+ ground state of ^{187}Au decays to ^{187}Pt (see Chapter IV), only low-spin states of ^{187}Pt are populated. Therefore, only low-spin members of the $i_{13/2}$ neutron band are directly populated, and the 11/2+ bandhead decay observed in the present work occurs through indirect population of this level from low-spin members of the band. These

low-spin levels have not been located in the present work. The asymmetric rotor model calculations of Meyer ter Vehn[5,6] appear to describe adequately the $i_{13/2}$ bands in the odd-A platinum isotopes[18,22,91]. In ^{187}Pt, the energy spacings of the favored decoupled members of the $i_{13/2}$ band more closely resemble the energy spacings of the ^{188}Pt ground state band than they do the ^{186}Pt ground state band. Thus the Meyer ter Vehn calculation describes the nucleus ^{187}Pt as a neutron hole in a ^{188}Pt core.

The keys to constructing the ^{187}Pt level scheme (Fig. 4-9) were the six levels below 100 keV (including the ground state). Transitions between these levels are reported in ref. 18. In the present work, these levels are further established by the observation of coincidences between higher energy transitions. For example, the level at 426.3 keV is populated by the intense 914.6 keV gamma ray from the level at 1340.9 keV. The 914.6 keV gamma ray is in coincidence with the 351.7, 369.1, 374.8, 400.7, 416.6 and 426.3 keV gamma rays. These gamma rays thus decay to the levels at 74.6, 57.2, 51.5, 25.6, and 9.3 keV and the ground state, respectively. The level at 1340.9 keV similarly decays to other levels which subsequently decay to these low energy levels. The 559.7, 706.1, 720.2, 832.9, 1052.2, 1080.2, and 1150.2 keV transitions depopulate the 1340.9 keV level to the levels at 781.2, 634.8, 620.7, 508.0, 288.4, 260.7, and 190.7 keV, respectively. Coincidence gates on the gamma rays depopulating the 1340.9 keV level then show coincidences with other gamma rays, some of which decay to the energy levels below 100 keV. There is also a level at 1408.0 keV which exhibits the same pattern and several levels above 2 MeV can

also be consistently fit into this pattern.

One point of disagreement between the present work and ref. 18 is the placement of the 1331.7 keV transition, the most intense gamma ray observed in ^{187}Au decay. Bourgeois et al.[18] place this transition between a level at 1383.3 keV and the 51.5 keV level while the present assignment is between the 1340.9 keV and 9.3 keV levels. If Bourgeois et al. are correct, there should be a coincidence observed between the 1332 keV gamma ray and the 51.5 keV electron. This coincidence is not seen in the present work. As noted above, however, the e-γ-t data of the present work do not have the statistics necessary to rule out completely the assignment of ref. 18. However, the ability to fit this 1332 keV transition into the decay scheme described above strengthens the present assignment. This question of assignment can be resolved in future work by using the pre-acceleration electron detector currently under construction for use at UNISOR[92], which will allow the detection of low-energy electrons, e.g., the 9.3 keV electron in this case.

The nature and origin of the low-energy states in the odd-A platinum isotopes are not understood, so little can be said about the coupling scheme applicable to them. Bourgeois et al.[18] report experimental transition probabilities between some of these levels which are enhanced relative to single-particle estimates, indicating collective character. In addition to these low-energy levels, there are several other notable structural aspects observed in the present work. The coincidence gate at 251 keV is found to have a delayed component as well as the prompt component already assigned. This

indicates some form of isomerism in ^{187}Pt. The delayed component has not been placed in the decay scheme of the present work, and the low counting rate resulting in poor statistics prevents a measurement of the isomeric lifetime. Coincidences with this delayed component are listed in Table 4-4.

Another aspect of the present scheme is the large amount of feeding of levels at 1340 and 1408 keV and several levels above 2 MeV. These levels are obviously low-spin states, since they decay to low-spin states in ^{187}Pt and are populated by beta decay from the 1/2+ ground state in ^{187}Au. Values of log (ft) for these states have not been computed because the amount of beta decay to the ^{187}Pt ground state (3/2-) is not known.

One final feature of the present work is a group of transitions not placed in the level scheme but showing coincidences between its members. These transitions are included in Tables 4-2(a) and 4-4(a) even though they can not be unambiguously placed in the level scheme. This group includes the 185, 390, 469, 482, and 1383 keV transitions.

Finally, it should be noted that in addition to the $i_{13/2}$ coupling to the ^{188}Pt ground band, there are other possible coupling schemes for the odd neutron in ^{187}Pt. There are both particle and hole states available in this neutron region which could couple to the ground and excited bands in ^{186}Pt and to the ground and excited bands in ^{188}Pt, respectively. Also, the low-lying levels of $^{177-185}$Pt have recently been shown[16,18,93,94] to be strongly deformed (Nilsson) states, implying that such states may occur at low energy in ^{187}Pt. Some of the unplaced transitions in the present work may be due to

these couplings but more study is needed in order to conclusively elucidate these coupling schemes.

^{187}Au

In the Meyer ter Vehn model, the nucleus ^{187}Au is pictured either as a proton particle coupled to the even-even ^{186}Pt core, or as a proton hole coupled to the even-even ^{188}Hg core. As seen in a Nilsson diagram of this region (Fig. 2-3), the proton hole states available are the $d_{3/2}$, $d_{5/2}$, and $h_{11/2}$ states. The particle states available are the $s_{1/2}$ and the "intruder" states, $h_{9/2}$ and $i_{13/2}$, which cross the major Z = 82 closed shell from above at the deformation encountered in the light odd-mass gold nuclei. These intruder states have been attributed to a variety of effects[96-103].

The $h_{9/2}$ and $h_{11/2}$ states are the best candidates for a Meyer ter Vehn asymmetric rotor model assignment, since they are of high-spin and pure-j, i.e., they have opposite parity to all other neighboring states and thus do not mix with them. The $h_{9/2}$ and $h_{11/2}$ states do not mix with each other due to their respective particle and hole characters. Calculations using the Meyer ter Vehn computer code ASQRT were performed at ORNL on the IBM-360. The calculations utilized the standard parameters of refs. 5 and 6 as described above. Results of these calculations are compared with experiment in Figs. 5-2, 5-4, and 5-6. Each band in ^{187}Au is separately discussed below.

$h_{11/2}$ Band

The systematic trend of members of the $h_{11/2}$ band (Fig. 5-1) is seen to vary smoothly for the nuclei $^{187-195}$Au. All of these bands

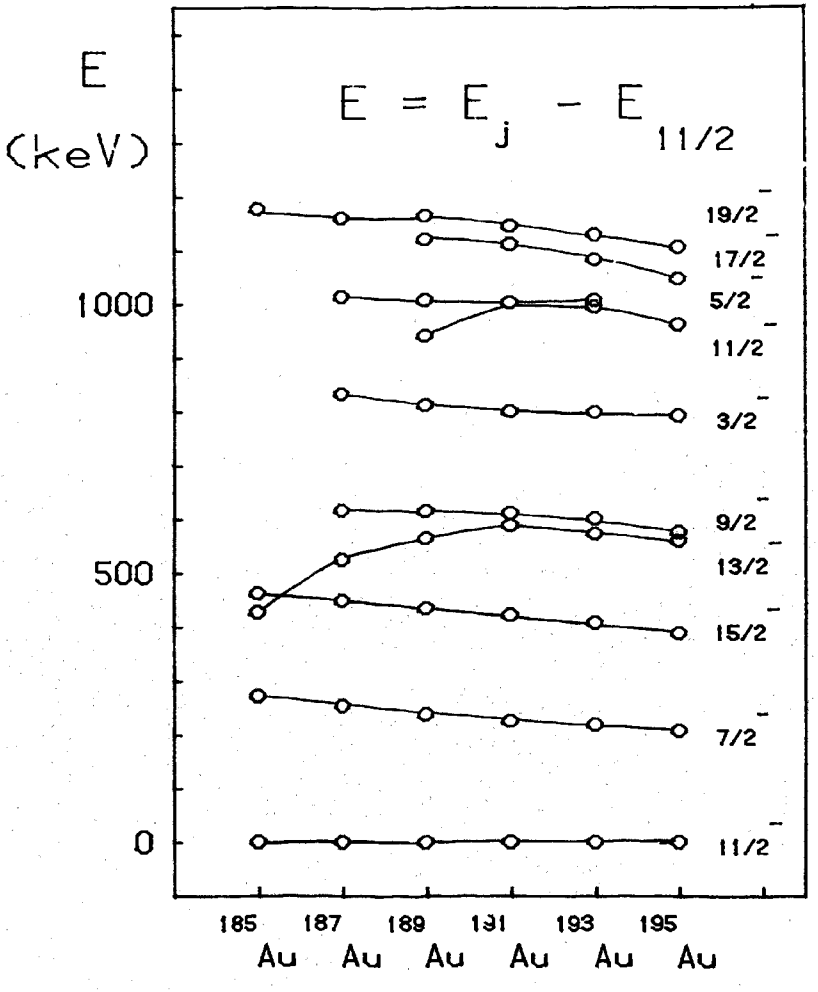

Figure 5-1. Systematics of Members of the $h_{11/2}$ Band in $^{185-195}Au$.

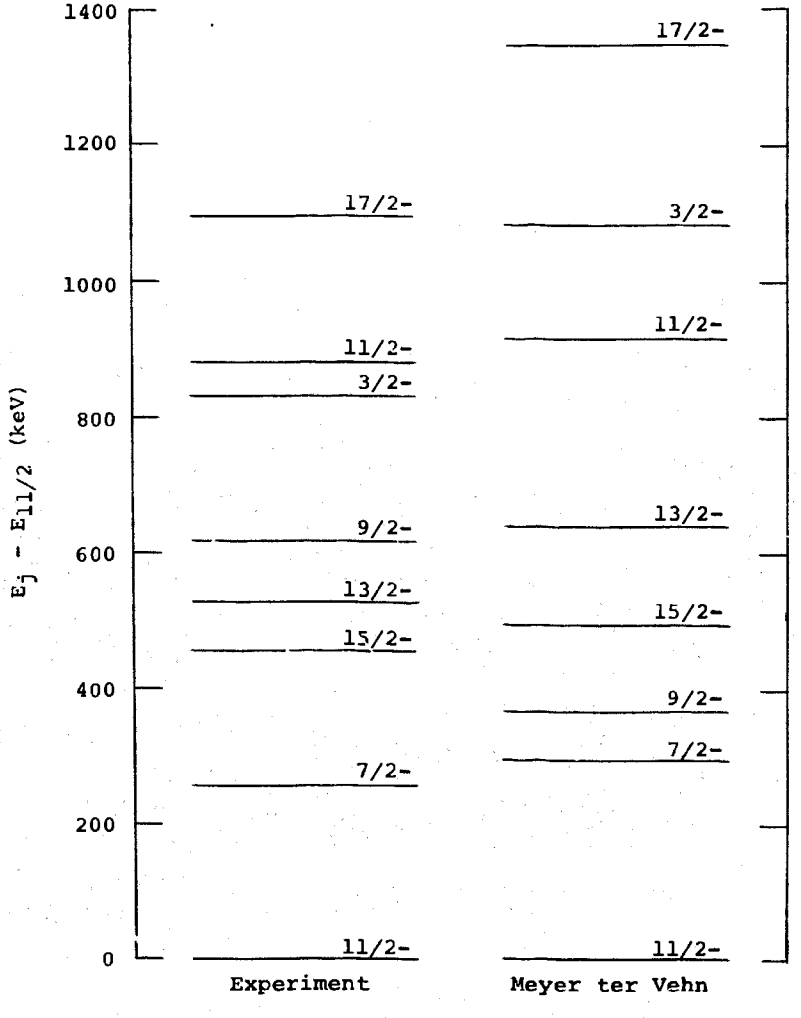

Figure 5-2. Comparison of Experimental and Theoretical (Meyer ter Vehn) $h_{11/2}$ Band in ^{187}Au.

are decoupled, which can be interpreted as a proton hole coupled to an oblate Hg core for each (see Chapter II), and indicates that these cores are stable against changing neutron number. The j, j+2 energy differences correspond closely to the 2_1^+ energies of the respective Hg cores.

A Meyer ter Vehn calculation was performed for the $h_{11/2}$ band in ^{187}Au to obtain energy levels and transition probabilities. The standard parameters for this band are $\beta = 0.14$ and $\gamma = 36^o$, i.e., it is oblate. The theoretical energy levels are compared with experiment in Figure 5-2 where they are seen to agree fairly well both in energy and in ordering of levels for $j \geq 11/2$ and for the 7/2- state, which is a member of the favored decoupled band. The transition probabilities are listed in Table 5-1 for the 9/2- → 11/2- and 9/2- → 7/2- transitions. The B(E2, and B(M1) values are those computed with the Meyer ter Vehn code, whereas the energies of the transitions are those experimentally observed. The ratio of the 9/2- → 7/2- and 9/2- → 11/2- theoretical intensities is 0.5 while the ratio of the experimental intensities is 0.9. Thus the Meyer ter Vehn calculation results in qualitative agreement with experiment.

The 11/2- bandhead decays via an M1 transition to the $h_{9/2}$ bandhead with a 48 ns halflife. This transition is delayed owing to the change in shape from the oblate $h_{11/2}$ bandhead to the prolate $h_{9/2}$ bandhead. Comparison of this halflife to that predicted by the Weisskopf single-particle estimate[104] yields a hindrance factor of $\sim 10^4$.

$h_{9/2}$ band

The $h_{9/2}$ band systematics, unlike the $h_{11/2}$ band, show a

Table 5-1. ^{187}Au Theoretical Gamma-Ray Transition Probabilities.

Band	J_i	J_f	E^*(MeV)	B(E2)** e^2b^2	B(M1)** nm^2	T(E2)/ps	T(M1)/ps	T_{tot}/ps	Rel. Int.*
$h_{11/2}$	9/2-	11/2-	0.616	0.2943	0.3060	0.3187	1.2588	1.5775	3.3
$h_{11/2}$	9/2-	7/2-	0.363	0.1217	0.9916	0.0094	0.8348	0.8442	3.1
$h_{9/2}$	11/2-	13/2-	0.143	0.0114	0.2060	8×10^{-7}	0.0106	0.0106	3.9
$h_{9/2}$	11/2-	9/2-	0.376	0.3822	0.2626	0.0351	0.2457	0.2808	44.9
$h_{9/2}$	15/2-	11/2-	0.319	0.7216	----	0.0291	----	0.0291	8.4
$h_{9/2}$	15/2-	13/2-	0.462	0.2772	0.1947	0.0712	0.3379	0.4091	12.3
$h_{9/2}$	13/2-'	13/2-	0.602	0.0456	0.0097	0.0440	0.0372	0.0812	3.3
$h_{9/2}$	13/2-'	9/2-	0.836	0.0304	----	0.1516	----	0.1516	5.6
$h_{9/2}$	13/2-'	11/2-	0.460	0.3664	0.2878	0.0921	0.4930	0.5851	5.7

* Experimental value

** Theoretical value calculated from the Meyer ter Vehn prescription of the asymmetric rotor model.

dramatic change in the level order as the neutron number changes (Fig. 5-3). For $^{191-195}$Au the $h_{9/2}$ band is strongly coupled, i.e., the level order is j, j+1, j+2, . . . which indicates a proton particle coupled to an oblate shape in the corresponding even platinum core (see Chapter II). Between ^{191}Au and ^{189}Au, the level ordering changes to a decoupled pattern which indicates prolate shapes for the platinum core nuclei corresponding to $^{185-189}$Au. Thus the even-even Pt nuclei appear to be unstable against changing neutron number.

For ^{187}Au, the Meyer ter Vehn standard shape parameters are $\beta = 0.20$ and $\gamma = 19.6^0$. The theoretical energy level scheme obtained from these parameters is compared to the experimental level scheme in Fig. 5-4. Although the experimental and theoretical energies disagree, the spin sequence is generally reproduced and every predicted level is accounted for in the experimental spectrum up to j = 17/2. The theoretical energies of the high-spin states, as noted in Chapter II, can be lowered by using a variable-moment-of-inertia (VMI) model[62,63], thus obtaining better agreement with experiment.

Theoretical transition probabilities are presented in Table 5-1 for selected transitions in the $h_{9/2}$ band. Again, experimental energies and theoretical reduced transition probabilities are used to compute the total transition probabilities. The experimental and theoretical intensity ratios are again in qualitative agreement, as seen in Table 5-2.

The $h_{9/2}$ bandhead decays via a 101.2 keV E3 transition to the 3/2+ level at 19.5 keV. Since this transition is from a prolate shape to an oblate shape and from a particle to a hole configuration, it

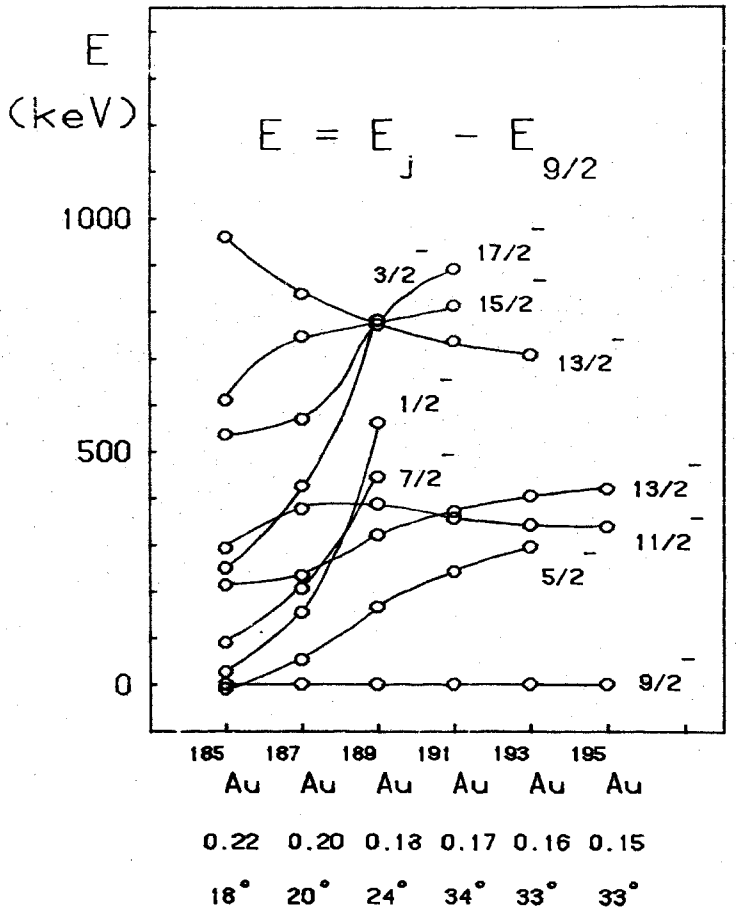

Figure 5-3. Systematics of Members of the $h_{9/2}$ Band in $^{185\text{-}195}Au$.

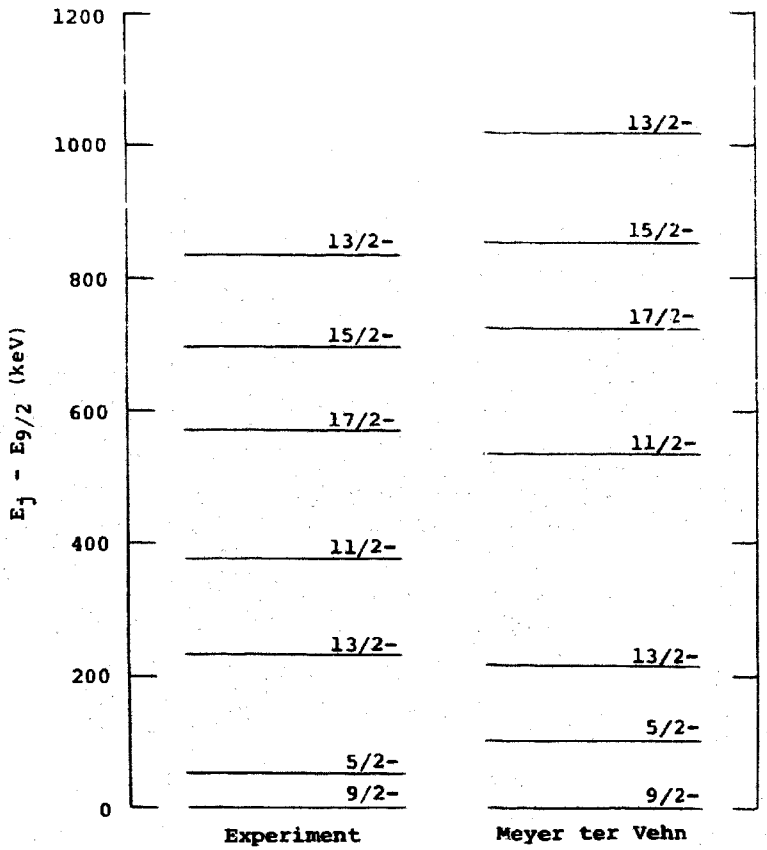

Figure 5-4. Comparison of Experimental and Theoretical (Meyer ter Vehn) $h_{9/2}$ Band in ^{187}Au.

Table 5-2. Comparison of Theoretical and Experimental Transition Probabilities in ^{187}Au.

Band	Transition 1	Transition 2	I_1/I_2 Theory	I_1/I_2 Expt.
$h_{11/2}$	9/2- → 7/2-	9/2- →11/2-	0.5	0.9
$h_{9/2}$	11/2- → 9/2-	11/2- →13/2-	26.5	11.5
$h_{9/2}$	15/2- →13/2-	15/2- →11/2-	14	1.5
$h_{9/2}$	13/2-'→13/2-	13/2-'→ 9/2-	0.5	0.6
$h_{9/2}$	13/2-'→11/2-	13/2-'→13/2-	7.2	1.7
$h_{9/2}$	13/2-'→11/2-	13/2-'→ 9/2-	3.8	1.0

should be hindered. If the hindrance factor is assumed to be the same as that of the $h_{11/2}$ bandhead to $h_{9/2}$ bandhead transition, i.e., 10^4, the resulting halflife for an E2 gamma-ray transition is 8 min. Analysis of the multiscaled conversion electron data, however, shows that the 101.2 keV transition decays with a halflife of 2.2 min, i.e., that of the ^{187}Hg parent, and the decay curve is smooth so that any delay in this transition is probably less than 15 sec, which is the duration of the multiscaled plane. Bourgeois et al.[30] suggest a 20 ns halflife based on a Weisskopf estimate. Also, atomic beam experiments indicate the presence of only the 1/2 ground state in ^{187}Au, although an earlier in-beam reaction spectroscopy measurement by Heiser et al.[29] indicated a level with a halflife of 142 ms in ^{187}Au. The energy of this transition, however, was reported as 162 keV.

In addition to the ground band in ^{186}Pt, there is a second band whose 0^+ bandhead is 472 keV above the ground state. The odd proton in ^{187}Au should also be coupled to this band. Only particle states in ^{187}Au can couple to ^{186}Pt, so the $h_{9/2}$ and $s_{1/2}$ are the only states which can couple to this excited band. Six members of a second $h_{9/2}$ band in ^{187}Au have been identified in the present work: the 9/2- bandhead, the 13/2- member, and, tentatively, the 11/2-, $13/2_2$-, 15/2- and 17/2- members.

The spins and parities of the 9/2- and 11/2- levels in this second $h_{9/2}$ band have been determined from the conversion coefficients of the transitions connecting these levels to the analogous levels in the first $h_{9/2}$ band. The 9/2- → 9/2- transition energy is 322.8 keV,

and its internal conversion coefficient is $\alpha_K = 0.439 \pm 0.079$, corresponding to an M1 + E2 + E0 multipolarity assignment (see Table 4-3). The 13/2- → 13/2- transition energy is 387.9 keV, and its conversion coefficient is $\alpha_K = 0.436 \pm 0.141$, again corresponding to a multipolarity assignment of M1 + E2 + E0. The conversion coefficient of the 322.8 keV transition deduced in earlier and independent UNISOR studies[105] is $\alpha_K = 0.373 \pm 0.030$. This anomalous conversion coefficient was interpreted in ref. 105 as arising from M2 + E3 multipolarity, with the assignment solely based on conversion electron and gamma-ray singles measurements. However, when coincidence information is taken into account, this multipolarity is ruled out, since an M2 + E3 transition would be too slow to be seen in coincidence, whereas the 322.8 keV transition shows strong prompt coincidence relationships (see Table 4-3). The same argument holds for the 387.9 keV transition. Thus both the 322.8 and 387.9 keV transitions have been assigned an E0 component in the present work. The spin and parity of the 11/2- member of this second $h_{9/2}$ band were assigned on the basis of coincidences with gamma-rays depopulating levels of known spin and parity. A conversion coefficient could not be deduced for this line from the present data.

Previous studies of ^{187}Hg decay[30] report both the 323 and 388 keV transitions but do not report conversion coefficients for either and do not place the 323 keV transition in the energy level scheme. It does, however, report the same strong coincidences for both the 388 and 323 keV transitions as seen in the present work and places the 388 keV transitions as in the present work, but fails to recognize the significance of the level.

Three other members of this second $h_{9/2}$ band have been tentatively identified. These levels were placed with systematics and coincidence relationships. The 13/2- → 9/2- and 11/2- → 9/2- gamma-ray energies in the second $h_{9/2}$ band are found to fit the odd-A gold systematics diagram at a fictitious mass location just below ^{189}Au (Fig. 5-3) The other members of this band were thus assumed to be near the energies predicted at this point on the systematics diagram, e.g., systematics predict the 17/2- member to lie ~400 keV above the 13/2- member and a 425 keV transition is found in the coincidence data that feeds the 13/2- level. Similarly, the second 13/2- member and the 15/2- member of the second $h_{9/2}$ band were tentatively identified by looking for coincidences near the energies predicted for them by systematics. These two levels, however, are not as firmly established as the 17/2- member.

An estimate of the E0 strength parameter ρ can be made from the present data for the 388 keV transition by making a few additional assumptions. Since the 298 keV transition is assumed to be the 13/2- → 9/2- transition, its lifetime can be approximated by the lifetime of a similar E2 transition of ^{189}Au, known from ref. 106. The total halflife of the 13/2- level is then computed using the measured gamma-ray and conversion electron intensities of the transitions depopulating this level. The partial halflife of the level due to E0 conversion electrons is then computed and thus the E0 transition probability obtained. The strength function is computed from[107]

$$\rho^2 (E0) = \frac{W_e(E0)}{\Omega(Z,k)} \qquad (5\text{-}1)$$

where $W_e(E0)$ is the transition probability of E0 conversion electrons and $'Z,k)$ is tabulated in ref. 108. The strength function thus deduced is $\rho \approx 0.6$. A similar strength function is obtained for ^{100}Zr where $\rho = 0.5$ for the $0_2^+ \rightarrow 0_1^+$ transition. This large value of $\rho(E0)$ for ^{100}Zr is attributed to a slight mixing of the two 0^+ states. However, ref. 109 also points out that these 0^+ states have a very different nature since they do not mix enough to repel each other as strongly as states of like nature are commonly belived to do.

For the second $h_{9/2}$ band to occur where it does on the $h_{9/2}$ systematics diagram, two minima in the potential energy surface would be required in close proximity with respect to the deformation parameters β, γ, i.e., there would have to be a large potential barrier between these two minima. A simple interpolation of the $h_{9/2}$ systematics yields $\beta \approx 0.18$, $\gamma \approx 20^0$ for the second ^{187}Au $h_{9/2}$ band, compared to $\beta \approx 0.20$, $\gamma \approx 20^0$ for the first ^{187}Au $h_{9/2}$ band. Potential energy surface calculations[66,67], however, predict that the platinum nuclei are very γ-soft. This would prevent the existence of such a large barrier between two points so closely spaced in the β - γ plane.

This second $h_{9/2}$ band may thus require an additional nuclear degree of freedom. Two possible candidates for such a degree of freedom are inertia parameter isomerism and pairing isomerism, both mentioned in Chapter II. These degrees of freedom enter through the moment of inertia $\mathcal{I}$ = f (inertial parameters, pairing). If fluctuations in the inertial parameters[69] are responsible for the second $h_{9/2}$ band, it is only fortuitous that the band fits the systematics where it does.

It could turn out that β and γ are not the values given by systematic predictions and the band spacing still fit the systematics diagram. Regardless of whether it is the inertial parameters or two minima in the β - γ potential energy surface, the E0 transitions imply yet a third shape in ^{187}Au.

Positive Parity Bands

The first attempt to describe the positive parity states of the odd-mass gold isotopes was made by Hecht and Satchler[58] as described in Chapter II. This model has been extended by Larsson et al.[110] and applied to $^{193-199}$Au by Vieu et al.[59,60]. This extended model correctly predicts the three major positive parity bands which are systematically seen throughout the odd-mass gold isotopes (see Figs. 5-5). It is also successful in predicting electromagnetic properties of the transitions between these levels.

In the positive parity bands of $^{193-199}$Au, both the experimental and theoretical spectra of the extended model display interband transitions which are nearly as strong as intraband transitions[59]. These interband transitions are due to mixing of the (rotational) K quantum number of the levels. Such transitions cannot be taken into account in the Meyer ter Vehn calculations since each band is characterized by a well-defined value of the quantum number j and the calculations do not include j-mixing. In ^{187}Au, however, the experimental spectrum (Fig. 5-5) shows few interband transitions with intensities comparable to those of intraband transitions. This suggests that the positive parity bands might also be approximated by pure-j levels and the Meyer ter Vehn prescription applied to them. Calculations were performed for

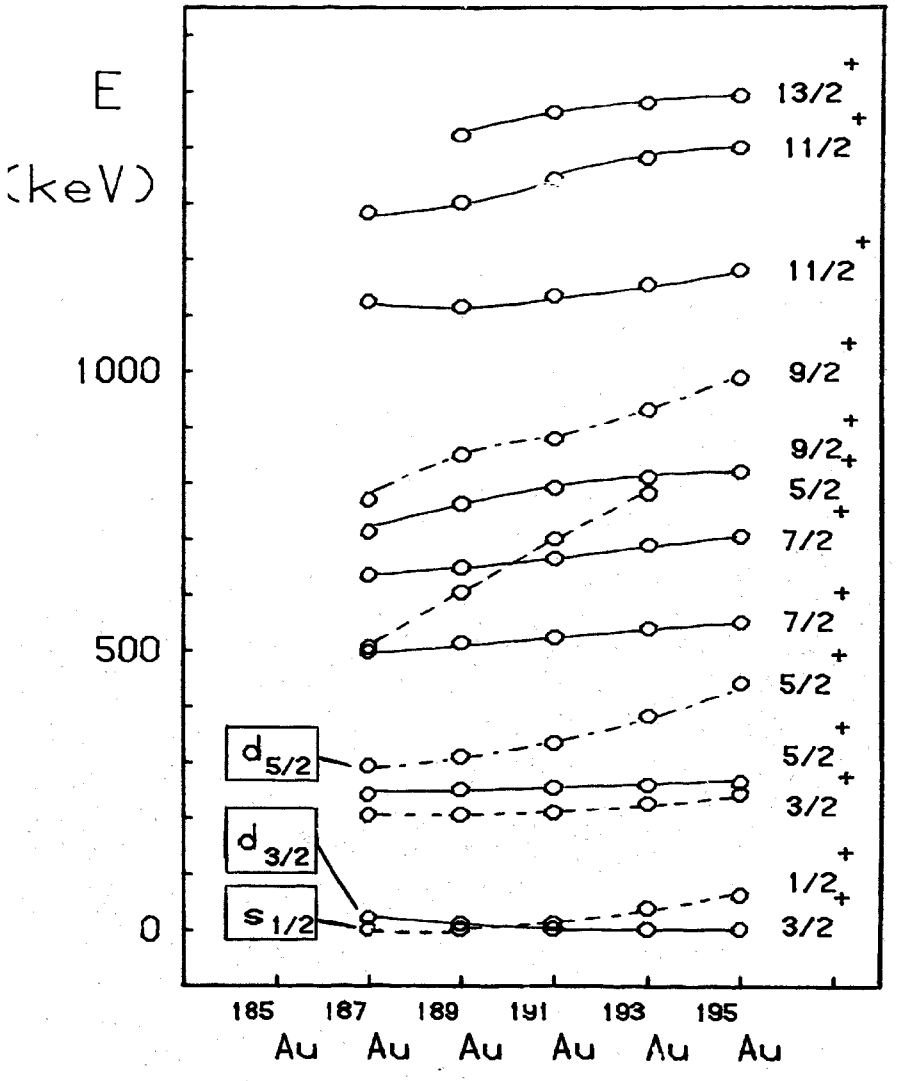

Figure 5-5. Systematics of Members of the $s_{1/2}$, $d_{3/2}$ and $d_{5/2}$ Bands in $^{187-195}Au$.

these bands, again using standard parameters, and are shown in Fig. 5-6 compared with the experimental results. The $d_{3/2}$ and $d_{5/2}$ bands are interpreted as holes coupled to the ^{188}Hg core and the $s_{1/2}$ band interpreted as a particle coupled to the ^{186}Pt core.

It should be pointed out that the single-particle labels "$d_{3/2}$," "$d_{5/2}$," or "$s_{1/2}$" are only names for the bands and do not imply that ℓ or j are good quantum numbers. In fact, recent (^{3}He,d) studies[111] have shown that the single-particle strength is not contained in any one level in ^{195}Au. For example, there is a 1/2+ state at 841 keV in ^{195}Au which contains more of the $s_{1/2}$ strength than the 1/2+ state at 61.3 keV. These labels, however, are retained for convenience.

Although the $d_{5/2}$ and $s_{1/2}$ bands are not well developed in the experimental level scheme, several features of these bands should be noted in comparison with predictions of Meyer ter Vehn calculations. First, the theoretical $d_{5/2}$ band is decoupled with the 9/2+ energy level below the 7/2+ energy level. This could be a clue to finding the 7/2+ member of this band, although there are no candidates for it in the present work. Secondly, the theoretical $s_{1/2}$ band displays the weak coupling limit. If this coupling scheme is correct, there should be a 5/2+ level nearly degenerate with the 3/2+ level at 203 keV. In Table 4-2(a), it can be seen that there is an unassigned component of the 205 keV line which may de-excite the 5/2+ member of this band. Finally, in the $d_{3/2}$ band, the Meyer ter Vehn recipe successfully reproduces the level order but fails in the usual manner in describing the high-spin members. The theoretical transition probabilities are

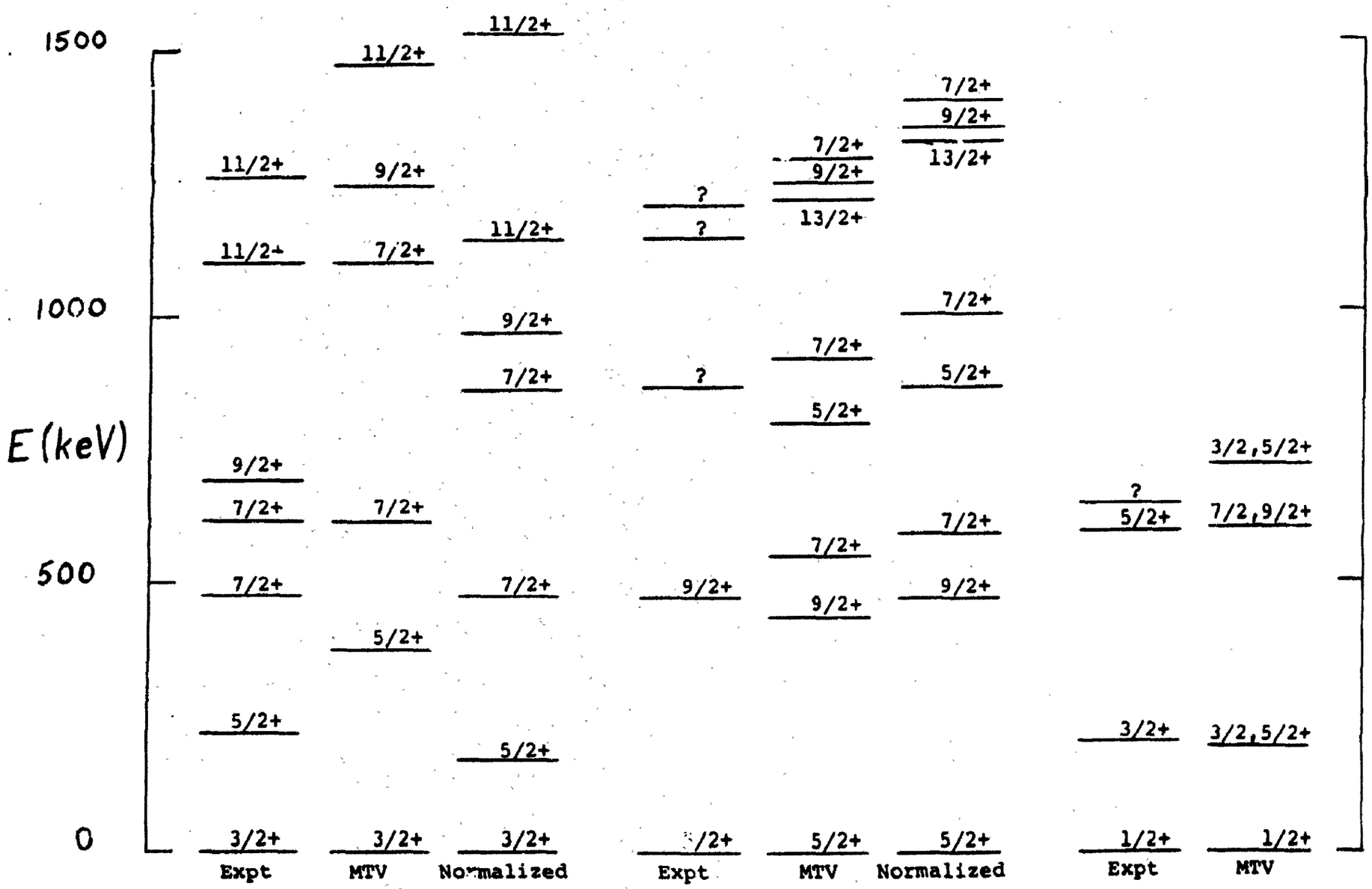

Figure 5-6. Comparison of Experimental and Theoretical (Meyer ter Vehn) $s_{1/2}$, $d_{3/2}$, and $d_{5/2}$ Bands in ^{187}Au. Also shown are the $d_{3/2}$ and $d_{5/2}$ bands normalized to the j + 2 level.

not compared with experiment for these bands since there is some mixing evident between the bands.

"Extra" States

In this section we discuss those levels which cannot be identified as members of any of the bands discussed above. A few of these states belong to the $i_{13/2}$ band which should also be adequately described by a Meyer ter Vehn calculation. The $i_{13/2}$ state is another intruder state which crosses the Z = 82 closed proton shell and decreases in energy with respect to the ground state as the nuclei become more neutron deficient (see Fig. 5-7). In ^{187}Au the $i_{13/2}$ bandhead is 1122 keV above the ground state. The Meyer ter Vehn version of the asymmetric rotor model pictures this band as a proton particle coupled to ^{186}Pt, so transitions from its bandhead to $h_{9/2}$ band members proceed unhindered and are observed in the present work. In coincidence with these transitions are four other transitions defining levels which could be members of the $i_{13/2}$ band. The 0_2^+ state in ^{186}Pt might also be coupled to the $i_{13/2}$ proton, but there are no states which are candidates at present for this structure.

In addition to the transitions between the $i_{13/2}$ bandlead and $h_{9/2}$ states, there is a 501 keV transition from the $i_{13/2}$ bandhead to a level at 620 keV. This level then decays via a 499 keV M1 transition to the $h_{9/2}$ bandhead. Since the 501 keV transition is assigned an E1 multipolarity, the level at 620 keV is established as an 11/2- level. This level has no analog in the systematics and is interpreted in the present work as the strongly coupled odd proton 11/2- [505] Nilsson state due to a hole coupled to the 0_2^+ state of ^{188}Hg. This 0_2^+ state

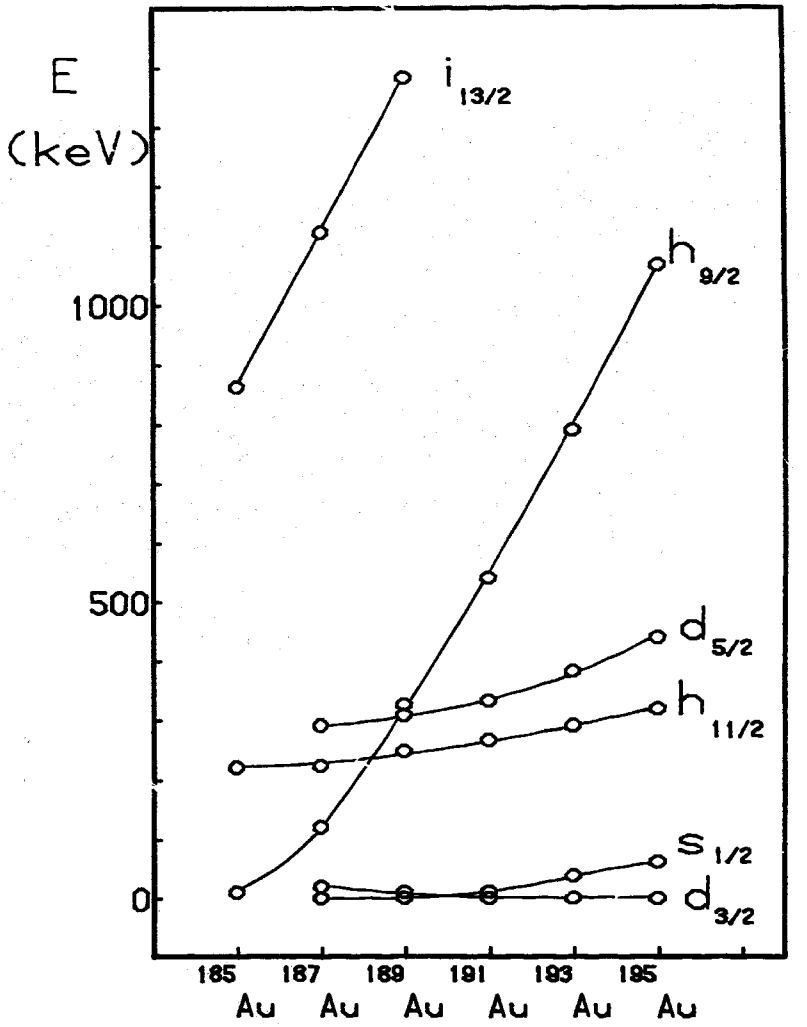

Figure 5-7. Systematics of the $s_{1/2}$, $d_{3/2}$, $d_{5/2}$, $h_{9/2}$, $h_{11/2}$ and $i_{13/2}$ Proton Bandheads for $^{187-195}$Au.

has been studied in previous UNISOR work[70] and interpreted as a well-deformed prolate shape with $\varepsilon = 0.27$ and $\gamma = 0^{o}$. The 499 keV transition depopulating this level is in coincidence with several other gamma rays besides the 501 keV transition. These other levels thus defined may be members of a deformed rotational band built on the 11/2- [505] state. A time-to-amplitude-converter (TAC) spectrum of the 499 keV transition in the present work does not display any delayed character which would be expected for a hole-to-particle transition and a shape change. The Weisskopf estimate of the lifetime of a 499 keV M1 transition with a hindrance factor of 10^4 is $T_{1/2} \sim 1$ ns. Thus better time resolution than that achieved in the present work is needed to establish or refute the identification of this level as a Nilsson state.

Besides this 11/2- level and its associated levels, there are several "extra" levels in the positive parity bands which may also result from coupling Nilsson states to the 0_2^+ in ^{188}Hg. The other proton Nilsson states available for strong coupling as a hole are the 1/2+ [400], 3/2+ [402], and 7/2+ [404] states (see Fig. 2-3). The 1/2- [541] and 1/2+ [660] Nilsson states appear only as particle states in this region, and are thus not available for coupling to the ^{188}Hg core as holes. The spins and parities of these extra states are not known at present, but they are tentatively identified as Nilsson states. Again, the transitions defining these levels may exhibit a delayed character due to the shape change, if they are Nilsson states, but the TAC resolution of the present work does not exhibit delayed character.

Also, if these extra levels are Nilsson states, they should form rotational bands as noted below. There are also extra states observed in the $h_{11/2}$ band at 881 keV and 924 keV.

Conclusion and Future Work

The results of the present work indicate that four shapes can be associated with ^{187}Au. The two previously known shapes[26,72] are the weakly deformed prolate shape associated with the ground band of ^{186}Pt and the weakly deformed oblate shape associated with the ground band of ^{188}Hg. The present work indicates the existence of a third shape, possibly due to a new degree of freedom, which is associated with the excited 0^+ state in ^{186}Pt. If no new degree of freedom is considered, this shape seems to be another weakly deformed prolate shape with deformation parameters β and γ very similar to those of the ground state in ^{186}Pt. If an additional degree of freedom is assumed, the deformation parameters may be different from those predicted by systematics, but would still imply a third shape in ^{187}Au. The Nilsson states coupled to the excited 0^+ state in ^{188}Hg would then account for a fourth shape, a deformed prolate shape.

In order to establish the two additional shapes more firmly, additional measurements are needed: In particular, better internal conversion electron data are needed, in order to assist in the assignment of spins and parities of the extra states. The transitions depopulating these levels are relatively weak, so any transition feeding them would be even weaker. If there are rotational bands built on these states, and the states are deformed, there would be many

M1 + E2 transitions between band members. Since low-energy M1 transitions are strongly internally converted, and since the intensities of the transitions to be searched for are weak, the conversion electron data might be the best way to identify rotational bands built on the deformed Nilsson states. Further conversion electron measurements could also establish spins of the states tentatively identified as members of the second $h_{9/2}$ band. In particular, the 11/2-, second 13/2-, 15/2-, and 17/2- members of the second $h_{9/2}$ band should decay via E0 transitions to their analog states in the first $h_{9/2}$ band. Better time resolution could establish the isomeric nature of the extra states identified as Nilsson states. A delay in the transitions from these states is expected, since there is a shape transition involved. Finally, a measurement of the lifetime of the 101 keV E3 transition depopulating the $h_{9/2}$ bandhead is needed. If its lifetime is a few seconds, it can be measured by directly producing ^{187}Au and multiscaling the sources collected. If the lifetime is in the millisecond range, the multiple time analysis system[77] can be used. Some of these suggested experiments have already been started at UNISOR.

BIBLIOGRAPHY

1. M. G. Mayer and J. H. D. Jensen, Elementary Theory of Nuclear Shell Structure, John Wiley and Sons, Inc., New York (1957).

2. A. Bohr, Mat. Fys. Medd. Dan. Vid. Selsk. 27, No. 14 (1952).

3. A. Bohr and B. R. Mottelson, Mat. Fys. Medd. Dan. Vid. Selsk. 27, No. 16 (1953).

4. F. S. Stephens, Revs. Mod. Phys. 47, 43 (1975).

5. J. Meyer ter Vehn, Nucl. Phys. A249, 111 (1975).

6. J. Meyer ter Vehn, Nucl. Phys. A249, 141 (1975).

7. G. Alaga, Nucl. Instr. and Meth. 146, 171 (1977).

8. Y. Tanaka and R. K. Sheline, Nucl. Phys. A276, 101 (1977).

9. T. Fényes, I. Mahunka, Z. Maté, R. V. Jolos and V. Paar, Nucl. Phys. A247, 103 (1975).

10. G. Leander, Nucl. Phys. A273, 286 (1976).

11. E. F. Zganjar, J. L. Wood, R. W. Fink, L. L. Riedinger, C. R. Bingham, B. D. Kern, J. L. Weil, J. H. Hamilton, A. V. Ramayya, E. H. Spejewski, R. L. Mlekodaj, H. K. Carter and W. A. Schmidt-Ott, Phys. Lett. 58B, 159 (1975).

12. H. Rubinsztein and M. Gustafsson, Phys. Lett. 58B, 283 (1975).

13. C. Ekström, S. Ingleman, G. Wannberg, and M. Skarestad, CERN 76-13, 193 (1976).

14. J. Berkes, R. Haroutunian and G. Marest, CERN 76-13, 209 (1976).

15. M. Finger, R. Foucher, J. P. Husson, J. Jastrzebski, A Johnson, C. Sébille, R. Henck, J. M. Kuchly, R. Regal, P. Siffert, G. Astner, B. R. Erdal, E. Hagebo, A. Kjelberg, F. Münnich, P. Patzelt, E. Beck and H. Kugler, CERN 70-29 (1970).

16. M. A. Deleplanque, C. Gerschel, M. Ishihara, N. Perrin and B. Ader, Compt. Rend. 280B, 515 (1975).

17. M. A. Deleplanque, C. Gershel, M. Ishihara, N. Perrin, B. Adler, C. Bourgeois, J. P. Husson, P. Kilcher and J. Letessier, J. Physique 36, C5-97 (1975).

18. C. Bourgeois, M. G. Desthuillers, P. Kilcher, J. Letessier, J. R. Husson, V. Berg, A. Hoglund, A. Huck, A. Knipper, C. Richard-Serre, C. Sebille-Schuck, M. A. Deleplanque, C. Gerschel, M. Ishihara, N. Perrin and B. Adler, CERN 76-13, (456 (1976).

19. C. Bourgeois, P. Kilcher, J. Letessier, M. G. Desthuillers, F. Beck, T. Birsky and A. Knipper, ORSAY Annual Report, N.21 (1978).

20. P. Hornshoj, B. R. Erdal, P. G. Hansen, B. Johnson, K. Aleklett and G. Nyman, Nucl. Phys. A239, 15 (1975).

21. C. L. Duke, P. G. Hansen, O. B. Nielsen and G. Rudstam, Nucl. Phys. A151, 609 (1970).

22. S. K. Saha, C. L. Dors, M. Piiparinen, H. Helppi, P. J. Daley, T. L. Khoo, and F. M. Bernthal, Bull. Am. Phys. Soc. 23, 628 (1978).

23. M. Piiparinen, J. C. Cunnane, S. K. Saha, P. J. Daly, C. L. Dors, F. M. Bernthal and T. L. Khoo, Bull. Am. Phys. Soc. 20, 670 (1975).

24. M. Piiparinen, J. C. Cunnane, P. J. Kaley, C. L. Dors, F. M. Bernthal, and T. L. Khoo, Phys. Rev. Lett. 34, 1110 (1975).

25. M. Piiparinen, S. K. Saha, P. J. Daley, C. L. Kors, F. M. Barnthal and T. L. Khoo, Phys. Rev. C13, 2208 (1976).

26. V. Berg, C. Bourgeois and R. Foucher, J. Physique 36, 613 (1975).

27. M. A. Deleplanque, C. Gerschel, M. Ishihara, N. Perrin, V. Berg, C. Bourgeois, M. G. Gesthuiller, J. P. Husson, P. Kilcher and J. Letessier, J. Physique Lett. 36, L-205 (1975).

28. C. Ekstrom, I. Lindgren, S. Ingelman, M. Olsmats and G. Wannberg, Phys. Lett. 60B, 146 (1976).

29. C. Heiser, K. F. Alexander, N. F. Brinckmann, N. Nenov, W. Neubert and H. Rotter, Nucl. Phys. A96, 327 (1967).

30. C. Bourgeois, P. Kilcher, J. Letessier and M. G. Desthuillers, Nucl. Phys. A295, 424 (1978).

31. P. G. Hansen, H. C. Nielsen, K. Wilsky, M. Alpsten, M. Finger, A. Lindahl, R. A. Waumann and O. B. Nielsen, Nucl. Phys. A148, 249 (1970).

32. G. Albouy, M. Gusakov, N. Poffé, J. Physique Rad. 21, 751 (1960).

33. P. G. Hansen, P. Hornshoj, H. L. Nielsen, K. Wilsky, H. Kugler, G. Astner, E. Hagebo, J. Hudis, A. Kjelberg, F. Münnich, P. Patzelt, M. Alpsten, G. Andersson, Aa. Appelqvist, B. Bengtsson, R. A. Naumann, O. B. Nielsen, E. Beck, R. Foucher, J. P. Husson, J. Jastrzehski, A. Johnson, J. Alstad, T. Jahnsen, A. C. Pappas, T. Tuuaal, R. Heuck, P. Siffert and G. Rudstam, Phys. Lett. 28B, 415 (1969).

34. S. G. Nilsson, Mat. Fys. Medd. Dan. Vid. Selsk. 29, No. 16 (1955).

35. M. G. Bunker and C. W. Reich, Revs. Mod. Phys. 43, 348 (1971).

36. W. Ogle, S. Wahlborn, R. Piepenbring and S. Fredriksson, Revs. Mod. Phys. 43, 424 (1971).

37. R. R. Chasman, I. Ahmad, A. M. Friedman and J. R. Erskine, Revs. Mod. Phys. 49, 833 (1977).

38. P. Kleinheinz, R. F. Casten and B. Nilsson, Nucl. Phys. A203, 539 (1973).

39. F. T. Baker and D. Goss, Phys. Rev. Lett 36, 852 (1976).

40. S. G. Nilsson, C. F. Tsang, A. Sobiczewski, Z. Szymanski, S. Wyech, C. Gustafsson, I.-L Lamm, P. Möller and B. Nilsson, Nucl. Phys. A131, 1 (1969).

41. T. Kühl, P. Dabkiewicz, C. Duke, H. Fischer, H.-J. Kluge, H. Kremmling and E.-W. Otten, Phys. Rev. Lett. 39, 180 (1977).

42. J. Bonn, C. Huber, H.-J Kluge and E.-W. Otten, Z. Phys A276, 203 (1976).

43. M. A. Preston and R. K. Bhaduri, Structure of the Nucleus, Addison-Wesley, Reading, Mass. (1975), pp. 349-350.

44. A. S. Davydov and A. A. Chaban, Nucl. Phys. 20, 499 (1960).

45. J. M. Eisenberg and W. Greiner, Nuclear Models, North Holland Amsterdam (1970), p. 36.

46. E. Merzbacher, Quantum Mechanics, John Wiley and Sons, Inc., New York (1970), p. 540.

47. A. Bohr and B. R. Mottelson, Nuclear Structure, Benjamin, Reading, Mass (1969), Vol. I, p. 272.

48. J. Bardeen, L. N. Cooper and J. R. Schriffer, Phys. Rev. 108, 1175 (1957).

49. A. Bohr, B. Mottelson and D. Pines, Phys. Rev. 110, 936 (1958).

50. I. Ragnarsson and R. A. Broglia, Nucl. Phys. A263, 315 (1976).

51. S. G. Nilsson, J. R. Nix, P. Möller and I. Ragnarsson, Nucl. Phys. A222, 221 (1974).

52. R. E. Griffin, E. Jackson and E. Volkov, Phys. Lett. 36B, 281 (1971).

53. W. I. van Rij and S. H. Kahana, Phys. Rev. Lett. 28, 50 (1972).

54. R. R. Chasman, Phys. Rev. Lett. 28, 1275 (1972).

55. A. M. Friedman, K. Katori, D. Albright and J. P. Schiffer, Phys. Rev. C9, 760 (1974).

56. V. Paar, Ch. Vieu and J. S. Dionisio, Nucl. Phys. A284, 199 (1977).

57. F. Dönau and S. Frauendorf, Phys. Lett. 71B, 263 (1977).

58. K. T. Hecht and G. R. Satchler, Nucl. Phys. 32, 286 (1962).

59. Ch. Vieu, S. E. Larsson, G. Leander, I. Ragnarsson, W. DeWieclawik and J. S. Dionisio, J. Phys. G4, 531 (1978).

60. Ch. Vieu, S. E. Larson, G. Leander, I. Ragnarsson, W. DeWiechlawik and J. S. Dionisio, J. Phys. G4, 1159 (1978).

61. V. V. Pashkevich and R. A. Sardaryan, Nucl. Phys. 65, 401 (1965).

62. H. Toki and A. Faessler, Nucl. Phys. A253, 231 (1975).

63. H. Toki and A. Faessler, Z. Phys. A276, 35 (1976).

64. A. Faessler and H. Toki, Phys. Lett. 59B, 211 (1975).

65. K. T. Hecht, Phys. Lett. 58B, 253 (1975).

66. M. Baranger and K. Kumar, Nucl. Phys. A110, 490 (1968).

67. K. Kumar and M. Baranger, Nucl. Phys. A110, 529 (196B).

68. G. Gneuss and W. Greiner, Nucl. Phys. A171, 449 (1971).

69. K. Pomorski, T. Kaniowska, A. Sobiczewski and S. G. Rohozinski, Nucl. Phys. A283, 394 (1977).

70. J. H. Hamilton, A. V. Ramayya, E. L. Bosworth, W. Lourens, J. D. Cole, B. Van Nooijen, G. Garcia-Bermudez, B. Martin, B. N. Subba Rao, H. Kawakami, L. L. Riedinger, C. R. Bingham, F. Turner, E. F. Zganjar, E. H. Spejewski, H. K. Carter, R. L. Mlekodaj, W. D.Schmidt-Ott, K. R. Baker, R. W. Fink, G. M. Gowdy, J. L. Wood, A. Zenuolis, B. D. Kern, K. J. Hofstetter, J. L. Weil, K. S. Tooth, M. A. Ijaz, K. F. R. Faftry, Phys. Rev. Lett 35, 562 (1975).

71. M. Finger, R. Foucher, J. P. Husson, J. Jastrzebski, A. Johnson, G. Astner, B. R. Erdal, A. Kjelberg, P. Patzelt, A. Hoglund, S. G. Malmskog, and R. Henck, Nucl. Phys. A188, 369 (1972).

72. M. A. Deleplanque, C. Gerschel, N. Perrin, and V. Berg, Nucl. Phys. A249, 366 (1975).

73. E. H. Spejewski, R. L. Mlekodaj, H. K. Carter, W. D. Schmidt-Ott, E. L. Robinson, R. W. Fink, J. M. Palms, W. H. Brantley, B. D. Kern, K. J. Hofstetter, E. F. Zganjar, A. R. Quinton, F. T. Avignone, W. M. Bugg, C. R. Bingham, F. Culp, J. Lin, J. H. Hamilton, A. V. Ramayya, M. A. Ijaz, J. A. Jacobs, J. L. Duggan, W. G. Pollard, R. L. Robinson, R. S. Livingston, C. E. Bemis, E. Eichler, N. R. Johnson, and K. S. Toth, Proceedings Eighth International Electromagnetic Isotope Separator Conference, eds. G. Andersson and G. Holmen, Chalmers University, Gothenberg, Sweden (1973), p. 318.

74. G. M. Gowdy, Ph.D. Thesis, Georgia Institute of Technology, 1976.

75. M. L. Mallory, E. D. Hudson and G. Fuchs, IEEE Transactions on Nucl. Sci. NS-19, 2, 118 (1971).

76. R. L. Mlekodaj, E. H. Spejewski, H. K. Carter and A. G. Schmidt, Nucl. Instr. and Meth. 139, 299 (1976).

77. H. K. Carter, E. H. Spejewski, R. L. Mlekodaj, A. G. Schmidt, F. T. Avignone, C. P. Bingham, R. A. Braga, J. D. Cole, A. V. Ramayya, J. Hamilton, E. L. Robinson, K. S. R. Sastry, and E. F. Zganjar, Nucl. Instr. and Meth. 139, 349 (1976).

78. H. K. Carter and R. L. Mlekodaj, Nucl. Instr. and Meth. 128, 611 (1975).

79. E. H. Spejewski, R. L. Mlekodaj, H. K. Carter, A. G. Schmidt, and F. T. Avignone, private communication (1978).

80. E. A. Henry, Nucl. Data Sheets 11, 495 (1974).

81. M. R. Schmorak, Nucl. Data Sheets 22, 487 (1977).

82. Program developed by M. L. Halbert, ORNL (1976).

83. Program developed by H. J. Saltmarsh, ORNL (1973).

84. R. J. Gehrke, J. E. Cline and R. L. Heath, Nucl. Instr. and Meth. 91, 349 (1971).

85. R. S. Hager and E. C. Seltzer, Nucl. Data Tables, A4, 1 (1968).

86. M. Girod and B. Grammaticos, Phys. Rev. Lett. 40, 361 (1978).

87. C. Baktash, J. X. Saladin, J. J. O'Brien and J. G. Alessi, Phys. Rev. 18, 131 (1978).

88. J. L. Wood, R. W. Fink, E. F. Zganjar and J. Meyer ter Vehn, Phys. Rev. 14, 682 (1976).

89. J. L. Wood, Private communication (1978).

90. A. Visvananthan, E. F. Zganjar, M. A. Grimm, J. L. Wood, R. W. Fink, A. C. Kahler, L. L. Riedinger, E. L. Robinson and H. K. Carter, Bull. Am. Phys. Soc. 22, 615 (1977).

91. T. L. Khoo, F. M. Bernthal, C. L. Cors, M. Piiparinen, S. Saha, P. J. Daly and J. Meyer ter Vehn, Phys. Lett. 60B, 341 (1976).

92. E. F. Zganjar, Private communication (1978).

93. A. Visvanathan, Private communication (1978).

94. E. Hagberg, P. G. Hansen, P. Hornshoj, B. Jonson, S. Mattsson and P. Tidemand-Petersson, Phys. Lett. 78B, 44 (1978).

95. J. O. Newton, F. S. Stephens and R. M. Diamond, Nucl. Phys. A236, 225 (1974).

96. A. L. Goodman, Nucl. Phys. A287, 1 (1977).

97. A. L. Goodman and J. Borysowicz, Nucl. Phys. A295, 333 (1978).

98. W. DeWieclawik, S. E. Larsson, I. Ragnarsson, Ch. Vieu and J. S. Dionisio, J. Phys. G3, L57 (1977).

99. J. S. Dionisio, Ch. Vieu, W. DeWieclawik, R. Foucher, M. Beiner, S. E. Larsson, G. Leander and I. Ragnarsson, J. Phys. G2, L183 (1976).

100. J. L. Wood and R. W. Rink, Bull. Am. Phys. Soc. 20, 1185 (1975).

101. J. L. Wood and R. W. Fink, Bull. Am. Phys. Soc. 21, 639 (1976).

102. J. L. Wood and R. W. Fink, Bull. Am. Phys. Socl 21, 1001 (1976).

103. J. L. Wood, Bull Am. Phys. Soc. 22, 643 (1977).

104. J. M. Blatt and V. F. Weisskopf, Theoretical Nuclear Physics, John Wiley and Sons, Inc., New York (1952).

105. B. G. Ritchie, Masters Thesis, University of South Carolina, 1977, Unpublished.

106. V. Berg, R. Foucher and A. Höglund, Nucl. Phys. A244, 462 (1975).

107. A. V. Aldushchenkov and N. A. Voinova, Nucl. Data Tables 11, 299 (1972).

108. E. L. Church and J. Weneser, Phys. Rev. 103, 1035 (1956).

109. T. A. Khan, W. D. Lauppe, K. Sistemich, H. Lawin and H. A. Selic, Z. Phys. A284, 313 (1978).

110. S. E. Larsson, G. Leander and I. Ragnarsson, to be published, cited in ref. 59 (1978).

111. M. L. Munger and R. J. Peterson, Nucl. Phys. A303, 199 (1978).

[redacted]

Marvin Anton Grimm, Jr., [redacted] He attended the public school system in Savannah and graduated from Savannah High School in June, 1969. He entered Georgia Institute of Technology in the Fall of 1969 and received the Bachelor of Science Degree in Physics in 1973, with honors, and the Master of Science Degree in Physics in 1974. He is a member of the Physics Honor Society, Sigma Pi Sigma. He married the former Arlene Tankersley of Chatsworth, Georgia, in 1976, and they expect their first child in November, 1978.